

Interactive comment on “Aerosol liquid water content in the moist southern West African monsoon layer and its radiative impact” by Konrad Deetz et al.

Konrad Deetz et al.

konrad.deetz@kit.edu

Received and published: 4 August 2018

Answer to Referee #1 Konrad Deetz 25 July 2018

Dear Referee (Atmospheric Chemistry and Physics),

thank you for your report from 3 July 2018. We have accounted for the comments and suggestions in the revised manuscript version. Please find our replies (marked with #) to the individual comments in the following.

Sincerely, Konrad Deetz on behalf of all coauthors

Referee comments: (0) Hygroscopic growth could alter the optical properties of

aerosol. This manuscript reported the follow up simulation study based on Deetz et al. (2018) setup within the COSMO-ART modeling framework for a summer monsoon event in Southern West Africa and estimated the aerosol liquid water content (ALWC) and its impact on radiative transfer. The process was separated into three characteristic phases during commonly Atlantic Inflow event over this region to detailize the ALWC-radiation interactions. It was shown that the accumulation mode particles are the dominant contributor to aerosol liquid water and aerosol growth led to the increase of aerosol optical depth from 0.2 to 0.7. The increased aerosol optical depth can lead to around 20 W/m² decrease in shortwave radiation. Bootstrapping technique was used to derive the linear relationship between ALWC and radiation and found a stronger correlation for in-cloud conditions. This modeling study highlight the importance of including the relationship of RH dependency of aerosol optical depth in atmospheric model, which can significantly impact the local radiation balance, especially over moist tropical environment. The whole manuscript is well structured and the modeling discussion is adequate. I recommend publishing this work as a valuable component of the DACCWA special issue in ACP after the authors address the following comments.

(1) Page 1, Line 23: ALWC = aerosol liquid water content?

We have changed the manuscript accordingly.

(2) Page 4, Line 26-27: the “coarse modes of marine origin” should be (7-9) and the following “coarse modes of mineral origin” should be (10-12)?

We have changed the manuscript accordingly.

(3) Page 5, Line 5: ISORROPIA II does not include fresh soot for calculation. Did the model assume aged soot is internally mixed with sulfate in the calculation of optical properties and radiative transfer?

Yes, fresh soot is not included in ISORROPIA II. In COSMO-ART it is therefore handled separately (as denoted on p. 4 l. 3). And yes, as soon as the soot is treated as

[Printer-friendly version](#)

[Discussion paper](#)



aged, it is an internal mixture within ISORROPIA II and with respect to the calculation of optical properties and radiative transfer.

(4) Page 5, Line 30-32. It is better to mark down the approximate area of “Ivory Coast” (7.5 W – 3W, 4N-10N, should be a subset of 2.5km modeling domain) in Figure 1(b) since nearly all the Figures follow on (e.g. Figure 2, : : :) are focus on this area.

We agree on that and have changed the manuscript (figure and figure caption) accordingly.

(5) Page 6, Line 21: Where is the geographic location of radiosounding site at “Lamto”, please provide the locations in Figure 1. Also, look at the Figure B1-B3 in the Appendix, why there is no sounding comparison for location at “Lamto” for July 2-3. The radiosounding for RH vertical profiles at the two sites are not synchronized and with different time interval? Also, the Figure B2, may be due to the compress the the aspect ratio, the grey shading regions at certain place are not consistent with the description of uniformly 4% uncertainty assigned for radiosondes.

We added Lamto as a magenta dot in Figure 1b. For Lamto, no sounding data is available for 2-3 July. Indeed, the soundings of Lamto and Abidjan are not launched at the same times and with different time intervals. We double-checked the shaded area enveloping the uncertainty of +4 % relative humidity. This is correct. The shading just appears inhomogeneous when the black line is rather horizontal.

(6) Page 7, line 22-23: ALWC was influenced by aerosol types and RH. Are the aerosol type and RH all the same in North China plain and southern West African, so they are comparable? The authors refer this study with China campaigns (e.g. HaChi, PRIDE-PRD) heavily in the introduction section and the following discussion, maybe in some place in the introduction section, the author need to point out the similarity of this DACCIWA campaign with China campaigns such as aerosol loading, RH conditions, atmospheric oxidation capacity, cloud coverage.

[Printer-friendly version](#)

[Discussion paper](#)



This is an interesting question. We try to elaborate this by relating to the study of Bian et al. (2014) as you have proposed. When focusing on the study of Bian et al. (2014), the observations are related to the time period July-August 2009 and focusing on the chinese provinces Shandong, Hebei, Pekin and Tianjin. The climate in this area is in between humid subtropical and humid continental Summers are hot and rainy with temperatures around 24-28 °C in July with the precipitation maximum in summer via influences from the monsoon. A qualitative analysis of Terra Modis satellite images (of course only one overfly per day) revealed that in the 62 d period of July-August 2009 Shandon was fully covered by clouds on 55 d and partly covered by clouds on 7 days. Therefore the weather conditions during the DACCIWA campaign and HaChi campaign are very similar. Both studies focus on the NH summer. Both areas are located in the NH summer monsoon area with high temperatures and are very frequent covered by clouds. The measurement site for the study of Bian et al. (2014) is Wuqing. For this location, Liu et al. (2011) [Figure 3] shows measurements of temperature and relative humidity for July-August 2009. Temperature variations are between 20 °C and 32 °C. Relative humidity variations are between 40 % (mostly 60%) and 95 %. The latter is similar to what is modeled for southern West Africa (Fig. 3 in our manuscript) and to what was observed in southern West Africa at Save supersite (Kalthoff et al., 2018, Fig. 3).

Wuqing is about 90 km away from the Gulf of Bohai. So also HaChi focuses on the area near the coast. Wuqing is surrounded by large cities (Peking (80 km away, 21.5 million inhabitants, megacity), Langfang (30 km away, 4.4 million inhabitants), Tianjin (40 km away, 15.5 million inhabitants, megacity), Tangshan (100 km away, 7.6 million inhabitants)). Also southern West Africa has several large cities especially near the coast. However, the populations are generally smaller but on the same order of magnitude (Lagos: 13.7 million inhabitants, Abidjan: 5 million inhabitants). Based on MODIS observations, Bian et al. (2014) show that the averaged AOD values are generally above 0.6 in the research area and 0.7 above Wuqing. For the DACCIWA region we found averaged MODIS AOD values of 0.4-0.7, slightly smaller to what was observed



in the HaChi region. However, the validity over land is limited because southern West Africa is virtually always covered by clouds, restricting the observations to a few days.

Based on these findings we came to the conclusion that the general meteorological and aerosol conditions are similar for HaChi and DAccIWA and therefore allow a qualitative comparison e.g. of the ALWC values between both sites.

We added the following passage in the conclusions to account for your remark: "HaChi and DAccIWA both focus on the northern hemispheric monsoon season, capture coastal areas that are frequently covered by clouds, have similar temperature and relative humidity conditions (Liu et al., 2011; Kalthoff et al., 2018) as well as similar aerosol loadings (Bian et al. (2014); Deetz et al. (2018a), allowing for a qualitative comparison of modeled ALWC with measurements during HaChi."

(7) Page 8, first paragraph: any explanation why OC dominate the aerosol mass composition? was it a biomass burning event? Also, for Figure D1, is the July 6-7 aerosol component vertical profiles similar to the July 2-3 shown here?

The aerosol mass composition is subject to current research in the DAccIWA research community. Therefore the main outcomes with respect to this question are not yet available/published. However, also the DAccIWA observations (e.g. aircraft measurements) show this dominance of organic carbon (e.g. Flamant et al., 2018). Biomass burning is an important source of OC and likely is responsible for the dominance of OC over Ivory Coast. Based on the experience we obtained with COSMO-ART during our two month (June-July 2016) of forecasting the atmospheric composition (with coarser grid mesh size), we observed that the biomass burning plumes over the Gulf of Guinea (coming from central Africa) frequently swash into the DAccIWA domain. To account for your remark, we repeated the composition analysis for 6-7 July 2016. The corresponding plot (Review-figure-1) is given as appendix to our review answer. For the non-OA, the situation is comparable with 2-3 July but OA is about twice as high compared to 2-3 July with a more distinct vertical gradient, indicating a stronger

[Printer-friendly version](#)

[Discussion paper](#)



influence of biomass burning.

(8) Page 8, Line 15. In contrast, AIT particles are lacking in size and COARSE particles are lacking in number.

We have changed the manuscript accordingly.

(9) Page 8, Line 30-31. Can you also provide the boxplots for median aerosol number concentrations for Aitken, accumulation and coarse mode in Figure E1?

We have changed Figure E1 and the manuscript accordingly. Now the panels (a) and (c) show the median aerosol number concentrations for Aitken, accumulation and coarse mode in addition to the aerosol diameters (b,d). The revised figure is added as appendix (Review-figure-4).

(10) Page 9, Line 8: the total water column is the full integration of model layer (e.g. 30km in Table S1) or below 1500m AGL that this study focused?

Yes, in this case the full integration of model layer is considered and not just the lowest 1500 m. This is done on purpose because the total cloud water column is a widely used measure for the quantification of clouds and with this figure we want to provide some guide values to allow for comparison between the water contribution from clouds and the water contribution from aerosol. Furthermore, Figure 7 is the basis for Figure 8 and in Figure 8 we also analyze the contribution of the in-cloud AOD to the total AOD. Since the total AOD is related to the total vertical column, it is necessary to focus on the total vertical column in the model to ensure consistency.

(11) Page 9, Line 13-15: where is the location of the model realized NLLS and convective clouds in the fouced Ivory Coast region? In Figure 3 and Figure 4, the authors showed the double peak of ALWC during phase 2 period, one near coast and the another one in hilly terrain to the north. Are the peaks for ALWC at different locations also strictly correlated with the model simulated clouds?

We attached Review-figure-2 to emphasize the location of clouds over Ivory Coast

and the total DACCIA domain in general. The figure shows an overview of the low-level cloud temporal evolution between 2 July 21 UTC and 3 July 10 UTC (a-f). Blue shading denotes low-level clouds via the existence of cloud water in the lowest 1.3 km AGL. Brown shading indicates the topography above 250 m ASL. The arrows show the wind speed (m s⁻¹, scale is given below) and direction at 250 m AGL. For 21 UTC and 23 UTC the Atlantic Inflow front is shown in red. From a-c a clear separation between the cloud band directly behind the Atlantic Inflow front and at the coast is visible. This figure is published in Deetz (2018a). The ALWC is primarily correlated with the relative humidity, therefore cloudy areas (with a presence of sufficient amounts of aerosol, which is fulfilled over the entire DACCIA domain) are areas with the highest amounts of ALWC. Review-figure-3 shows the ALWC at 500 m AGL (where we can find the NLLS) over land (for the entire DACCIA domain) on 3 July 6 UTC. (a) Total ALWC (mg m⁻³, shading) and RH of 95% (black contour) and (b) pie chart of the ALWC contribution from the single aerosol modes (%) to the total ALWC in (a). For the entire DACCIA domain highest ALWC values can be found in areas with highest relative humidities (location of the NLLS). This figure is also published in Deetz (2018a).

(12) Page 10: Line 9-10. "... sharpen condition substantially decrease selected area", can you provide the percentage instead of the subjective description on simulated clouds grids versus non-cloud grids in the Ivory Coast area? From page 9, line 18-19, I may know only 3%-9% of total grids realized the clouds in July 2-3. So between the two sensitivity runs, the "ALWC" and "no-ALWC" case, how many percentage were excluded from further radiation analysis due to the model simulated the displacement of clouds?

We calculated the ratio a/b with (a) the number of gridboxes which are related to clouds in both realizations by restricting to gridboxes with a total cloud water difference below 0.1 g m⁻² (masking cloud displacement) (b) and the number of gridboxes which are related to clouds in both realizations without any restrictions (by ignoring cloud displacement). This ratio is between 0.04 and 0.18 in the 25 hour period with a median

[Printer-friendly version](#)[Discussion paper](#)

of 0.076. So on average only 7.6 % of the cloud grid points (clouds in both realizations) can be used for the radiation analysis. We adapted the corresponding sentence in the manuscript as follows: "Consider that the sharpened condition substantially decreases the selected area (on average only 7.6 % of the cloudy area can be considered) and therefore makes the results less representative for the cloudy area."

(13) Page 10, Line 28-29: where is the fixed SST value from COSMO-ART coming from?

The fixed SST is coming from the driving model ICON. For ICON, the SST fields are derived daily at 0 UTC based on observations. A detailed description of the handling of the SST in COSMO can be found in the "COSMO Documentation Part III - Data assimilation" (<http://www.cosmo-model.org/content/model/documentation/core/cosmoAssim.pdf>) at page 89f.

(14) Page 11, Line 24. The AOD is higher -> the difference of AOD is higher

We have changed the manuscript accordingly.

(15) Page 11, Line 33-34. In what percentage are the outliers for ALWC-radiation linear fitting (e.g. "less data, large spread, extra low ALWC ...")?

The following tables summarize the percentages of ALWC data that are not included in the linear fitting (red curves in Fig. 15 (2-3 July) and Fig. H1 (6-7 July)).

2-3 July 2016 (Fig. 15): see Table presented in Review-figure-5

6-7 July 2016 (Fig. H1): see Table presented in Review-figure-6

This analysis shows very similar results when comparing 2-3 July and 6-7 July underlining some robustness in these characteristics. The upper outliers are generally noncritical and negligible (never greater than 0.5%). Lower outliers are only relevant when focusing on longwave radiation and in-cloud areas because there a nonlinear behavior is obvious for which we have no explanation. In this case about one-fifth of

[Printer-friendly version](#)

[Discussion paper](#)



Interactive
comment

the data is not considered. We added/adapted the following passage in the manuscript to meet your concerns: "The fitting omits bins with large ALWC (less data and large spread). A detailed analysis revealed that not more than 0.5 % of the data are omitted. Figure 15c and Figure 15e show a nonlinear behavior for low ALWC. Therefore also these parts are omitted in the linear fitting. This affects 3.5-23.3 % of the data."

(16) Page 12, Line 3-7. What the total size n for the linear fitting based on the grouping of ALWC versus radiation difference with the increment of 0.01 g m^{-2} . If there existed similar linear relationship either derived from observation or model from other regions, it is worth mentioning here and discussing the possible reason for the difference considering during the DACCIWA campaign the aerosol components are dominated by OC (Figure D1) and the water uptake are most significant for coarse mode (Figure 6).

To the first part of your question: In the style of our tables of remark (15) we show again the two tables that now include the total number n of gridboxes that are used for the linear fitting. n_{max} is the maximum number for day and night spanned by the dimensions lon x lat x hours.

2-3 July 2016 (Fig. 15): see Table presented in Review-figure-7

6-7 July 2016 (Fig. H1): see Table presented in Review-figure-8

To the second part of your question: As far as we know, our study is the first approach assessing the linear relationship between ALWC and the radiation difference. We don't have opportunities for a comparison with observations or model results from other regions. (A prerequisite for a comparison of our results with model results from other regions is the availability of a model run that excludes the ALWC effect in the radiative transfer calculations that can be compared with a reference run. From our knowledge, this is not available from other research groups.) Zieger et al. (2017) made an approach with a global model to underline how the hygroscopicity of sea salt affects the AOD (and with that the radiative transfer which is not shown in that work). However, we

[Printer-friendly version](#)

[Discussion paper](#)



have serious doubts that a global model is able to appropriately consider the aerosol growth due to water uptake and their impacts on radiation. Nevertheless we added a reference of this work in our introductory section as follows: "Ziegler et al. (2017) assess the effect of hygroscopicity of sea salt on AOD with a global model approach. They modeled latitudinal averaged reductions in the AOD of up to 14 % when reducing the hygroscopicity of sea salt from 1.5 to 1.1." It is not unusual that OC is the dominating aerosol component, especially when regions are affected by locally emitted or long-range transported biomass burning plumes. E.g. Brito et al. (2014) characterize the ground-based aerosol during the South American Biomass Burning Analysis (SAMBBA) field experiment and found that OC is the dominating aerosol in the sub-micron size range. With respect to the significant water uptake of the coarse mode it has to be considered that in our radiation analysis the coarse mode only consists of sea salt. Generally, the coarse mode in COSMO-ART consists of sea salt, mineral dust and coarse mode anthropogenic particles. But the latter two are not related to ALWC in COSMO-ART. It is not a new finding that sea salt is extremely hygroscopic. Sea salt aerosol particles take up significant amounts of water at $RH < 75\%$, due to the presence of the highly hygroscopic salts of Ca^{2+} and Mg^{2+} (Ziegler et al., 2017). Therefore we have expected most significant water uptake with respect to the coarse mode.

(17) Page 14. Line 1-5. The authors mentioned before the RH underestimation may suggest the model derived ALWC value from this case study is the lower bound (Page 6, line 28- 29), how it compared with the double counting of aerosol activate in the model, which tends to overestimate the AWLC, and the uncertainty for the corresponding radiation change calculation?

The comparison of the modeled RH with soundings at Abidjan and Lamto (Figure B1-B3) indicate that COSMO-ART tends to underestimate the RH, although there is no systematic bias. This is a source of uncertainty for the calculation of ALWC and the radiative transfer. However, it has to be considered that the increase in water uptake

[Printer-friendly version](#)

[Discussion paper](#)



is most sensitive to RH in the narrow range of RH >95 % and less sensitive for RH below 95 %. Therefore, potential deviations should not be overrated. The conception in COSMO-ART, not to remove the activated aerosol from the aerosol population, is done by reason. Model tests in the past that remove the aerosol after activation leads to a very fast (unrealistic) cleaning of the atmosphere. But conception of not removing the activated aerosol from the aerosol population does not lead to an overestimation of the ALWC. Instead it is the consideration of two different aspects: (a) Aerosol that take up water, (b) A cloud droplet or ice crystal that has an aerosol particle (CCN/IN) inside. The activated aerosol particle is a cloud droplet (or ice crystal) and the radiative interaction is only related to its quality being a cloud droplet (the negligible small aerosol particle and its ALWC is not considered when we talk about the interaction between cloud droplet and radiation). On the other hand we have the aerosol in the aerosol population that can take up water when it is hygroscopic. In this case there is an interaction between the aerosol particle (combination of aerosol and ALWC) and the radiation. Therefore we expect that we do not per se overestimate the ALWC with our model concept. But of course, we see uncertainties in the corresponding radiative transfer calculations. With our existing model system and the model realizations we have conducted for this study it is not possible to quantify these uncertainties or to set them in relation to the uncertainty that comes from deviations in the RH.

(18) Page 18, Figure 4. The caption. “Same ass for Fig. 3”??

We have changed the manuscript accordingly.

(19) Page 34, in the row of “vertical levels”, sometime in the main content the notation is “AGL” but here it is “ASL”. make it consistent.

We have changed the manuscript accordingly.

Additional References: Flamant et al. (2018): THE DYNAMICS–AEROSOL–CHEMISTRY–CLOUD INTERACTIONS IN WEST AFRICA FIELD CAMPAIGN Overview and Research Highlights, BAMS, pp. 83–104,

[Printer-friendly version](#)

[Discussion paper](#)



<https://journals.ametsoc.org/doi/pdf/10.1175/BAMS-D-16-0256.1>

Zieger et al. (2017): Revising the hygroscopicity of inorganic sea salt particles, *Nature communications*, Vol. 8, Article number: 15883, <https://www.nature.com/articles/ncomms15883>

Interactive comment on *Atmos. Chem. Phys. Discuss.*, <https://doi.org/10.5194/acp-2018-420>, 2018.

ACPD

Interactive
comment

[Printer-friendly version](#)

[Discussion paper](#)



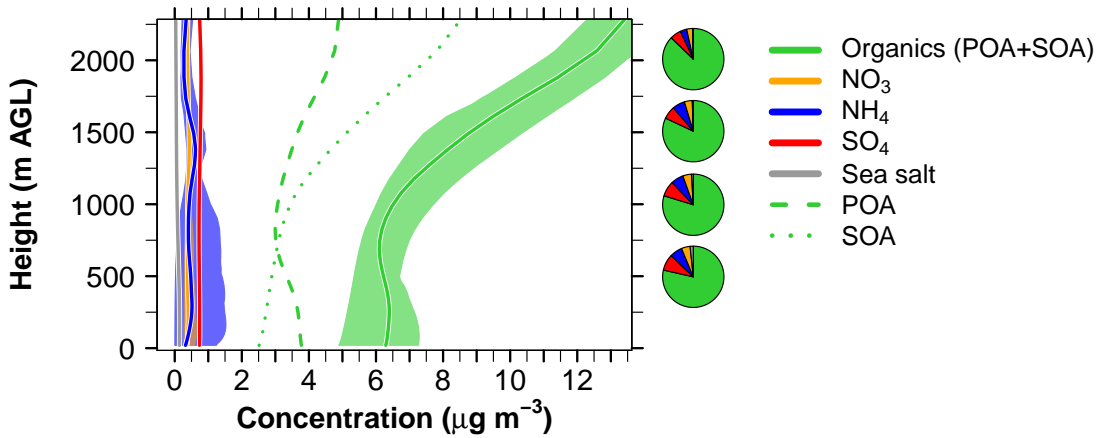


Fig. 1. Vertical profiles (m AGL) of aerosol concentrations ($\mu\text{g m}^{-3}$) for the median over Ivory Coast (7.5° W–3° W, 4–10° N) with respect to the time period 6 July 15 UTC and 7 July 15 UTC.

[Printer-friendly version](#)

[Discussion paper](#)



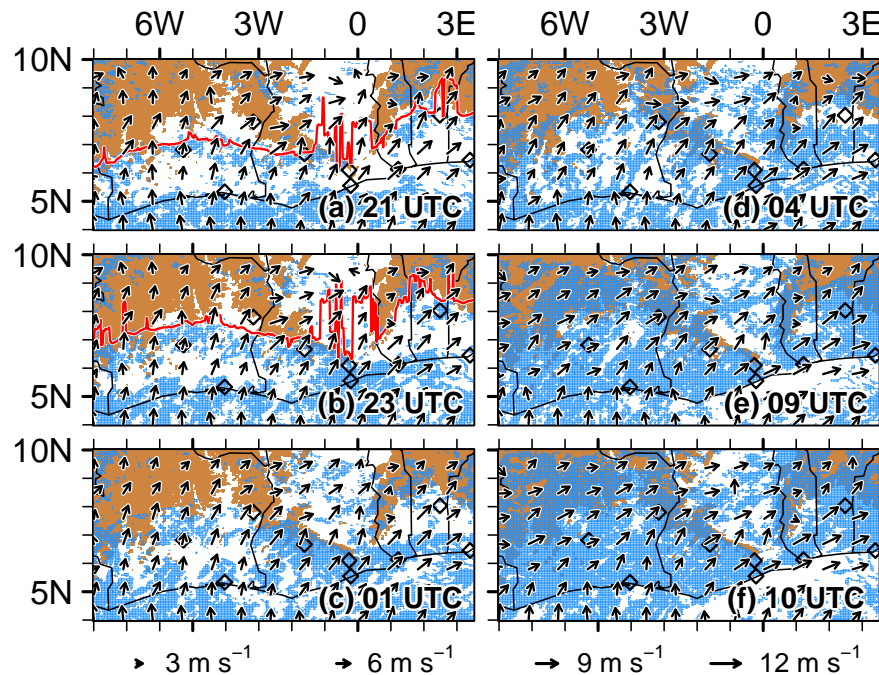


Fig. 2. Overview of the low-level cloud temporal evolution between 2 July 21 UTC and 3 July 10 UTC (a-f). Blue shading denotes low-level clouds via nonzero cloudwater below 1.3 km AGL.

[Printer-friendly version](#)

[Discussion paper](#)



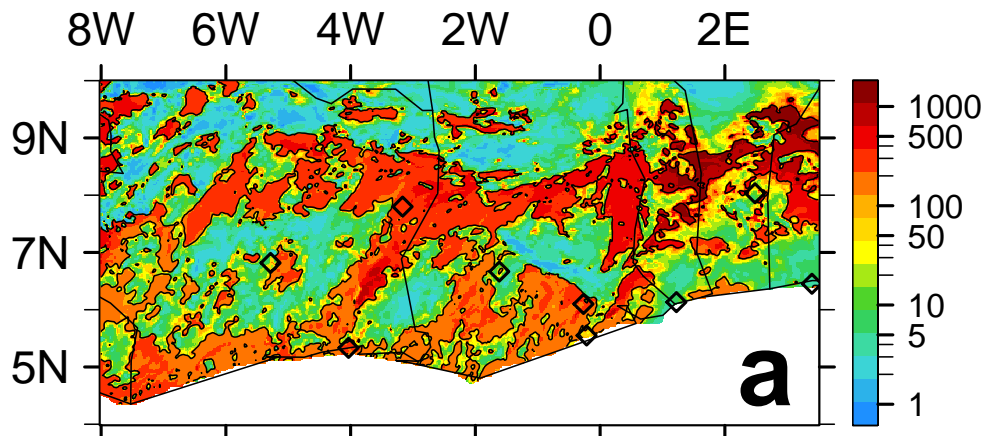
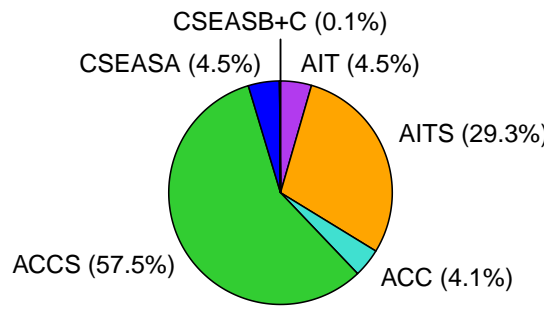
**a****b**

Fig. 3. ALWC at 500 m AGL over land on 3 July 6 UTC. (a) Total ALWC (mg m⁻³, shading) and RH of 95% (black contour) and (b) pie chart of the ALWC.

[Printer-friendly version](#)[Discussion paper](#)

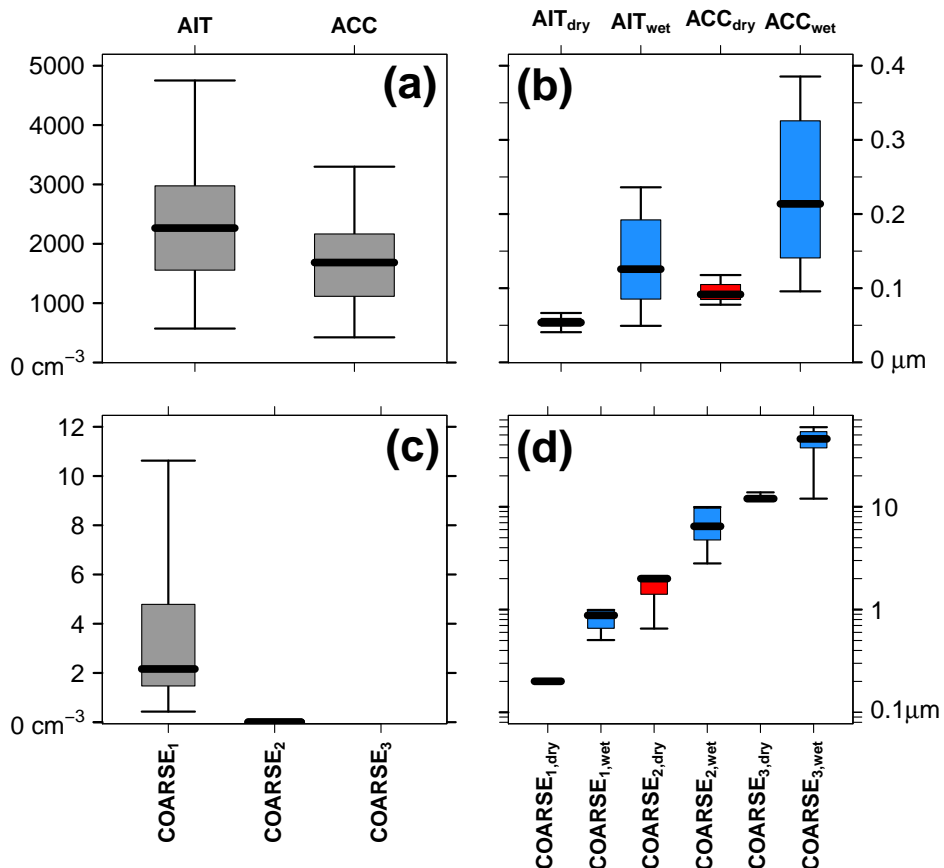


Fig. 4. Boxplots of (a) aerosol number density (cm^{-3}) and (b) dry (red) and wet (blue) aerosol diameters (μm) for AIT and ACC and boxplots of (c) aerosol number density (cm^{-3}) and (d) dry and wet diameter.

2-3 July 2016 (Fig. 15):

	In-cloud ALWC (ICA)		Off-cloud ALWC (OCA)	
	lower outlier	upper outlier	lower outlier	upper outlier
SW day	-	0.4%	-	0.2%
LW day	23.3%	0.4%	-	0.05%
LW night	3.5%	0.5%	-	0.02%

Fig. 5. Table summarizing the percentages of ALWC data that are not included in the linear fitting (red curves in Fig. 15 (2-3 July)).

[Printer-friendly version](#)

[Discussion paper](#)



6-7 July 2016 (Fig. H1):

	In-cloud ALWC (ICA)		Off-cloud ALWC (OCA)	
	lower outlier	upper outlier	lower outlier	upper outlier
SW day	-	0.1%	-	0.2%
LW day	16.7%	0.1%	-	0.05%
LW night	3.5%	0.2%	-	0.06%

Fig. 6. Table summarizing the percentages of ALWC data that are not included in the linear fitting (red curves in Fig. H1 (6-7 July)).

[Printer-friendly version](#)[Discussion paper](#)

2-3 July 2016 (Fig. 15):

`n_max_day = 472680`

`n_max_night= 436320`

	In-cloud ALWC (ICA)		Off-cloud ALWC (OCA)
	<code>n</code>		<code>n</code>
SW day	16560		55120
LW day	12687		55230
LW night	9310		114402

Fig. 7. Table showing the total number n of gridboxes that are used for the linear fitting for 2-3 July 2016 (Fig. 15).

[Printer-friendly version](#)

[Discussion paper](#)



6-7 July 2016 (Fig. H1):

`n_max_day = 472680`

`n_max_night= 436320`

	In-cloud ALWC (ICA)		Off-cloud ALWC (OCA)
	<code>n</code>		<code>n</code>
SW day	17086		48518
LW day	14236		48583
LW night	8903		109723

Fig. 8. Table showing the total number n of gridboxes that are used for the linear fitting for 6-7 July 2016 (Fig. H1).

[Printer-friendly version](#)

[Discussion paper](#)



Interactive comment on “Aerosol liquid water content in the moist southern West African monsoon layer and its radiative impact” by Konrad Deetz et al.

Konrad Deetz et al.

konrad.deetz@kit.edu

Received and published: 4 August 2018

Answer to Referee #2a Konrad Deetz 25 July 2018

Dear Referee (Atmospheric Chemistry and Physics),

thank you for your report from 10 July 2018. We have accounted for the comments and suggestions in the revised manuscript version. Please find our replies (marked with #) to the individual comments in the following.

Sincerely, Konrad Deetz on behalf of all coauthors

Referee comments: (0) Water uptake onto aerosol may increase the size of the aerosol

population as well as their impact on global radiative budget. However, the models used nowadays do not take this effect in account properly. This study is based on simulations results to evaluate the impact of Aerosol Liquid Water Content (ALWC) on shortwave and longwave radiations over Southern West Africa. The authors try to estimate the effect of cloud presence, aerosol size and dynamical processes on ALWC. The manuscript is well written and definitely within the scopus of ACP. Therefore I recommend publishing this work after the authors address the following comments.

(1) There are a lot of figures in this paper and I felt like most of them were not correctly described in the text. Indeed, each line drawn on a plot deserves at least a small explanation otherwise there is no need to plot it.

The figures are necessary to transport our findings to the reader. The number of figures increased because we actively decided to repeat some of the pivotal figures also for the time period 6-7 July 2016 in the appendix (in addition to our main focus 2-3 July 2016). This is done to support our findings, making them more robust within our limited capacity to run further computationally expensive model realizations. We think that all figures are described in detail. If you have the feeling that a figure is not correctly described please indicate which passage has to be revised.

(2) This kind of study is highly dependent on RH fields. In this manuscript, only profiles observed on July 2, 3, 5 and 6 2016 were compared to simulations results at two different locations (Lamto and Abidjan). Could you compare horizontal RH fields over West Africa for both periods?

We agree, RH is the predominant factor for ALWC. We are convinced RH profiles from soundings are appropriate to evaluate the modeled RH. Radiosounding is one of the most accurate measurement techniques for quantifying RH. Horizontal fields of observed RH are not available from DACCIWA observations. Also remote sensing does not provide horizontal RH fields but statements about the total column water. However, remote sensing is extremely limited over SWA due to the frequent cloud cover.

[Printer-friendly version](#)[Discussion paper](#)

(3) Could you add more explanation about the dynamics of the Atlantic inflow? Indeed, sea breeze could be comparable to the Atlantic inflow but the occurrence time is not exactly the same. The AI front is moving inland during the night, which is quite unusual. During the night the ground temperature is getting colder in comparison to sea surface temperature. Therefore, I would rather imagine a land breeze. In few words, what is dynamically explaining this inflow?

We suggest, the two counteracting effects "pressure difference" and "turbulence difference" determine the AI front and its propagation. During day the land is subject to stronger heating than the Gulf of Guinea, leading to stronger turbulence over land. The turbulence mixes the horizontal momentum of the monsoon flow vertically, impeding the monsoon flow and establishing a frontal structure near the coast. In the evening, the turbulence over land decreases allowing the pressure difference (pressure gradient in direction land-sea) to overcome the effects from turbulence. The front starts to penetrate inland, transporting the post-frontal air characteristics (cool air, low-level jet) inland. Therefore during night the monsoon flow (directed from ocean to land) over-compensates the land breeze that we would expect in the classical land-sea breeze concept. Please also refer to our companion paper in which we describe the mechanisms of AI in detail: Deetz, K., Vogel, H., Knippertz, P., Adler, B., Taylor, J., Coe, H., Bower, K., Haslett, S., Flynn, M., Dorsey, J., Crawford, I., Kottmeier, C., and Vogel, B.: Numerical simulations of aerosol radiative effects and their impact on clouds and atmospheric dynamics over southern West Africa, *Atmos. Chem. Phys.*, 18, 9767–9788, 2018. <https://www.atmos-chem-phys.net/18/9767/2018/acp-18-9767-2018.pdf>

(4) P7 L 15-24 : (a) The Aerosol Inflow involves an increase of RH a decrease of temperature but also brings different types of aerosols inland. You discuss the meteorological conditions that have for sure an influence on the ALWC but you never suggest that aerosol components may also have an impact. (b) Section 3.3 (Impact of aerosol modes): First, you should details the different types of aerosols that are predominant during each phase and the mean size distribution associated with each phase. (c) Do

Printer-friendly version

Discussion paper



you separate the aerosol modes in term of chemistry within your model? (d) It seems, according to P8 L25, that coarse mode is only made of sea salt particles. (e) How do you take into account dust then? (f) The comparison with chinese field campaigns need to be clarified. Are the different types of aerosols similar in China and Africa? (g) Did Chen et al. (2012) performed their measurements during the monsoon period?

We have separated this remark in subsections (a)-(g): (a) In a draft version of our manuscript we have had a further subsection that dealt with the effect of the aerosol composition on ALWC during the diurnal evolution. In fact, ACC is dominating in all three phases. In Phase 2 the ALWC contribution from ACC increases because the RH increases. The ALWC contribution from sea salt is generally higher during daytime (although more sea salt is transported inland during night). This is because sea salt also takes up water at RHs that are significantly below 95 % (daytime drying) which is not the case for the submicron particles within ISORROPIA II. Therefore during daytime sea salt has strongest contributions to the total ALWC. Although, the analysis of these aspects are interesting we decided to exclude it from this study for two reasons: - The discussion of the aerosol composition impact on ALWC is strongly dependent on how it is parameterized in the model. E.g. for sea salt we use the parameterization of Lundgren et al. (2013) which can lead to significant different results when using another parameterization. - Furthermore, the analysis of these aspects distract from the actual goal of this study. We wanted to find a relationship between the ALWC and its impact on the radiative transfer in shortwave and longwave. Section 3 is meant as a rather short transfer part that leads the reader to the core topic assessed in Section 4. Additionally it has to be considered that the ISORROPIA is based on the equilibrium solution. This works well in general but can also lead to substantial deviations. Water is a component of this equilibrium and therefore we cannot separately assess the impact of specific aerosol components on the ALWC.

(b) The manuscript points out that ACC is dominating in all Phases. In Figure E1 we now have added (in addition to the aerosol diameter) the aerosol number concentration

[Printer-friendly version](#)

[Discussion paper](#)



of the different modes (Review-figure-1).

(c) The aerosol treatment in COSMO-ART is described in detail in Vogel et al. (2009). All aerosol species in COSMO-ART (except of pollen and volcanic ash, which are not considered in this study) are allocated to lognormal aerosol modes. But of course the aerosols undergo aerosol chemistry (e.g. deposition of sulfuric acid on soot particles).

(d) No, COSMO-ART considers sea salt, mineral dust and coarse mode anthropogenic particles in the coarse mode. But with respect to ALWC, only sea salt is relevant within the coarse mode. Therefore this study focuses on sea salt in COARSE.

(e) Mineral dust is treated as chemical inert in COSMO-ART. Of course this is a shortcoming, because aged mineral dust in the atmosphere can also be subject to ALWC or other chemical reactions. These effects are not considered in COSMO-ART. It has to be considered that in the research period 2-3 July/ 6-7 July mineral dust plays no role in the monsoon layer.

(f) This aspect refers to a remark that came up already in the first review. Therefore I copy my thoughts and the revision at this place: When focusing on the study of Bian et al. (2014), the observations are related to the time period July-August 2009 and focusing on the chinese provinces Shandong, Hebei, Pekin and Tianjin. The climate in this area is in between humid subtropical and humid continental Summers are hot and rainy with temperatures around 24-28 °C in July with the precipitation maximum in summer via influences from the monsoon. A qualitative analysis of Terra Modis satellite images (of course only one overfly per day) revealed that in the 62 d period of July-August 2009 Shandon was fully covered by clouds on 55 d and partly covered by clouds on 7 days. Therefore the weather conditions during the DACCIWA campaign and HaChi campaign are very similar. Both studies focus on the NH summer. Both areas are located in the NH summer monsoon area with high temperatures and are very frequent covered by clouds. The measurement site for the study of Bian et al. (2014) is Wuqing. For this location, Liu et al. (2011) [Figure 3] shows measurements



of temperature and relative humidity for July-August 2009. Temperature variations are between 20 °C and 32 °C. Relative humidity variations are between 40 % (mostly 60%) and 95 %. The latter is similar to what is modeled for southern West Africa (Fig. 3 in our manuscript) and to what was observed in southern West Africa at Save supersite (Kalthoff et al., 2018, Fig. 3).

Wuqing is about 90 km away from the Gulf of Bohai. So also HaChi focuses on the area near the coast. Wuqing is surrounded by large cities (Peking (80 km away, 21.5 million inhabitants, megacity), Langfang (30 km away, 4.4 million inhabitants), Tianjin (40 km away, 15.5 million inhabitants, megacity), Tangshan (100 km away, 7.6 million inhabitants)). Also southern West Africa has several large cities especially near the coast. However, the populations are generally smaller but on the same order of magnitude (Lagos: 13.7 million inhabitants, Abidjan: 5 million inhabitants). Based on MODIS observations, Bian et al. (2014) show that the averaged AOD values are generally above 0.6 in the research area and 0.7 above Wuqing. For the DAccIWA region we found averaged MODIS AOD values of 0.4-0.7, slightly smaller to what was observed in the HaChi region. However, the validity over land is limited because southern West Africa is virtually always covered by clouds, restricting the observations to a few days.

Based on these findings we came to the conclusion that the general meteorological and aerosol conditions are similar for HaChi and DAccIWA and therefore allow a qualitative comparison e.g. of the ALWC values between both sites.

We added the following passage in the conclusions to account for your remark: "HaChi and DAccIWA both focus on the northern hemispheric monsoon season, capture coastal areas that are frequently covered by clouds, have similar temperature and relative humidity conditions (Liu et al., 2011; Kalthoff et al., 2018) as well as similar aerosol loadings (Bian et al. (2014); Deetz et al. (2018a), allowing for a qualitative comparison of modeled ALWC with measurements during HaChi."

(g) The study of Chen et al. (2012) mainly focus on January 2010 so not on the

[Printer-friendly version](#)

[Discussion paper](#)



monsoon period in contrast to Bian et al. (2012) and Liu et al. (2011).

(5) P10 Section 4.2 : In this section, you are using 3 different figures to describe the effect of ALWC on the shortwave, longwave radiations and 2-m temperature. (a) However, I felt like I did not have any explanations on what you observed. As an example, L16-18 'a decrease in SSR can be observed when considering ALWC for ICA and OCA'. Could you explain why you have the same order of magnitude for OCA and ICA (where the RH should be higher)? (b) 'A change in the cloud cover' → the cloud is disappearing or strengthening? These are examples, but the entire section is written the same way. (c) According to your conclusions it seems that the cloud presence doesn't affect much the effect of ALWC on radiation. Could you provide anywhere in your manuscript the meteorological and aerosol size distribution differences between OCA and ICA?

We have separated this remark in subsections (a)-(c): (a) We have applied two model realizations, one is the reference run in which the ALWC is considered in the radiative transfer calculations and the other run is the experiment ("No-ALWC") in which the ALWC is neglected in the radiative transfer. As expected, the incoming surface shortwave radiation (SSR) decreases when we consider ALWC in the radiative transfer. The median reduction is -28 W m⁻² for the in-cloud area (ICA) and -15 W m⁻² outside of clouds. As expected the reduction is higher in clouds because there the RH is higher and therefore the ALWC increases compared to areas outside of clouds. For ICA the reduction is twice as high as for OCA. It has to be considered that the radiative transfer is a two-stream model (just up and down). The intensity of an incoming beam that passes a certain column is reduced in case of ICA by the ALWC in clouds but also by the ALWC below and above the clouds. In case of OCA the light intensity is reduced only by ALWC outside of clouds in the total column. (I) Even in OCA the RH can reach very high values near 100 % and (II) in ICA the clouds mostly will span only a very small fraction of the total vertical column. (III) Most of the path in OCA AND ICA will be cloud free. The aspects (I-III) let deduce that the ALWC surplus from cloudy regions



can be high but nevertheless the difference in SSR between ICA and OCA will not be extraordinary high.

(b) We revised the corresponding sentence in the manuscript: "The positive values north of 8 °N in Phase 3 are related to a change in cloud cover (more clouds in Reference), which is not a general feature." If you have detect further imprecise statements, please specify.

(c) Figure E1 (see Review-figure-1) now shows the median aerosol number density for the separate modes on 3 July 2016 6 UTC in the lowest 1500m AGL. Furthermore, Review-figure-2 shows boxplots of the wet diameters for areas with a cloud water greater than zero (in clouds, ICA) and for areas with a cloud water equal zero (off clouds, OCA) also on 3 July 2016 6 UTC in the lowest 1500m AGL. For this time the meteorology (differences in temperature and RH) looks as follows: see Table presented in Review-figure-4.

Review-figure-2 is added in the manuscript as Figure E2 and we added the following passage in the end of Section 4.1: "For Reference on 3 July 6 UTC, Figure E2 shows the median wet diameter separated in ICA and OCA for the lowest 1500 m AGL over Ivory Coast, highlighting the effect that submicron particles (Fig. E2a) need a RH near 100 % to significantly grow, whereas sea salt (Fig. E2b) already shows a growth due to ALWC at lower RH values. The median temperature for ICA (OCA) is 20.9°C (21.7°C) and the median RH for ICA (OCA) is 99.9% (93.2%)."

Minor comments : (6) Page 2 L10 : replace sodium by sodium

We have changed the manuscript accordingly.

(7) Page 3 L14-16 : I'm not sure I understand this sentence. You claim : " The RH increasingly affects the relationship between the amount of aerosol and the cloud droplet number concentration". I believe that larger RH could involve more or larger cloud droplets. These results are not from 2015: :

[Printer-friendly version](#)

[Discussion paper](#)



We removed this passage and the citation because this is less relevant as you have described.

ACPD

(8) Page 3 L28 : I believe that there were no GF measured during AMMA.

We have corrected the citation.

(9) P5 L4 : Could 5% of the mass concentration of soot particle be defined considerable ?

We have rephrased this sentence.

(10) P5 L16-17 : 'Furthermore, : : : process studies'. I do not understand this sentence. The undisturbed monsoon condition favor NLLS presence? Also, NLLS is not defined in the acronym list.

We removed the "and" in the corresponding sentence. Yes, undisturbed monsoon conditions favor the process studies, because then the conditions are very similar from day to day, making a short simulation period qualitatively representative for longer time periods. Undisturbed monsoon conditions also favor NLLS presence because e.g. the passage of an MCS can disturb the NLLJ and with that the evolution of NLLS. We added NLLS in the acronym list.

(11) P5 L28 : please remove 'by a a decrease'

We have changed the manuscript accordingly.

(12) P9 section 3.4 : Is this AOD within cloud ? Are you talking about interstitial aerosols? Then the clouds are just considered as a vector for RH increase? There are numerous studies that have shown the contribution of the ALWC to the total AOD (Brock et al., 2015 and 2016; Crumeyrolle et al., 2014; Beyersdorf et al., 2016; Orozco et al. 2016; Eck et al. 2014).

Yes, we consider clouds as areas where the RH maximizes. And here we don't focus on cloud optical thickness but on the radiative effects that come from the ALWC. Yes,

Interactive comment

Printer-friendly version

Discussion paper



you can term it interstitial aerosol. It is right that this effect was already analyzed in several former studies. Nevertheless, the topic is still relevant. The weather forecast model COSMO (not the research model COSMO-ART) still does not consider this effect when calculating the radiative transfer. This study is also meant as a motivation for the model developer to consider these effects, especially when they do forecasts in moist tropical regions. We have not stated that our finding about the strong impact of ALWC on AOD is completely new. We just highlighted this finding as a step towards the subsequent analysis of the ALWC - radiation relationship. But we added the following passage in the introduction to consider your remark: "Several studies analyzed the implication of ALWC to AOD (e.g. Brock et al. 2016, Beyersdorf et al. 2016). Brock et al. (2016) combine aircraft observations with a simple model to analyze the sensitivity of the AOD towards meteorological and aerosol properties in the southeastern United States. The results indicate highest (lowest) sensitivities towards RH (dry and wet aerosol refractive index)."

(13) P12 L22 : please remove 'The' : 'on THE one hand'

"On the one hand ... on the other hand ..." is a fixed term. Please specify if we misunderstood your remark.

(14) P13 L3 : please replace 'AI affected' - 'AI affects'

We have changed the manuscript accordingly.

(15a) Figure 4 : I'm sure this is a typo : ' same ass '

We have changed the manuscript accordingly.

(15b) Relative ALWC should be a proxy for the hygroscopicity of aerosols right ? If yes then it needs to be stated somewhere. And you should present mean aerosol size distribution before this figure for the different phases.

We added the following sentence in the introduction: "The relative ALWC can be seen as a proxy for the hygroscopicity of an aerosol species." Figure D1 shows the median

Interactive
comment

mass concentration of the single aerosol species, Figure E1 (Review-figure-1) presents the median number concentration as well as dry and wet diameters. Furthermore figure E2 (Review-figure-2) is added to separate the analysis of dry and wet diameters to ICA and OCA. We disagree that a further analysis of the aerosol size distribution, now separated in the three AI phases, is appropriate. Adding more and more figures will distract the reader from the main outcomes and also contradicts your remark (1).

(16) Figure 5 : You should add on the different figures 'TOTAL' , 'AIT', 'ACC' and 'COARSE'

We have adapted the figure accordingly.

(17) Figure 6 : Could you add the RH on this figure ?

We have adapted the figure accordingly (see Review-figure-3).

(18) Figure 9/10/11 : Could you add on the figure ICA and OCA . I'm sure that will also be clearer if there is REF and REF-No_ALWC

We have adapted the figure accordingly.

Interactive comment on *Atmos. Chem. Phys. Discuss.*, <https://doi.org/10.5194/acp-2018-420>, 2018.

[Printer-friendly version](#)

[Discussion paper](#)



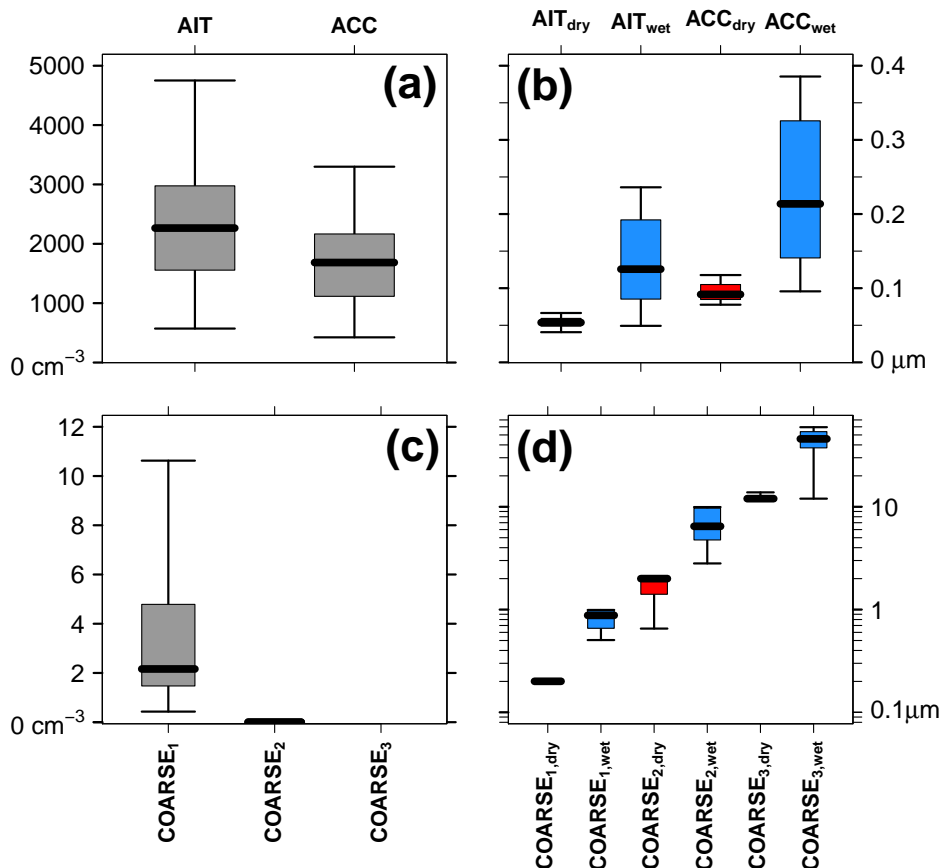


Fig. 1. Boxplots of (a) aerosol number density (cm^{-3}) and (b) dry (red) and wet (blue) aerosol diameters (μm) for AIT and ACC and boxplots of (c) aerosol number density (cm^{-3}) and (d) dry and wet diameter.

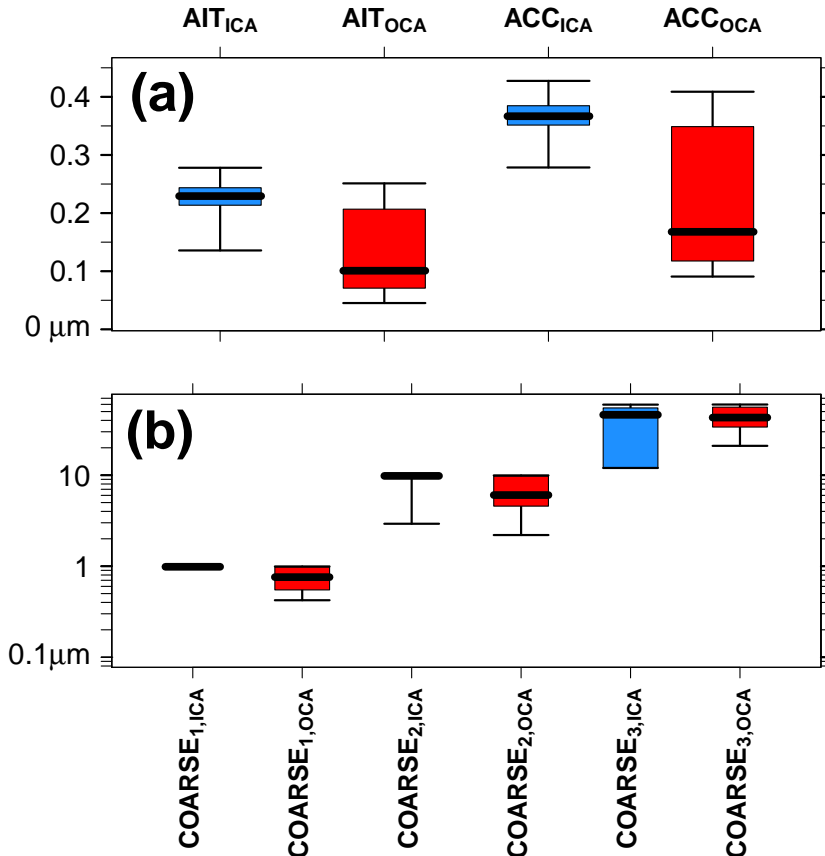


Fig. 2. Boxplots of aerosol wet diameters (μm) for (a) AIT and ACC and (b) COARSE, splitted in the three COSMO-ART sea salt modes as median in the lowest 1500 m AGL on 3 July, 6 UTC by separating in ICA/OCA.

Printer-friendly version

Discussion paper



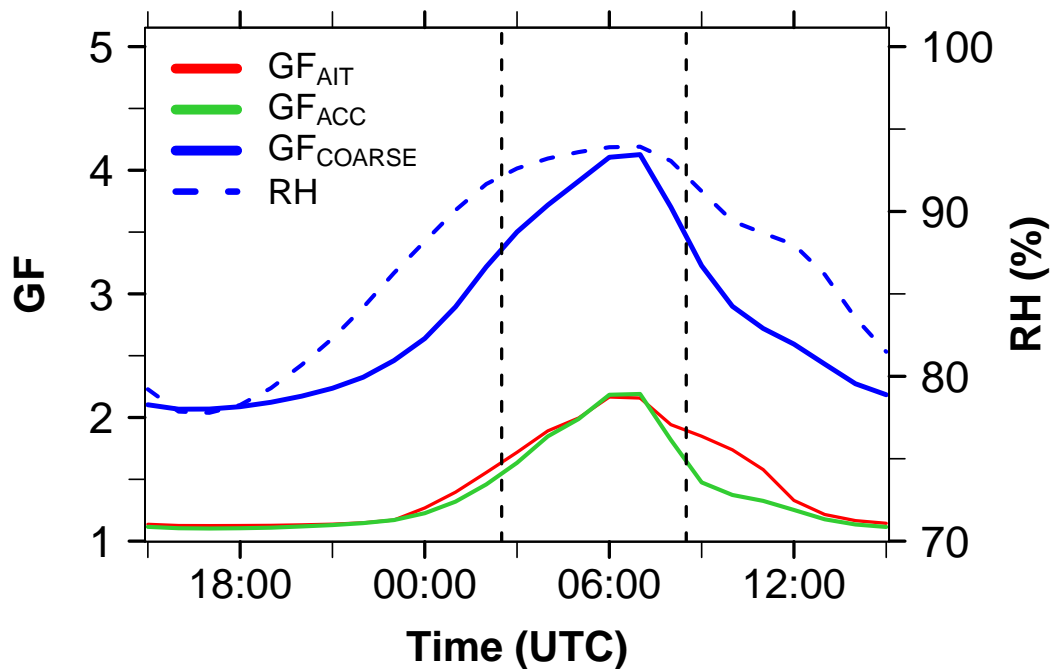


Fig. 3. Diurnal cycle of the median GF (%) of GF_{AIT} (red), GF_{ACC} (green), GF_{COARSE} (blue) and RH (%) (blue dashed) in the lowest 1500 m AGL over Ivory Coast (7.5° W–3° W, 4–10° N) on 2–3 July.

[Printer-friendly version](#)

[Discussion paper](#)



	in clouds		off clouds	
Temperature °C (median and standard deviation)	20.9	2.0	21.7	2.3
RH % (median and standard deviation)	99.99	1.4	93.2	4.9

Fig. 4. Table summarizing the meteorological conditions on 3 July 2016 6 UTC for "in clouds" (ICA) and "off clouds" (OCA) in the lowest 1500m AGL.

[Printer-friendly version](#)[Discussion paper](#)

Interactive comment on “Aerosol liquid water content in the moist southern West African monsoon layer and its radiative impact” by Konrad Deetz et al.

Konrad Deetz et al.

konrad.deetz@kit.edu

Received and published: 4 August 2018

Answer to Referee #2b Konrad Deetz 23 July 2018

Dear Referee (Atmospheric Chemistry and Physics),

thank you for your supplementary report from 10 July 2018. We have accounted for the additional comment in the revised manuscript version. Please find our reply (marked with #) in the following.

Sincerely, Konrad Deetz on behalf of all coauthors

Referee comments: (1) It's not clear if the radiative effect of the ALWC is calculated

only from an increase of the aerosol size or if the refractive index is changing with the water uptake ?

ACPD

Interactive comment

We see your point. We suggest that the radiative effect of the ALWC is a combination of effects from the aerosol size increase and the change in the refractive index. Both effects are considered in COSMO-ART but in the model output we do not disentangle them. Although, this is an interesting aspect, it is beyond the scope of our study, which aims on the general quantification of the impact of ALWC on the radiative transfer. To account for your remark, we added the following paragraph in the conclusion section: "It is expected, that the radiative effect of the ALWC is determined by a combination of the aerosol size increase and the corresponding change of the refractive index. Although it would be interesting to assess the contribution of each process, this is beyond the scope of this work and has to be left for future studies."

Interactive comment on Atmos. Chem. Phys. Discuss., <https://doi.org/10.5194/acp-2018-420>, 2018.

[Printer-friendly version](#)

[Discussion paper](#)



List of relevant changes:

- Figure adaptions to improve readability, understanding (Fig.1, Fig. 2, Fig. 5, Fig. 6, Fig. 9-11)
- Add more details with respect to the comparability of DAccIWA and HaChi with respect to ALWC
- Add also boxplots for median aerosol number concentrations in Figure E1
- Add a figure that assesses the differences of the aerosol diameter in clouds and off clouds
- Assessment of the relevance of outliers in the ALWC-radiation relationship analysis

Aerosol liquid water content in the moist southern West African monsoon layer and its radiative impact

Konrad Deetz¹, Heike Vogel¹, Sophie Haslett², Peter Knippertz¹, Hugh Coe², and Bernhard Vogel¹

¹Institute of Meteorology and Climate Research, Karlsruhe Institute of Technology (KIT), Karlsruhe, Germany

²National Centre for Atmospheric Science, and School of Earth and Environmental Sciences, University of Manchester, Manchester, United Kingdom

Abstract.

Water uptake can significantly increase the size and therefore alters the optical properties of aerosols. In this study, the regional-scale model framework COSMO-ART is applied to Southern West Africa (SWA) for a summer monsoon process study on 2–3 and 6–7 July 2016. The high moisture and aerosol burden in the monsoon layer makes SWA favorable to 5 quantify properties that determine the aerosol liquid water content and its impact on radiative transfer. Given the marked diurnal cycle in SWA, the analysis is separated into three characteristic phases: (a) *Atlantic Inflow progression phase* (15-2 UTC), when winds from the Gulf of Guinea accelerate in the less turbulent evening and nighttime boundary layer, (b) *Moist morning phase* (3-8 UTC), when the passage of the Atlantic Inflow front leads to overall cool and moist conditions over land and (c) *Daytime drying phase* (9-15 UTC), in which the Atlantic Inflow front re-establishes with the inland heating 10 initiated after sunrise. This diurnal cycle imprints, via the relative humidity, also the aerosol liquid water content. We analyzed the impact of relative humidity and clouds on the aerosol liquid water content. As shown by other studies, the accumulation mode particles are the dominant contributor of aerosol liquid water. We find aerosol growth factors of 2 (4) for submicron (coarse) mode particles, leading to a substantial increase of mean aerosol optical depth from 0.2 to 0.7. Considering the aerosol liquid water content leads to a decrease in shortwave radiation of about 20 W m^{-2} , while longwave effects 15 appear to be insignificant, especially during nighttime. The estimated relationships between total column aerosol liquid water and radiation are $-305 \pm 39 \text{ W g}^{-1}$ (shortwave in-cloud), $-114 \pm 42 \text{ W g}^{-1}$ (shortwave off-cloud) and about -10 W g^{-1} (longwave). The results highlight the need to consider the relative humidity dependency of aerosol optical depth in atmospheric models, particularly in moist tropical environments, where their effect on radiation can be very large. [List of acronyms used in this study](#)

Acronym Description

ACC Accumulation mode
ADE Aerosol Direct Effect
AGL Above Ground Layer
AI Atlantic Inflow
AIE Aerosol Indirect Effect
AIT Aitken mode
ALWC Aerosol Liquid Water Content
AOD Aerosol Optical Depth
ASL Above Sea Level
CDNC Cloud Droplet Number Concentration
COARSE Coarse mode
COSMO-ART Consortium for Small-scale Modeling – Aerosol and Reactive Trace gases
DACCIAWA Dynamics-aerosol-chemistry-cloud interactions in West Africa
DWD Deutscher Wetterdienst (German Weather Service)
ECDF Empirical Cumulative Distribution Function
GF Growth Factor
GRAALS General Radiative Algorithm Adapted to Linear-type Solutions
radiation scheme
HaChi Haze in China campaign
ICA In-Cloud Area
ICON Icosahedral Nonhydrostatic Model
No-ALWC Model realization neglecting ALWC in the radiation calculation
OCA Off-Cloud Area
PBL Planetary Boundary Layer
POA Primary Organic Aerosol
Referencee Reference

ease model realization with considering ALWC in the radiation calculation RH Relative Humidity SCT Stratus-to-cumulus transition SLR Surface Longwave (net) Radiation SOA Secondary Organic Aerosol SSR Surface Shortwave (net) Radiation SST Sea Surface Temperature SWA Southern West Africa WAM West African Monsoon

1 Introduction

5 Water can significantly contribute to the total aerosol mass. While at low relative humidities (RH) the inorganic salts of an aerosol particle are solid, the particle spontaneously starts taking up water when exceeding a composition-specific RH, the *deliquescence relative humidity (DRE)* (Seinfeld and Pandis, 2006). The aerosol liquid water content (ALWC) thereby affects the aerosol physicochemical and optical properties, which have the potential for significant impacts on the aerosol direct effect (ADE) (e.g. Jung et al., 2009).

10 The hygroscopic growth factor GF is a frequently used measure to describe the aerosol hygroscopicity via the ratio between the wet aerosol diameter at a specific RH $d_{p,wet}(RH)$ and the dry aerosol diameter $d_{p,dry}$ (e.g. Chen et al., 2012). Furthermore, the relative ALWC is defined as the ratio between ALWC and the dry aerosol volume V_{dry} to assess the mass of water that is taken up by a unit volume of dry aerosol (e.g. Bian et al., 2014). The relative ALWC can be seen as a proxy for the hygroscopicity of an aerosol species.

15 In terms of ALWC, the understanding of aerosol effects on clouds and radiation is hindered by (a) the complexity in the reproduction of ALWC in observations and modeling under high RH (e.g. Bian et al., 2014) and (b) the covariance of cloud properties and aerosol water uptake with similar meteorological variables (e.g. RH; Andersen and Cermak, 2015). In atmospheric aerosol modeling the thermodynamic equilibrium model ISORROPIA II (Fountoukis and Nenes, 2007) is widely used (e.g. COSMO-ART, GEOS-Chem and LOTOS-EUROS), describing the chemical equilibrium between the gas, liquid and solid

20 phases for the aerosol system containing the inorganic ions potassium, magnesium, natriumsodium, sulfate, nitrate, chloride and water. The ALWC is derived by using the Zdanovskii, Stokes and Robinson (ZSR) mixing rule (Stokes and Robinson, 1966). Hygroscopicity measurements can be obtained e.g. via the *High Humidity Tandem Differential Mobility Analyzer* (HH-TDMA, Hennig et al., 2005) for 90–98.5 % RH. Estimations of the aerosol hygroscopicity are also possible via the combination of observed aerosol number size distributions and aerosol compositions from aerosol mass spectrometers. Using the ZSR mixing rule the GF can be derived (e.g. Aklilu et al., 2006).

25 Several measurement campaigns and modeling efforts have addressed the ALWC and its impact on aerosol chemistry, visibility and the radiative transfer. Zieger et al. (2017) assess the effect of hygroscopicity of sea salt on AOD with a global model approach. They modeled latitudinal averaged reductions in the AOD of up to 14 % when reducing the hygroscopicity of sea salt from 1.5 to 1.1. Several studies analyzed the implication of ALWC to AOD (e.g. Brock et al., 2016; Beyersdorf et al., 2016).

30 Brock et al. (2016) combine aircraft observations with a simple model to analyze the sensitivity of the AOD towards meteorological and aerosol properties in the southeastern United States. The results indicate highest (lowest) sensitivities towards RH (dry and wet aerosol refractive index).

The most comprehensive project in this regard to date in the research field of ALWC is the *Haze in China (HaChi) campaign*

in 2009. The scientific results are comprised in the ACP special issue "Haze in China (HaChi 2009–2010)". HaChi focused on the North China Plain between the megacities Beijing and Tianjin. The results indicate significant diurnal variations in the aerosol physicochemical properties, including the aerosol scattering and absorption coefficient (high in the morning, low in the evening; Ma et al., 2011) and aerosol hygroscopicity (high during daytime, low during nighttime; Liu et al., 2011), both due to

5 Planetary Boundary Layer (PBL) evolution and direct particle emissions. Chen et al. (2012) identify two haze regimes: below 90 % RH the haze is caused by high aerosol volume concentrations and above 90 % RH ALWC dominates the haze. Based on the HaChi observations, Kuang et al. (2015) conclude that the diurnal cycles of the optical properties single-scattering albedo and asymmetry parameter differ when considering ambient or dry aerosol. For ambient aerosol, maximum (minimum) values are reached after sunrise (in late afternoon), correlated with the RH, whereas for dry aerosol, maximum values are detected at

10 noon and minimum values in the morning and evening. Kuang et al. (2015) emphasize that the diurnal variations in the optical properties can significantly alter the ADE. Bian et al. (2014) estimate the maximum (average) value of ALWC in HaChi to be 971 (169) $\mu\text{g m}^{-3}$ related to a diurnal cycle with minimum values during day and maximum values during night. Due to the high aerosol number and their hygroscopicity from aging and cloud processing, the ALWC contribution from the accumulation mode is dominating. For RH above 60 % the ALWC observations are in good agreement with the values derived

15 from ISORROPIA II model. Liu et al. (2011) assess the hygroscopic properties of aerosol particles at high relative humidities and their diurnal variations in the North China Plain. They find average growth factors of 1.57-1.89 regarding dry diameters of 50-250 nm in a 95 % RH environment. For the highly hygroscopic particles a size increase by a factor of 2.1-2.8 (98.5 % RH) compared to the dry diameter is reached. Liu et al. (2011) highlight that this behavior can significantly increase the light scattering.

20 Aside from HaChi also the *Program of Regional Integrated Experiment of Air Quality over Pearl River Delta (PRIDE-PRD)* focused on the air pollution in China including aerosol hygroscopicity. The ALWC effect on the total light-extinction coefficient is estimated to be 34.2 %, with contributions from ammonium sulfate (25.8 %), ammonium nitrate (5.1 %) and sea salt (3.3 %) (Jung et al., 2009). Jung et al. (2009) highlight the sensitivity of the scattering and extinction coefficients as well as the mass-scattering efficiency and single-scattering albedo towards the ALWC. The modeling study of Cheng et al. (2008) for the

25 same region reveals an aerosol-related cooling in the lower PBL, in which 40 % of the cooling effect is related to ALWC at 80 % RH.

The western Canadian aerosol study of Aklilu et al. (2006) reveals that the particle hygroscopicity is dominated by the availability of sulfate, since sulfate and *GF* show significant correlations. Low *GF* are detected for air masses affected by urban pollution. Aklilu et al. (2006) suggest that this is related to the primary organics that are less oxidized than secondary organics

30 (e.g. Alfarra et al., 2004). Furthermore, Aklilu et al. (2006) underline the failing of the ZSR mixing rule for particulate nitrate that is subject to a considerably smaller water uptake than ammonium nitrate.

Andersen and Cermak (2015) analyze ten years of satellite-derived aerosol and cloud products and ERA-interim data over the Southeast Atlantic and find out that in very humid conditions (RH > 90) the RH increasingly affects the relationship between the amount of aerosol and the cloud droplet number concentration. However, Andersen and Cermak (2015) also stress that the biomass burning aerosol in this area is mostly situated above the cloud layer such that the boundary layer humidity might

35

~~not be representative for the humidity in the aerosol layer.~~ Eastern China's tremendous air pollution makes it favorable for the study of ALWC, but a rapid growth of population and economy has also lead to a significant increase in atmospheric pollutants in Southern West Africa (SWA). Although SWA shows aerosol loadings similar to what is observed in East China (e.g. Hsu et al., 2017), the ALWC and its impacts on the visibility and radiative transfer have not been explored until now.

5 Also SWA frequently shows a hazy milky sky even without the presence of clouds or the occurrence of a mineral dust event (personal observations by the authors), raising the question about the "Haze in SWA". First insights into West African ALWC characteristics are provided by observations obtained during the *African Monsoon multidisciplinary Analysis* (AMMA, Re-delsperger et al., 2006). Matsuki et al. (2010) conclude that freshly emitted biomass burning aerosol is rather hydrophobic, whereas aging processes transform them into more hygroscopic particles. The aged biomass burning plumes, transported from

10 Central to West Africa over the Atlantic Ocean (Mari et al., 2008), consist of highly hygroscopic particles with $GF > 1.2$ ([Matsuki et al., 2010](#)) ([Maßling et al., 2003](#)). Crumeyrolle et al. (2008) even see evidence for the coating of dust particles with soluble elements in Mesoscale Convective Systems enhancing their hygroscopicity and making them favorable as cloud condensation nuclei (CCN). However, the spatial focus of AMMA was on the Sahelian region and it is expected that the conditions

15 farther south, over the coastal region of the Gulf of Guinea with its large urbanized areas and generally higher RH, differ substantially.

Furthermore, SWA is characterized by frequent nocturnal low-level stratus (NLLS) and stratocumulus (e.g. Schrage and Fink, 2012; Schuster et al., 2013; van der Linden et al., 2015; Adler et al., 2017) that have significant influence on the radiation budget (e.g. Hill et al., 2017). This study builds on the work of Deetz et al. (2018) that analyzes the impact of aerosol on the properties of the Atlantic Inflow (AI) and Stratus-to-cumulus transition (SCT) by focusing on Ivory Coast. Deetz et al. (2018)

20 highlight the dominance of the ADE and Twomey effect in the observed changes. The present study extends the aerosol impact analysis to the effects of ALWC on aerosol properties and the radiative transfer, because the model results analyzed in Deetz et al. (2018) reveal significantly enhanced Aerosol Optical Depth (AOD) in high RH regimes over SWA.

The goals of this study are: (1) to quantify the diurnal evolution of the ALWC-related properties and to assess whether diurnal recurring structures can be observed, which allow generalizing the results, (2) to evaluate the ALWC impact on radiative

25 transfer, also in terms of their relevance to atmospheric modeling and (3) to derive robust relationships between ALWC and the change in radiative transfer.

HaChi and DACCIAWA both focus on the northern hemispheric monsoon season, capture coastal areas that are frequently covered by clouds, have similar temperature and relative humidity conditions (Liu et al., 2011; Kalthoff et al., 2018) as well as similar aerosol loadings (Bian et al., 2014; Deetz, 2018), allowing for a qualitative comparison of modeled ALWC with

30 measurements during HaChi. This also contributes to broaden the view of ALWC-radiation interactions to a highly polluted area other than Eastern China, an area that additionally is affected by the West African Monsoon (WAM) and its intense on-shore moisture transport.

This study is structured as follows: In Section 2 the model framework as well as the research area are introduced. The results comprise an analysis of atmospheric dynamics and thermodynamics affecting the ALWC (Sect. 3) and a detailed assessment

35 of the radiative impact from ALWC (Sect. 4). The study concludes with a summary and evaluation of the findings (Sect. 5).

2 Model framework and setup

For this study, the regional-scale model framework COSMO-ART (Consortium for Small-scale Modeling - Aerosols and Reactive Trace gases, Vogel et al., 2009) is used. COSMO-ART is based on the operational weather forecast model COSMO (Baldauf et al., 2011) of the German Weather Service (DWD). The ART extensions allow for an online treatment of aerosol dynamics and atmospheric chemistry. This study accompanies the analysis of Deetz et al. (2018) using the same basic model setup, time period and spatial focus. The SWA model domain (2.5 km grid mesh size) comprises Ivory Coast, Ghana, Togo, Benin and the Gulf of Guinea (red rectangles in Fig. 1). ~~(a) Modeling domain SWA (red rectangle, 2.5 km grid mesh size) together with its coarse domain (blue, 5 km grid mesh size). (b) Map of the research area SWA. The color shading denotes topography (m Above Sea Level, ASL). Topographic features are named in bold, coastal cities are shown as blue dots and the three DACCIA supersites as red dots. The modeling domain SWA is again denoted as red rectangle. Figure adopted from Deetz et al. (2018).~~ The SWA domain is nested into a coarse domain (blue rectangle in Fig. 1a) with a grid mesh size of 5 km to capture pollutants of mineral and biomass burning origin. The subsequent study will focus on the results of the red domain. The coarse domain is using ICON operational forecasts (approximately 13 km grid spacing) as meteorological boundary conditions. These cover the time period 25 June to 3 July to allow for an aerosol-chemistry spin up. The meteorological state is initialized every day at 0 UTC. COSMO-ART considers 12 lognormal aerosol modes: (1) Aitken mode, (2) Aitken mode containing a soot core, (3) accumulation mode, (4) accumulation mode containing a soot core, (5) pure (fresh) soot, (6) coarse mode of anthropogenic origin, ~~(7–107–9)~~ coarse modes of marine origin (3 modes) and ~~(11–1310–12)~~ coarse modes of mineral origin (3 modes). In the following, three aggregated modes are considered: AIT (Aitken mode, (1)+(2)), ACC (Accumulation mode, (3)+(4)) and COARSE (Coarse mode of marine origin, (7)+(8)+(9)). Pure soot as well as the coarse mode of anthropogenic and mineral origin are not considered, since their contribution to ALWC is either not considered in COSMO-ART or the contribution is negligible. The model setup is summarized in Appendix A.

In COSMO/COSMO-ART the radiation scheme *General Radiative Algorithm Adapted to Linear-type Solutions radiation scheme* (GRAALS; Ritter and Geleyn, 1992) is used. Without the ART extensions, GRAALS considers aerosol climatologies (Tegen et al., 1997) instead of prognostic aerosol. In this case the aerosol is treated as dry and all effects emerging from the ALWC are neglected ~~(B. Bodo Ritter, personal communication, 2018)~~. In contrast, COSMO-ART is able to derive the ALWC and its impact on the radiative transfer. With respect to anthropogenic aerosol the ALWC is calculated by ISORROPIA II (Fountoukis and Nenes, 2007). Fresh soot is treated separately but is also related to an uptake of water, namely via the condensation of sulfuric acid on the particle. Nevertheless, this contribution is negligibly small, since a soot particle with a ~~considerable~~ mass fraction of sulfuric acid ~~(more than that exceeds 5 %)~~ is shifted from the fresh soot mode to aged (internally mixed) aerosol treated by ISORROPIA II. Therefore we will not address to the ALWC from fresh soot in the subsequent analysis. In terms of sea salt, the ALWC is parameterized via Lundgren (2010). The coarse mode aerosols of anthropogenic and mineral origin are not related to ALWC in COSMO-ART and therefore also neglected in the following.

It has to be considered that activated aerosol particles are not removed from the aerosol distribution, which could lead to potential double counts in the radiative transfer calculations. Prior approaches to remove the activated aerosol leads to a rapid

and unrealistic cleaning of the atmosphere. With the model configuration denoted in Table 3, two realizations are performed: *Reference* considers ALWC in the calculation of the radiative transfer, whereas *No-ALWC* neglects this component. The difference between both realizations allows for a quantification of the changes in aerosol properties and their radiative effects in the monsoon layer.

5 The time period 2–3 July 2016 was selected due to the intense and persistent NLLS as observed at the Savè supersite (Kalthoff et al., 2018). Furthermore, 3 July is the center of the monsoon *Post-onset phase* (22 June – 20 July; Knippertz et al., 2017) and it is expected that the undisturbed monsoon condition favor ~~and~~ the process studies. Since the meteorological conditions show less variation from day to day, it is assumed that, even with a focus on a very short time period, insight can be achieved that can be generalized at least qualitatively to the length of the *Post-onset phase*. Nevertheless, we added results from the time period
10 6–7 July to assess the robustness of our findings.

3 Quantities affecting the ALWC

3.1 Impact of Atlantic Inflow (AI)

The studies of Adler et al. (2017) and Deetz et al. (2018) reveal a regular occurrence of the phenomenon *Atlantic Inflow (AI)* over SWA. AI involves a coastal front that develops during daytime and propagates inland in the evening. The AI front marks
15 the location of strongest horizontal gradients, with significantly higher wind speeds and lower potential temperatures post-frontally. The post-frontal area is affected by the nocturnal low-level jet (NLLJ) with a jet axis around 250 m Above Ground Layer (AGL). Furthermore, the post-frontal airmass is characterized by higher RH than the pre-frontal area. Therefore the AI front passage is characterized by a ~~a~~ decrease in temperature and an increase in RH and wind speed. By adapting the method proposed by Grams et al. (2010), Deetz et al. (2018) identify the front in the model output by the location at which a specific
20 isentrope of potential temperature θ_s (302 K) crosses a specific height h_s (250 m AGL). Especially over the flat terrain in Ivory Coast a coherent coast-parallel frontal pattern can be observed. Therefore in the following the spatial focus is set to Ivory Coast.

AI is the underlying meteorological process affecting all measures relevant for ALWC, such as RH and the meridional transport of specific aerosol types in the levels below 1 km AGL. It will be shown that the diurnal cycle of RH is not only thermodynamically (radiative cooling) but also dynamically driven (cold air advection via AI). In fact, it is a superposition of both effects, which are hard to disentangle. The AI impact will be included in the following analysis by taking into account the AI front locations. A detailed assessment of the spatiotemporal properties of AI and its aerosol sensitivity is presented in Deetz et al. (2018), based on the same model setup and time period as used for this study. Subsequently, we focus on the time period 15 UTC to 15 UTC of the following day to capture a full diurnal cycle starting with the time of the inland propagation of the AI front. As described in Deetz et al. (2018), a decrease in surface heating leads to a deceleration of the inland propagation of the AI front. Although this mechanism is assessed in detail in Deetz et al. (2018) and will therefore not be in the focus of this study, we need to be aware of similar effects that could arise from changing the representation of ALWC in the radiative calculations. An analysis of the frontal position reveals that the consideration of the ALWC leads to an AI front ahead of the *No-ALWC*

front by about 6–7 km on 2–3 July between 15 UTC and 22 UTC (similar for 6–7 July). It is hypothesized that including the ALWC leads to a daytime inland cooling that reduces the turbulence over land and favors the earlier onshore propagation of the AI front. Possibly, also reduced nighttime longwave cooling due to ALWC can favor the persistence of the local heat low inland that accelerates the front. With respect to 2 July 22 UTC and by comparing with the findings of Deetz et al. (2018), the 5 displacement amplitude is 2.5 times smaller than the displacement from reducing the aerosol amount by a factor of 10. Since the frontal displacement is small and virtually constant in time, the following study will not further assess this aspect.

3.2 Impact of Relative Humidity (RH)

COSMO-ART shows reasonable results in numerous comparisons with other DAccIWA observations (e.g. Deetz, 2018; Deetz et al., 2018). Unfortunately, no aircraft observations are obtained on 3 and 4 July over Ivory Coast during the DAccIWA 10 campaign and the aircraft payload does not include devices to directly measure ALWC. For this study, radiosoundings of Lamto and Abidjan (Maranan and Fink, 2016) are used to compare observed RH vertical profiles with the COSMO-ART results. The intercomparison is presented in Appendix B. Generally, better agreement is achieved in the inland station Lamto (Fig. 16) than in the coastal station Abidjan (Fig. 17 and 18), likely due to the more complex boundary layer structure near the coast. The intercomparison show times with very good agreement (especially during night on 3 July (Fig. 17g,h) and on 6 July 15 at Lamto (Fig. 16a,b)). Interestingly, these times with good agreement simultaneously denote an agreement in the AI-related low-level moisture increase during night. Significant underestimations frequently occur approximately above 1000 m AGL (e.g. on 6 July 23 UTC at Abidjan (Fig. 18d)). In general, COSMO-ART is able to reasonably reproduce the RH vertical profile over Ivory Coast. The tendency of the model to underestimate RH implies that the model-derived ALWC is a lower limit that can actually be higher in the field.

20 Figure 2 presents first insight in the diurnal cycle of RH (Fig. 2a) and ALWC (Fig. 2b) via spatial mean vertical profiles in the monsoon layer over Ivory Coast. Generally moist conditions ($\text{RH} > 70\%$) can be observed over the area of interest (Fig. 2a). From 15 UTC to about 0 UTC the maximum RH is located at or above 1000 m AGL. For the layer below 750 m AGL a significant increase in RH is visible from 15 UTC (below 75 %) to 9 UTC on the next day (above 95%). In the following, it will be shown that this is related to the onshore advection of air with higher RH (colder air) within the AI. Highest RH on 25 the order of 95 % are reached between 3 UTC and 12 UTC in the lowest 1500 m AGL. This is reflected in the vertical profile of ALWC, showing highest values consistent with RH (Fig. 2b), with remarkable diurnal variations encompassing two orders of magnitude. Therefore it can be deduced that ALWC is most sensitive to the morning hours (sunrise in Abidjan is around 6 UTC (6 local time)). Based on Figure 2 we focus on the lowest 1500 m AGL in the following, capturing the monsoon layer. The DAccIWA measurement campaign reveals that the monsoon layer over SWA shows typical heights of about 1900 m AGL 30 (Kalthoff et al., 2018). ~~Vertical profiles (m AGL) of (a) RH () and (b) ALWC ($\mu\text{g m}^{-3}$) for the median over Ivory Coast (7.5° W–3° W, 4–10° N) between 2 July 15 UTC (black solid) and 3 July 15 UTC (black dashed). Consider the logarithmic abscissa of (b).~~ As denoted in Section 2, the ALWC calculation for secondary inorganic particles in COSMO-ART is treated using ISORROPIA II. Bian et al. (2014) showed that robust results for the ALWC can be expected from ISORROPIA II for $\text{RH} > 60\%$. As presented in Figure 2, the average conditions over Ivory Coast reveal RH above 70 %. Therefore, principally we also

can expect robust results for SWA. Figure 3 shows a Hovmöller diagram for the median RH (Fig. 3a) and total ALWC (Fig. 3b) in the lowest 1500 m AGL as zonal means over Ivory Coast (7.5° W– 3° W, 4 – 10° N) between 2 July 15 UTC and 3 July 15 UTC. The black bars denote the location of the 302 K isentrope at 250 m AGL that is used for the frontal detection between 15 UTC and 22 UTC (Deetz, 2018). ~~Hovmöller diagram of the median (a) RH () and (b) total ALWC ($\mu\text{g m}^{-3}$) in the lowest 1500 m AGL as zonal mean over Ivory Coast (7.5° W– 3° W, 4 – 10° N) between 2 July 15 UTC and 3 July 15 UTC. The horizontal bars denote the zonal mean location of the 302 K isentrope at 250 m AGL, the horizontal solid line the zonal mean coast line and the vertical dashed lines separate the three phases: *AI progression phase* (Phase 1), *Moist morning phase* (Phase 2) and *Daytime drying phase* (Phase 3).~~ In the first half of the presented time period a clear separation between the pre-frontal inland area (north of the black bars in Fig. 3a) with relatively low RH and the post-frontal area (south of the black bars in Fig. 3a) with relatively high RH can be observed. The inland propagation of the front after 2 July 15 UTC is related to advection of cooler post-frontal air. In the following, this time period is denoted as Phase 1 (*AI progression phase*, 15–2 UTC). After the front has passed the area, the conditions are overall moist, revealing RH generally above 90 % (Phase 2, *Moist morning phase*, 3–8 UTC). After sunrise (6 UTC) the RH decreases again due to temperature increase and lifting of the stratus layer. Until 15 UTC the AI front re-establishes. This time period is denoted as Phase 3 (*Daytime drying phase*, 9–15 UTC). The comparison of Figure 3a and Figure 3b underlines that RH governs the spatiotemporal pattern of ALWC. Highest ALWC values are reached in Phase 2 and especially in the hilly terrain north of 7.5° N (Fig. 3b). The AI front denotes a clear border of a non-negligible ALWC regime post-frontally and negligible ALWC pre-frontally. The study of Bian et al. (2014) found average ALWC values of about 170 g m^{-3} for the North China plain, which is on the same order of magnitude as presented in Figure 3b.

In Phase 1 a cloud band develops behind the front which intensifies north of 7.5° N due to orographic lifting as visible in the high RH in the Hovmöller diagram after 0 UTC. After 21 UTC further clouds, originating from the Gulf of Guinea, propagate inland. This is reflected in the high RH after 21 UTC south of approximately 6.5° N. Figure 3 reveals the strong impact of atmospheric dynamics, in particular AI, on the spatiotemporal evolution of RH. This is most pronounced in Phase 1. Without AI and the land-sea contrast, a zonally more homogeneous pattern would be expected for the diurnal cycle. In fact, this can only be observed in Phase 2. In this time period the zonal differences that developed during daytime have been removed by the progressing AI. However, also the nighttime radiative cooling contributes to the increase in RH in addition to the cold air advection. When considering 6–7 July 2016 (see Fig. 19 in Appendix C), Phase 2 appears to be moister and the area south of the coast is drier but nevertheless the general evolution of RH and the three phases agree to the findings obtained for 2–3 July 2016, including the double-peak structure in Phase 2 with one peak near the coast and one peak in the hilly terrain to the north. The subsequent sections assess whether distinct differences in the ALWC and its impact on radiation can be identified between the proposed phases.

3.3 Impact of aerosol modes

Figure 20 in Appendix D shows spatiotemporal mean vertical profiles of aerosol mass concentrations over Ivory Coast. Highest contributions of about three quarters come from organic aerosol as the sum of primary organics (POA) and secondary organics (SOA). The spatiotemporal mean reveals aerosol profiles that are rather constant with height in the lowest 2000 m AGL, only

for organic aerosol an increase with height is visible.

Figure 4 shows the relative ALWC (Fig. 4a-d) and (absolute) ALWC (Fig. 4e-h) for the different aerosol modes. The relative ALWC is related to the water mass absorbed by 1 cm⁻³ of dry aerosol and the absolute ALWC to the water mass in an air volume of 1 m⁻³. As described above, the ALWC dominates in the post-frontal area and especially in Phase 2 (Fig. 4e). This

5 pattern is also visible for the relative ALWC (Fig. 4a). The main contribution comes from ACC (Fig. 4g). With respect to the relative ALWC, COARSE shows highest water uptake per unit volume (Fig. 4d) south of approximately 8° N. The peak in the relative ALWC of AIT in Phase 2 (Fig. 4b) might be related to high aerosol concentrations coming from the east. When focusing on the relative ALWC, AIT particles show a higher water uptake per unit volume than ACC particles (compare Fig. 4b and Fig. 4c). Nevertheless, due to their small size, ACC particles contribute the largest absolute ALWC (compare Fig. 4f and 10 Fig. 4g). In fact, ACC is dominating in the ALWC contribution, because a sufficient number is available and the particles are not too small. In contrast, AIT particles are lacking in size and COARSE particles are lacking in number. Accumulation mode particles over the Gulf of Guinea emerging to a large extent from long-range transport of biomass burning aerosols from 15 central Africa (e.g. Mari et al., 2008) but there are also contributions from shipping emissions. Therefore it is expected that these particles are comparably old and therefore highly hygroscopic. Over land, emissions from cities contribute to the total aerosol amount. The spatial mean diurnal cycle of the particle number concentration reveals a decrease from about 5500 on 2 July 15 UTC to 4000 on 3 July 7 UTC with the inland advection of postfrontal air coming from the Gulf of Guinea. After sunrise the particle number concentration increases again with the evolution of the convective PBL (not shown).

Same as for Fig. 3 but for (left) relative ALWC (g ALWC cm⁻³ dry aerosol) with respect to (a) total relative ALWC, (b) relative ALWC_{AIT}, (c) relative ALWC_{ACC} and (d) relative ALWC_{COARSE} and (right) absolute ALWC (μg ALWC m⁻³ air) with respect to (e) total

20 ALWC, (f) ALWC_{AIT}, (g) ALWC_{ACC} and (h) ALWC_{COARSE}. Figure 5 shows the mean GF (Fig. 5a) and the GF of the single aerosol modes (Fig. 5b-d). On average, GF of about 3–3.5 can be found in the high-ALWC areas of Phase 2 (Fig. 5a). The GF for AIT and ACC (Fig. 5a,b) are similar around 2.5, which is on the same order of magnitude compared to the findings of Chen et al. (2012) indicating GF of 1–3.25 for the North China Plain. As expected, highest aerosol growth due to ALWC is observed for COARSE with values up to 4.5 (Fig. 5d).

Same as for Fig. 3 but for the GF (d_{p,wet} d_{p,dry}⁻¹) with respect to (a) mean GF, (b) GF_{AIT}, (c) GF_{ACC} and (d) GF_{COARSE}. Sea salt particles are initially large and also highly hygroscopic but the number density is low (not shown). The spatial median of the GF is shown in Figure 6 revealing that AIT and ACC particles can be assumed comparably dry during Phase 1. During Phase 2 a doubling of the size can be observed. The comparably dry COARSE particles, already twice as big in Phase 1, double their diameter again within Phase 2. The absolute values of aerosol

30 number density as well as aerosol dry and wet diameters on 3 July 6 UTC (denoting the maximum GF in Fig. 6) are presented in Figure 21 of Appendix E, indicating a substantial aerosol increase with water uptake. However, except of the largest sea salt mode (COARSE₃ in Fig. 21), which is related to very low number concentrationsmedian number concentrations below 1.3 m⁻³, all aerosol particles are below the typical size of a cloud droplet, which is on the order of magnitude of 10 μm. Diurnal cycle of the median GF () of GF_{AIT} (red), GF_{ACC} (green) and GF_{COARSE} (blue) in the lowest 1500 m AGL over Ivory Coast (7.5° W–3° W, 4–10° N) from 2 July 15 UTC to 3 July 15 UTC. The vertical dashed lines denote the three phases introduced 35 in Figure 3. As expected, the highest GF can be found around sunrise related to the lowest temperatures and highest RH.

When focusing on ACC and COARSE particles, the slope before 6 UTC is flatter than after 6 UTC, indicating that the GF enhancement from AI-induced RH increase is slower than the heating-induced RH-decrease after sunrise. This is likely due to the combination of near-surface heating and lifting of the moist layer to greater heights. The aerosol growth, quantified in Figure 5 and 6, suggest substantial effects on the radiative transfer. This will be assessed in Section 4.

5 3.4 Impact of clouds

A further aspect that might affect the ALWC are clouds, as a special case of the RH dependency described in Section 3.2, with a focus on regimes that are saturated or virtually saturated with water vapor. It is an open question how much the ALWC in cloudy areas contribute to the total ALWC. In this section the total vertical column is considered. Figure 7 shows the total water column with respect to ALWC (Fig. 7). The respective value of the clouds is added to allow a comparison. As identified 10 in Figure 3b, largest ALWC values are reached in Phase 2. However, also Phase 3 shows remarkable contributions that are not visible when focusing on the layer below 1500 m AGL. ~~Diurnal cycle of total water column (g m^{-2}) as median over Ivory Coast (7.5°W – 3°W , 4 – 10°N) from 2 July 15 UTC to 3 July 15 UTC with respect to $\text{ALWC}_{\text{Total}}$ (black), ALWC_{AIT} (red), ALWC_{ACC} (green) and $\text{ALWC}_{\text{COARSE}}$ (blue) as well as the median total cloud water (grey, divided by 100). Values below 10^{-3} g m^{-2} are not considered. The vertical dashed lines denote the three phases introduced in Figure 3.~~ The median cloud water 15 is about 2–3 orders of magnitude larger (grey curve in Fig. 7), but due to the large standard deviation, ALWC and cloud water can differ 4 orders of magnitude (10th percentile). ALWC and cloud water correlate in the diurnal evolution (Fig. 7) with one peak in Phase 2 (NLLS) and one peak in Phase 3 (convective clouds). Interestingly, the cloud water and also the ALWC show a local minimum in the transition between Phase 2 and Phase 3 during the SCT.

Figure 8 quantifies the contribution of ALWC that comes from cloudy grid volumes. The in-cloud contribution from $\text{ALWC}_{\text{Total}}$ 20 is between 40 and 60 %, clearly dominated by ALWC_{AIT} and ALWC_{ACC} . The in-cloud contribution of $\text{ALWC}_{\text{COARSE}}$ is smaller with a constant diurnal offset of about 20 % compared to the other aerosol modes. ~~Diurnal cycle of the median contribution from in-cloud areas () with respect to $\text{ALWC}_{\text{Total}}$ (black), ALWC_{AIT} (red), ALWC_{ACC} (green), $\text{ALWC}_{\text{COARSE}}$ (blue) and the contribution of in-cloud AOD to the total AOD (brown) in the total vertical column over Ivory Coast (7.5°W – 3°W , 4 – 10°N) from 2 July 15 UTC to 3 July 15 UTC. The vertical dashed lines denote the three phases introduced in Figure 3.~~ Although 25 the strong contribution of in-cloud areas to the ALWC is not surprising, since here the highest RH can be expected, it is nevertheless remarkable. Between 3 and 9 % of the model grid boxes in the lowest 10 km are related to clouds during the day and this small fraction captures more than half of the total ALWC. To highlight the importance of this finding, the contribution of in-cloud AOD to the total AOD is added in Figure 8, which shows the same diurnal evolution as the ALWC. Approximately 40 % of the total AOD is related to cloud areas.

4 ALWC impact on radiative transfer

4.1 Definition of subdomains

After assessing the quantities affecting the ALWC (Sect. 3), this section focuses on the impact ALWC has on the radiative transfer comparing *No-ALWC* with *Reference*. *No-ALWC* denotes a sensitivity study neglecting the ALWC in the radiative transfer calculations. To evaluate the differences in net downward shortwave radiation at the surface (SSR) and net downward longwave radiation at the surface (SLR) between the two realizations, it is necessary to consider side-effects that have the potential to affect the differences apart from the consideration of the ALWC, in particular spatiotemporal differences in cloud pattern (displacement of clouds). Therefore, in the following two domain subsets are considered: (1) areas that are simultaneously cloudy in both realizations (in-cloud area, ICA) and (2) areas that are simultaneously cloud free in both realizations (off-cloud area, OCA). Areas, which differ in the cloud status, are omitted. Even if a grid box is related to clouds in both realizations, cloud properties may differ. Statistics of the difference in cloud properties are summarized in Table 4 of Appendix F including the full time period 2 July 15 UTC to 3 July 15 UTC. Table 4 includes the total cloud water, Cloud Droplet Number Concentration (CDNC) and effective radius. The spatiotemporal median over Ivory coast reveals negligible differences in cloud properties. However, for spatial analyses substantial differences can occur due to a displacement of clouds and different properties. Therefore it is not possible to fully disentangle radiative effects of ALWC from the cloud displacement in ICA. This is especially problematic since ICA is related to the highest ALWC amounts as shown in Section 3.4. In the following, we sharpen the condition for ICA by considering only the areas in which the total cloud water differences between the two realizations are below 0.1 g m^{-2} (approximately 1 % of the *Reference* median). Consider that the sharpened condition substantially decreases the selected area (on average only 7.6 % of the cloudy area can be considered) and therefore makes the results less representative for the cloudy area. OCA is expected to provide more robust results since the properties of clouds are not relevant in this area. For *Reference* on 3 July 6 UTC, Figure 22 shows the wet diameter separated in ICA and OCA for the lowest 1500 m AGL over Ivory Coast, highlighting the effect that submicron particles (Fig. 22a) need a RH near 100 % to significantly grow, whereas sea salt (Fig. 22b) already shows a growth due to ALWC at lower RH values. The median temperature for ICA (OCA) is 20.9°C (21.7°C) and the median RH for ICA (OCA) is 99.9 % (93.2 %).

4.2 Spatiotemporal differences in near-surface atmospheric properties

Figure 9 shows SSR in terms of the *Reference* absolute values (Fig. 9a) and the difference between *Reference* and *No-ALWC* (Fig. 9b) as a Hovmöller diagram. The following values in brackets indicate the median and the 99th/1th percentile of the differences considering the area south of 8°N . Since Phase 1 and 2 are related to the evening and night, the ALWC-SSR impact is restricted to Phase 3 and the early hours of Phase 1. When focusing on the area south of 8°N generally a decrease in SSR can be observed when considering ALWC in the radiation for ICA (-28 W m^{-2} , -111 W m^{-2} ; Fig. 9b) and OCA (-15 W m^{-2} , -107 W m^{-2} ; Fig. 9c). The positive values north of 8°N in Phase 3 are related to a change in cloud cover (more clouds in *Reference*), which is not a general feature. On 6-7 July the entire domain is related to a reduction in SSR (Fig. 24). ~~Hovmöller diagram of SSR (W m^{-2}) for (a) *Reference*, (b) *Reference* minus *No-ALWC* for ICA and (c) *Reference* minus *No-ALWC* for~~

OCA as zonal mean over Ivory Coast (7.5° W– 3° W, 4 – 10° N) between 2 July 15 UTC and 3 July 15 UTC. The horizontal bars denote the zonal mean location of the 302 K isentrope at 250 m AGL of *Reference*, the horizontal solid line the zonal mean coast line and the vertical dashed lines the three phases introduced in Figure 3. In Figure 10 the SLR is shown with respect to the *Reference* absolute value (Fig. 10a) and the difference between *Reference* and *No-ALWC* (Fig. 10b). For SLR the differences are less coherent than for SSR and the values are much smaller. Areas with positive and negative differences occur. For the post-frontal area, especially in the late Phase 1 and in Phase 2, negative values prevail, which indicates more outgoing longwave radiation in *No-ALWC*. Without the ALWC, less SLR can be absorbed and re-emitted in the atmosphere. During Phase 3 SLR is reduced due to the reduced shortwave input (compare Fig. 9b,c). The SLR differences are small in ICA (-0.6 W m^{-2} , -10 W m^{-2} ; Fig. 10b) and OCA (-0.5 W m^{-2} , -13 W m^{-2} ; Fig. 10c) in agreement with the findings on 6–7 July (Fig. 24). Especially the nighttime SLR differences appear insignificant. Only during daytime, with changes in SSR, the SLR shows relevant differences when considering the ALWC. *Same as for Fig. 9 but for SLR: (a) Reference, (b) Reference minus No-ALWC for ICA (c) Reference minus No-ALWC for OCA. Positive (negative) values in (b) and (c) denote more outgoing longwave radiation in Reference (No-ALWC).* The radiative impact on 2-m temperature is presented in Figure 11a. When focusing on the absolute values (Fig. 11), a diurnal cycle of about 8 K can be observed inland. Due to the fixed Sea Surface Temperature (SST) in COSMO-ART, the air temperature over the Gulf of Guinea is virtually constant. The definition of the three phases (Fig. 3) agrees well to the diurnal cycle of the temperature. In Phase 2 lowest temperatures over entire Ivory Coast can be observed. Generally, the daytime heating inland (pre-frontal in Phase 1 and 3) is stronger in *No-ALWC* than in *Reference* due to additional SSR input (Fig. 9b,c).

As expected from the small nighttime difference in SLR, also no relevant temperature differences occur during night (Fig. 11b,c). The postfrontal area (Phase 1 and 2), which is related to airmasses from the ocean with fixed SST, eliminates the differences developing during day. *Same as for Fig. 9 but for 2-m temperature (°C) and 2-m temperature difference (K): (a) Reference, (b) Reference minus No-ALWC for ICA (c) Reference minus No-ALWC for OCA.* The temperature difference during Phase 1 and 3 are negative for ICA (-0.04 K , -1.2 K ; Fig. 11b) and OCA (-0.04 K , -1.3 K ; Fig. 11c). The differences in SSR, SLR and 2-m temperature on 6–7 July, which are given in Figure 23, 24 and 25 of Appendix G, are on the same order of magnitude as on 2–3 July. Also the comparison between the results for ICA and OCA reveals no significant differences.

4.3 ALWC impact on Aerosol Optical Depth (AOD)

The observed changes in radiative transfer due to ALWC are caused by the ALWC impact on the AOD. Figure 12 presents the Empirical Cumulative Distribution function (ECDF) for the modeled AOD using the entire 25 h time period separated to ICA (blue) and OCA (red) AOD. With this the authors want to highlight that the focus is on aerosols and the AOD and not on effects of the cloud optical thickness. When neglecting ALWC in the radiation, the AOD distribution is virtually equal for ICA and OCA (dashed lines in Fig. 12) with median values around 0.2 (circles). In contrast, the AOD distribution significantly differs when considering ALWC (solid lines in Fig. 12) with median values of 0.7 (ICA, blue dot) and 0.3 (OCA, red dot). We conclude that ALWC generally increases the AOD and also causes AOD sensitivities with respect to RH (ICA and OCA).

Despite the substantial differences in AOD between the two realizations with respect to ICA, the differences in SSR, SLR and 2-m-temperature are not significantly higher than for OCA in the zonal mean as shown above. Most likely clouds are dominating the radiative transfer in ICA and therefore the AOD has less impact in these areas. ~~ECDF of the total AOD of ICA (blue) and OCA (red) for Reference (solid lines) and No-ALWC (dashed lines) over Ivory Coast (7.5° W–3° W, 4–10° N) including the time period from 2 July 15 UTC to 3 July 15 UTC. The dots (circles) highlight the median with respect to Reference (No-ALWC) and the whisker the 10th and 90th percentiles.~~ The diurnal cycle of the AOD is shown in Figure 13 for Reference and No-ALWC. Without ALWC, the AOD is rather zonally-symmetrical without a remarkable diurnal evolution (Fig. 13b) but by including ALWC, a clear diurnal cycle emerges (Fig. 13a). The dry areas, in particular the pre-frontal area in Phase 1, show AOD minima, whereas the wetter Phases 2 and 3 reveal a significant AOD increase.

10 ~~Hovmöller diagram of AOD for (a) Reference and (b) No-ALWC as zonal mean over Ivory Coast (7.5° W–3° W, 4–10° N) between 2 July 15 UTC and 3 July 15 UTC. The horizontal bars denote the zonal mean location of the 302 K isentrope at 250 m AGL, the horizontal solid line the zonal mean coast line and the vertical dashed lines the three phases introduced in Figure 3. Note the different color scales in (a) and (b).~~ Figure 14 summarizes the ALWC effects on SSR, SLR and AOD by presenting the differences between Reference and No-ALWC for the entire Ivory Coast. Strongest signals are visible for SSR

15 during Phase 1 and 3. Differences in the SLR are likely related to cloud fraction variations (note anticorrelation of SSR and cloud fraction differences). The fluctuations in SSR (red solid line) after sunrise are related to differences in the cloud cover (blue line). The ~~difference of the~~ AOD is higher in the wet Phases 2 and 3 than during the comparably dry Phase 1. ~~Diurnal cycle of the difference between Reference and No-ALWC with respect to SSR (red solid, $W\ m^{-2}$), SLR (red dashed, $W\ m^{-2}$), domain-wide cloud fraction (blue,) and AOD (brown) as median over Ivory Coast (7.5° W–3° W, 4–10° N) between 2 July 15 UTC and 3 July 15 UTC. The vertical dashed lines indicate the three phases introduced in Figure 3. Note the color coded of the different ordinates:~~

20

4.4 ALWC-radiation relationship

Sections 4.2 and 4.3 provided insight in the ALWC effects on radiation and AOD. Based on these findings the pivotal question is: Can we observe a robust relationship between ALWC and SSR as well as SLR? To answer this question we used the full

25 25 h period 2 July 15 UTC to 3 July 15 UTC and clustered it according to clouds (ICA and OCA) and time of day (daytime: 2 July 15–18 UTC and 3 July 7–15 UTC; nighttime: 2 July 19 UTC to 3 July 6 UTC). ~~Relationship between the total column ALWC ($g\ m^{-2}$) and the radiation difference between Reference and No-ALWC ($W\ m^{-2}$) capturing Ivory Coast (7.5° W–3° W, 4–8° N) and the time period 2 July 15 UTC to 3 July 15 UTC. The data is clustered in areas that are simultaneously cloudy (left, ICA) or cloud free (right, OCA) in both realizations. The top panels show the SSR difference (2 July 15–18 UTC and~~

30 ~~3 July 7–15 UTC), the middle panels the SLR daytime difference (same time period as SSR) and the bottom panels the SLR nighttime difference (2 July 19 UTC to 3 July 6 UTC). The ALWC values are clustered in bins with an increment of 0.01 $g\ m^{-2}$. For every bin the spatial median of the radiation difference is calculated (blue line). The envelope, spanned by the 25th and 75th percentile of the radiation difference, is shown as blue shading. For greater ALWC values the spread significantly increases. For this area (empirically selected) the median radiation difference is shown as blue dots instead of a blue line. A~~

linear fit is calculated for the first part of the curves (red line). The fitted equations are shown in the top-left corner of the panels. The clusters are sorted according to the total column ALWC (bin size 0.01 g m^{-2}). For all grid points, which are assigned to a certain bin, the median of the radiation differences *Reference* minus *No-ALWC* is calculated and plotted (blue lines in Fig. 15) together with the 25th and 75th percentile (blue shading). Linear fits are added to an empirically selected 5 subset of the total ALWC range, omitting the to quantify the ALWC-radiation relationship. The fitting omits bins with large ALWC (less data and large spread) and low ALWC due to the nonlinearity, to quantify the ALWC-radiation relationship. A detailed analysis revealed that not more than 0.5 % of the data are omitted. Figure 15c and Figure 15e show a nonlinear behavior for low ALWC. Therefore also these parts are omitted in the linear fitting. This affects 3.5-23.3 % of the data. The 10 slopes (W g^{-1}), which are derived from the linear fitting, are summarized in Table 2. Furthermore, we applied a bootstrapping technique for the six ALWC-radiation datasets of Table 2. For 10.000 re-samples the corresponding slopes are calculated to estimate the uncertainty of the slope (Table 2). Nevertheless, the informative value of this approach is limited to the fact that the ALWC-radiation relationship is not only defined by the ALWC itself but also by the distribution of the ALWC on aerosol particles. It can be expected that with the same total ALWC, many small particles with small ALWC values are more effective in altering the radiation than a few big particles with high ALWC values. Therefore, it might be problematic to compare 15 these results with other regions with different aerosol distributions. Radiation-ALWC relationship (W g^{-1}) based on linear fits as presented in Figure 15, including the time period 2 July 15 UTC to 3 July 15 UTC. The subdomain denotes whether the captured area is simultaneously cloudy (ICA) or cloud-free (OCA) in both realizations. *Original data* denote the slopes derived from Fig. 15 whereas *bootstrapping* refers to the median slopes of the 10.000 re-samples. The confidence intervals are derived by using the Gaussian approximation and $\alpha=0.05$ and the evaluation range provides the ALWC interval, which is used for 20 the linear fitting.

Radiation Subdomain Radiation-ALWC relationship (W g^{-1}) Evaluation range (g m^{-2})
 Original data
 Bootstrapping SSR-ICA -318 -305 ± 39 0.00 -0.49 SSR-OCA -106 -114 ± 42 0.00 -0.29 Daytime

SLR-ICA -12 -12 ± 5 0.04 -0.49 Daytime SLR-OCA -8.4 -12 ± 10 0.04 -0.39 Nighttime SLR

ICA -7.1 -7.1 ± 1.3 0.05 -0.50 Nighttime SLR-OCA -6.0 -6.5 ± 2.3 0.04 -0.49

Generally, the increase in ALWC leads to a decrease in SSR and SLR in *Reference* compared to *No-ALWC* (Fig. 15), which is more pronounced for ICA (Fig. 15, left) than for OCA (Fig. 15, right). Since ICA covers a wider ALWC interval than OCA, also the linear fit is more robust. In Section 4.1 ICA is defined as an area which is affected by clouds in both realizations and the differences in total cloud water are below 0.1 g m^{-2} to minimize effects from displaced clouds. This cloud water threshold value is generally smaller than the observed values of ALWC suggesting that effects from cloud water differences are smaller than effects from ALWC. Highest ALWC-radiation sensitivities can be observed for SSR in ICA with about -300 W g^{-1} . For 25 OCA the decrease is about -100 W g^{-1} . With respect to SLR, a separation in daytime and nighttime is done, with the former referring to the time period used for the SSR analysis. Negative SLR differences denote more outgoing longwave radiation in *No-ALWC*. This indicates that the ALWC contributes to the absorption and re-emission of SLR in the atmosphere. What we learn from the bootstrapping is that there are no statistically significant differences between the SLR decrease ICA and OCA or during daytime and nighttime (Table 2). The decrease is on an order of magnitude of -10 W g^{-1} . Interestingly, for ALWC 30 values below 0.05 g m^{-2} positive differences occur (more outgoing longwave radiation in *Reference*) and the relationship is

nonlinear (Fig. 15e-f, but also 15a,c,e). Therefore the linear fit omits this part of the curve. The reason for this behavior is not clear. This analysis is repeated for 6–7 July (Fig. 26 and Table 5, confirming the general relationship of decreasing radiation with increasing ALWC values. For SSR ICA, similar results are found whereas the other subsets tend to have stronger radiation declines with ALWC than on 2–3 July 2016. On the one hand this is related to the sensitivity of the interval selection for 5 the fitting and on the other hand 6–7 July shows higher RH (Fig. 19a) and lower temperatures (Fig. 25a) than 2–3 July and therefore a higher potential for altering the radiation.

5 Conclusions

This modeling study set the focus on the impact of Aerosol Liquid Water Content (ALWC) on the radiative transfer over Southern West Africa (SWA). It provides a complementary study to Deetz et al. (2018), which focuses on the implication of 10 aerosols on clouds and the atmospheric dynamics over SWA. The results are obtained via a process study with the regional model COSMO-ART on 2–3 and 6–7 July 2016, a time period in the well-established West African Monsoon (WAM) and little impacts of Mesoscale Convective Systems. With our study we aimed at (1) the quantification of the diurnal evolution of ALWC-related properties, (2) the evaluation of the ALWC impact on radiative transfer and (3) to derive robust relationships between ALWC and the change in radiative transfer.

15 Deetz et al. (2018) identify the Atlantic Inflow (AI) as an atmospheric phenomenon, which affects entire SWA by changes in temperature, relative humidity (RH) and wind speed with an especially coherent pattern over Ivory Coast. Therefore the spatial focus in Deetz et al. (2018) and this analysis is on this area. It turns out that AI, as an underlying meteorological process, affects all measures relevant for ALWC, in particular RH, clouds and aerosol properties. AI ~~affeeted~~ affects the monsoon layer (lowest 1900 m AGL) by advecting airmasses with comparably low temperatures and high RH onshore. Highest RH are reached in the 20 post-frontal area of AI. We have shown that AI decisively shapes the diurnal evolution of the RH and propose three phases: *Phase 1* (15–2 UTC) denotes the progression of the AI, inducing an inland contrast between the comparably dry and warm air pre-frontally and the comparably moist and cold air post-frontally. *Phase 2* (3–8 UTC) refers to the moist morning. The AI front has passed the area providing homogeneously moist and cool conditions. *Phase 3* (9–15 UTC) is the Daytime drying phase. After sunrise the land area warms and dries again leading to the re-establishment of the AI front. Due to AI the diurnal 25 cycle is not primarily thermodynamically driven (nighttime radiative cooling) but dynamically driven. Since several studies (e.g. Adler et al., 2017) have shown that AI is a common phenomenon during the West African monsoon (WAM), we suggest that the proposed phase definition can be generalized to this time period. This is supported by additional simulations for 6–7 July that show similar patterns. The spatiotemporal pattern of ALWC is clearly dominated by that of the RH. On average 60–80 % of the ALWC is related to RH regimes > 95 %. With respect to the aerosol size, the accumulation mode is the dominant 30 ALWC contributor in agreement to the findings of Bian et al. (2014). These particles are adequate in number and size and are also highly hygroscopic. Around sunrise (6 UTC, Phase 2) highest RH and therefore the ALWC maximum is reached over SWA. This is related to aerosol growth factors of about 2 for Aitken and accumulation mode and about 4 for coarse mode particles.

The radiative impact of ALWC is assessed by an additional model realization that neglects the ALWC impact on the radiative transfer. Including the ALWC leads to a significant increase in the Aerosol Optical Depth (AOD) especially for cloud areas (from about 0.2 to 0.7 on average). Therefore ALWC introduces a RH dependency in the AOD. However, effects from the AOD increase in cloudy areas on shortwave radiation and temperature are not significantly stronger than for the areas off clouds, 5 likely because the clouds are dominating the radiative transfer and the AOD has less impact. Generally, a decrease in incoming shortwave radiation can be observed when considering ALWC on an order of magnitude of -20 W m^{-2} (spatiotemporal average). Longwave effects appear insignificant. Since the effects are small during night, also 2-m temperature differences are restricted to daytime. The temperature decrease is usually not greater than -1 K but this is already significant in moist tropical climates.

10 To derive a relationship between ALWC and radiation (W per g ALWC), we calculated linear fits to the radiation decrease with increasing total column ALWC and estimated the uncertainty by using a bootstrapping technique. For shortwave radiation in-cloud (off-cloud), a relationship of $-305 \pm 39 \text{ W g}^{-1}$ ($-114 \pm 42 \text{ W g}^{-1}$) is found. For longwave radiation the relationship is about -10 W g^{-1} with insignificant differences between day and night as well as in-cloud and off-cloud. However, these relationships do not include effects arising from the aerosol optical properties (many small particles versus few large particles). The 15 findings indicate the general need to consider ALWC or the RH dependency of the AOD in the COSMO radiation calculation. This is especially of relevance in SWA with its moist and polluted monsoon layer. Although, the additional period 6–7 July is used to evaluate the robustness of the results, revealing similar evolutions of AI and the radiation differences, simulations on longer time scales are necessary to increase the reliability in the ALWC-radiation relationship. A drawback in this study is that the activated aerosol is not removed from the aerosol distribution leading to potential double counts in the radiative transfer 20 calculations. A simulation with radiatively fully transparent clouds can provide further insight in the ALWC-radiative impact by disentangling from the cloud properties but it is expected that the surplus in incoming solar radiation would significantly alter the atmospheric dynamics and therefore make it less realistic. It is expected, that the radiative effect of the ALWC is determined by a combination of the aerosol size increase and the corresponding change of the refractive index. Although it would be interesting to assess the contribution of each process, this is beyond the scope of this work and has to be left for future 25 studies.

The non-negligible radiative impact of ALWC motivates post-DACCIWA measurement efforts in which the SWA haze could be targeted. In this regard the time of sunrise will be of special interest, since at this time the ALWC maximum is reached and also the humidity related AOD increase is highest. However, strongest effects on temperature occurs later in the morning. The quantification of aerosol hygroscopicity with aircrafts on clear and hazy days might allow to derive observational-based relationships between ALWC and the radiative transfer or visibility in general. Especially nocturnal research flights can provide 30 added value complementary to DACCIWA. An interesting time of year to further study this effect is boreal spring (e.g. March) characterized by pre-monsoon conditions with high aerosol and humidity but less cloud and precipitation than in summer. There will be a **measurement** study estimating the ALWC solely based on measurements by using aircraft observations and the ZSR mixing rule (**S-Sophie** Haslett, personal communication).

Data availability. The underlying research data are available upon request from the corresponding author.

Competing interests. The authors declare that they have no conflict of interest.

Special issue statement. This article is part of the special issue *Results of the project "Dynamics–aerosol–chemistry–cloud interactions in West Africa" (DACCIWA)*

Appendix A: COSMO-ART model configuration

Appendix B: Evaluation of RH vertical profiles

Appendix C: Hovmöller diagram of RH on 6–7 July 2016

Appendix D: Spatiotemporally-averaged profiles of aerosol mass concentration on 2–3 July 2016

5 Appendix E: Aerosol dry and wet diameters on 3 July 2016, 6 UTC

Appendix F: Realization-related cloud property differences on 2–3 July 2016

Appendix G: Hovmöller diagram of SSR, SLR and 2-m temperature differences on 6–7 July 2016

Appendix H: ALWC-radiation relationship on 6–7 July 2016

Acknowledgements. The research leading to these results has received funding from the European Union 7th Framework Programme

10 (FP7/2007-2013) under Grant Agreement no. 603502 (EU project DAccIWA: Dynamics-aerosol-chemistry-cloud interactions in West Africa). Thanks to the German Weather Service (DWD) for providing access to the ICON forecast data and to the Steinbuch Centre for Computing (SCC) for providing the computational resources for the model realizations. The data analysis was done by using the software R (2013) .

References

Adler, B., Kalthoff, N., and Gantner, L.: Nocturnal low-level clouds over southern West Africa analysed using high-resolution simulations, *Atmos. Chem. Phys.*, 17, 899–910, 2017.

Aklilu, Y., Mozurkewich, M., Prenni, A. J., Kreidenweis, S. M., Alfarra, M. R., Allan, J. D., Anlauf, K., Brooks, J., Leaitch, W. R., Sharma, S., Boudries, H., and Worsnop, D. R.: Hygroscopicity of particles at two rural, urban influenced sites during Pacific 2001: Comparison with estimates of water uptake from particle composition, *Atmos. Environ.*, 40, 2650–2661, 2006.

Alfarra, M. R., Coe, H., Allan, J. D., Bower, K. N., Boudries, H., Canagaratna, M. R., Jimenez, J. L., Jayne, J. T., Garforth, A. A., Li, S.-M., and Worsnop, D. R.: Characterization of urban and rural organic particulate in the Lower Fraser Valley using two Aerodyne Aerosol Mass Spectrometers, *Atmos. Environ.*, 38, 5745–5758, 2004.

10 Andersen, H. and Cermak, J.: How thermodynamic environments control stratocumulus microphysics and interactions with aerosols, *Environ. Res. Lett.*, 10, 2015.

Athanasiopoulou, E., Vogel, H., Vogel, B., Tsimpidi, A. P., Pandis, S. N., Knote, C., and Fountoukis, C.: Modeling the meteorological and chemical effects of secondary organic aerosols during an EUCAARI campaign, *Atmos. Chem. Phys.*, 13, 625–645, 2013.

15 Baldauf, M., Seifert, A., Förstner, J., Majewski, D., and Raschendorfer, M.: Operational Convective-Scale Numerical Weather Prediction with the COSMO model: Description and Sensitivities, *Mon. Wea. Rev.*, pp. 3887–3905, 2011.

Bangert, M.: Interaction of Aerosol, Clouds, and Radiation on the Regional Scale, Institut für Meteorologie und Klimaforschung, Karlsruher Institut für Technologie, Dissertation, 2012.

Beyersdorf, A. J., Ziembra, L. D., Chen, G., Corr, C., Crawford, J. H., Diskin, G. S., Moore, R. H., Thornhill, K. L., Winstead, E. L., and Anderson, B. E.: The impacts of aerosol loading, composition, and water uptake on aerosol extinction variability in the Baltimore–Washington, D.C. region, *Atmos. Chem. Phys.*, 16, 1003–1015, 2016.

20 Bian, Y. X., Zhao, C. S., Ma, N., Chen, J., and Xu, W. Y.: A study of aerosol liquid water content based on hygroscopicity measurements at high relative humidity in the Northern China Plain, *Atmos. Chem. Phys.*, 14, 6417–6426, 2014.

Brock, C. A., Wagner, N. L., Anderson, B. E., Beyersdorf, A., Campuzano-Jost, P., Day, D. A., Diskin, G. S., Gordon, T. D., Jimenez, J. L., Lack, D. A., Liao, J., Markovic, M. Z., Middlebrook, A. M., Perring, A. E., Richardson, M. S., Schwarz, J. P., Welti, A., Ziembra, L. D., 25 and Murphy, D. M.: Aerosol optical properties in the southeastern United States in summer – Part 2: Sensitivity of aerosol optical depth to relative humidity and aerosol parameters, *Atmos. Chem. Phys.*, 16, 5009–5019, 2016.

CAMS: Copernicus Atmosphere Monitoring Service (<http://apps.ecmwf.int/datasets/data/cams-gfas/>, last access: 30 July 2017), 2017.

CCSM: https://svn-ccsm-inputdata.cgd.ucar.edu/trunk/inputdata/lnd/clm2/raw_data/pftlanduse.3minx3_min.simyr2000.c110913/ (last access: 10 June 2017), 2015.

30 Chen, J., Zhao, C. S., Ma, N., Liu, P. F., Göbel, T., Hallbauer, E., Deng, Z. Z., Ran, L., Xu, W. Y., Liang, Z., Liu, H. J., Yan, P., Zhou, X. J., and Wiedensohler, A.: A parameterization of low visibilities for hazy days in the North China Plain, *Atmos. Chem. Phys.*, 12, 4935–4950, 2012.

Cheng, Y. F., Wiedensohler, A., Eichler, H., Heintzenberger, J., Tesche, M., Ansmann, A., Wendisch, M., Su, H., Althausen, D., Herrmann, H., Gnauk, T., Brüggemann, E., Hu, M., and Zhang, Y. H.: Relative humidity dependence of aerosol optical properties and direct radiative 35 forcing in the surface boundary layer at Xinken in Pearl River Delta of China: An observation based numerical study, *Atmos. Environ.*, 42, 6373–6397, 2008.

5 Crumeyrolle, S., Gomes, L., Tulet, P., Matsuki, A., Schwarzenboeck, A., and Crahan, K.: Increase of the aerosol hygroscopicity by cloud processing in a mesoscale convective system: a case study from the AMMA campaign, *Atmos. Chem. Phys.*, 8, 6907–6924, 2008.

Deetz, K.: Assessing the Aerosol Impact on Southern West African Clouds and Atmospheric Dynamics, *Wissenschaftliche Berichte des Instituts für Meteorologie und Klimaforschung des Karlsruher Instituts für Technologie*, KIT Scientific Publishing, Karlsruhe, Dissertation, 75, 99–144, 2018.

10 Deetz, K. and Vogel, B.: Development of a new gas-flaring emission dataset for southern West Africa, *Geosci. Model Dev.*, 10, 1607–1620, 2017.

Deetz, K., Vogel, H., Knippertz, P., Adler, B., Taylor, J., Coe, H., Bower, K., Haslett, S., Flynn, M., Dorsey, J., Crawford, I., Kottmeier, C., and Vogel, B.: Numerical simulations of aerosol radiative effects and their impact on clouds and atmospheric dynamics over southern 15 West Africa, *Atmos. Chem. Phys.*, 18, 9767–9788, 2018.

EDGAR: Emission Database for Global Atmospheric Research, http://edgar.jrc.ec.europa.eu/htap_v2/index.php?SECURE=123 (last access: 10 June 2017), 2010.

Fountoukis, C. and Nenes, A.: Continued development of a cloud droplet formation parameterization for global climate models, *J. Geophys. Res.*, 110, 2005.

15 Fountoukis, C. and Nenes, A.: ISORROPIA II: a computationally efficient thermodynamic equilibrium model for K^+ - Ca^{2+} - Mg^{2+} - NH_4^+ - SO_4^{2-} - NO_3^- - Cl^- - H_2O aerosol, *Atmos. Chem. Phys.*, 7, 4639–4659, 2007.

GlobCover: GlobCover Land Cover Map - European Space Agency GlobCover Project (<http://www.gelis.com/globcover-2009.htm>, last access: 10 June 2017), 2009.

Grams, C. M., Jones, S. C., Marsham, J. H., Parker, D. J., Haywood, J. M., and Heuveline, V.: The Atlantic Inflow to the Saharan heat low: 20 Observations and Modelling, *Quart. J. Roy. Meteor. Soc.*, 136, 125–140, 2010.

Hennig, T., Massling, A., Brechtel, F. J., and Wiedensohler, A.: A Tandem DMA for highly temperature-stabilized hygroscopic particle growth measurements between 90% and 98% relative humidity, *Aerosol Science*, pp. 1210–1223, 2005.

Hill, P. G., Allan, R. P., and Chiu, J. C.: Quantifying the contribution of different cloud types to the radiation budget, *Atmos. Chem. Phys.*, under review, 2017.

25 Hsu, N. C., Lee, J., Sayer, A. M., Carletta, N., Chen, S.-H., Tucker, C. J., Holben, B. N., and Tsay, S.-C.: Retrieving near-global aerosol loading over land and ocean from AVHRR, *J. Geophys. Res.*, 122, 9968–9989, 2017.

HWSD: HWSD (FAO/IIASA/ISRIC/ISSCAS/JRC), 2012: Harmonized World Soil Database (version 1.2), FAO, Rome, Italy and IIASA, Laxenburg, Austria, 2012.

Jung, J., Lee, H., Kim, Y. J., Liu, X., Zhang, Y., Gu, J., and Fan, S.: Aerosol chemistry and the effect of aerosol water content on visibility 30 impairment and radiative forcing in Guangzhou during the 2006 Pearl River Delta campaign, *Journal of Environmental Management*, 90, 3231–3244, 2009.

Kalthoff, N., Louhou, F., Brooks, B., Jegede, O., Adler, B., Babić, K., Dione, C., Ajao, A., Amekudzi, L. K., Aryee, J. N. A., Ayoola, M., Bessardon, G., Danuor, S. K., Handwerker, J., Kohler, M., Lothon, M., Pedruzo-Bagazgoitia, X., Smith, V., Sunmonu, L., Wieser, A., Fink, A. H., and Knippertz, P.: An overview of the diurnal cycle of the atmospheric boundary layer during the West African monsoon 35 season: results from the 2016 observational campaign, *Atmos. Chem. Phys.*, 18, 2913–2928, 2018.

Knippertz, P., Fink, A. H., Deroubaix, A., Morris, E., Tocquer, F., Evans, M. J., Flamant, C., Gaetani, M., Lavaysse, C., Mari, C., Marsham, J. H., Meynadier, R., Affo-Dogo, A., Bahaga, T., Brosse, F., Deetz, K., Guebsi, R., Latifou, I., Maranan, M., Rosenberg, P. D., and Schlüter,

A.: A meteorological and chemical overview of the DACCIA field campaign in West Africa in June-July 2016, *Atmos. Chem. Phys.*, pp. 10 893–10 918, 2017.

Kuang, Y., Zhao, C. S., Tao, J. C., and Ma, N.: Diurnal variations of aerosol optical properties in the North China Plain and their influences on the estimates of direct aerosol radiative effect, *Atmos. Chem. Phys.*, 15, 5761–5772, 2015.

5 Lana, A., Bell, T. G., Simó, R., Vallina, S. M., Ballabrera-Poy, J., Kettle, A. J., Dachs, J., Bopp, L., Saltzman, E. S., Stefels., J., Johnson, J. E., and Liss, P. S.: An updated climatology of surface dimethylsulfide concentrations and emission fluxes in the global ocean, *Global Biogeochem. Cycles*, 25, G1004, 2011.

Liu, P. F., Zhao, C. S., Göbel, T., Hallbauer, E., Nowak, A., Ran, L., Xu, W. Y., Deng, Z. Z., Ma, N., Mildenberger, K., Henning, S., Stratmann, F., and Wiedensohler, A.: Hygroscopic properties of aerosol particles at high relative humidity and their diurnal variations in the North 10 China Plain, *Atmos. Chem. Phys.*, 11, 3479–3494, 2011.

Lundgren, K.: Direct Radiative Effects of Sea Salt on the Regional Scale, Institut für Meteorologie und Klimaforschung, Karlsruher Institut für Technologie, Dissertation, 2010.

Lundgren, K., Vogel, B., Vogel, H., and Kottmeier, C.: Direct radiative effects of sea salt for the Mediterranean region under conditions of low to moderate wind speeds, *J. Geophys. Res.*, 118, 1906–1923, 2013.

15 Ma, N., Zhao, C. S., Nowak, A., Müller, T., Pfeifer, S., Cheng, Y. F., Deng, Z. Z., Liu, P. F., Xu, W. Y., Ran, L., Yan, P., Göbel, T., Hallbauer, E., Mildenberger, K., Henning, S., Yu, J., Chen, L. L., Zhou, X. J., Stratmann, F., and Wiedensohler, A.: Aerosol optical properties in the North China Plain during HaChi campaign: an in-situ optical closure study, *Atmos. Chem. Phys.*, 11, 5959–5973, 2011.

Maranan, M. and Fink, A.: Radiosonde - All sites'. SEDOO OMP. doi: 10.6096/baobab-dacciwa.1656, 2016.

Mari, C. H., Cailley, G., Corre, L., Saunois, M., Attié, J. L., Thouret, V., and Stohl, A.: Tracing biomass burning plumes from the Southern 20 Hemisphere during the AMMA 2006 wet season experiment, *Atmos. Chem. Phys.*, 8, 3951–3961, 2008.

Matsuki, A., Quennehen, B., Schwarzenboeck, A., Crumeyrolle, S., Venzac, H., Laj, P., and Gomes, L.: Temporal and vertical variations of aerosol physical and chemical properties over West Africa: AMMA aircraft campaign in summer 2006, *Atmos. Chem. Phys.*, 10, 8437–8451, 2010.

Maßling, A., Wiedensohler, A., Busch, B., Neusüß, C., Quinn, P., Bates, T., and Covert, D.: Hygroscopic properties of different aerosol types 25 over the Atlantic and Indian Oceans, *Atmos. Chem. Phys.*, 3, 1377–1397, 2003.

MOZART: MOZART-4/GEOS-5 forecasts, National Center for Atmospheric Research (NCAR), University Corporation for Atmospheric Research, Atmospheric Chemistry Observations & Modeling (https://www.acom.ucar.edu/acresp/AMADEUS/mz4_output/chemfcst/, last access: 30 July 2017), 2017.

Philipps, V. T. J., DeMott, P. J., and Andronache, C.: An Empirical Parameterization of Heterogeneous Ice Nucleation for Multiple Chemical 30 Chemical Species of Aerosol, *J. Atmos. Sci.*, 65, 2757–2783, 2008.

R: R Core Team, R: A Language and Environment for Statistical Computing, R Foundation for Statistical Computing, Vienna, Austria, (<http://www.R-project.org/>, last access: 9 August 2017), 2013.

Redelsperger, J.-L., Thorncroft, C. D., Diedhiou, A., Lebel, T., Parker, D. J., and Polcher, J.: African Monsoon Multidisciplinary Analysis - An International Research Project and Field Campaign, *Bull. Amer. Meteor. Soc.*, pp. 1739–1746, 2006.

35 Rieger, D., Steiner, A., Bachmann, V., Gasch, P., Förstner, J., Deetz, K., Vogel, B., and Vogel, H.: Impact of a Saharan dust outbreak on the photovoltaic power generation in Germany, *Atmos. Chem. Phys.*, 17, 13 391–13 415, 2017.

Riemer, N.: Numerische Simulationen zur Wirkung des Aerosols auf die troposphärische Chemie und die Sichtweite, *Wissenschaftliche Berichte des Instituts für Meteorologie und Klimaforschung der Universität Karlsruhe*, Dissertation, 2002.

Riemer, N., Vogel, H., Vogel, B., and Fiedler, F.: Modeling aerosols of the mesoscale-y: Treatment of soot aerosols and its radiative effects, *J. Geophys. Res.*, 108, 2003.

Ritter, B. and Geleyn, J.-F.: A Comprehensive Radiation Scheme for Numerical Weather Prediction Models with Potential Application in Climate Simulations, *Mon. Wea. Rev.*, 129, 303–325, 1992.

5 Schrage, J. M. and Fink, A. H.: Nocturnal Continental Low-Level Stratus over Tropical West Africa: Observations and Possible Mechanisms Controlling Its Onset, *Mon. Wea. Rev.*, 140, 1794–1809, 2012.

Schuster, R., Fink, A. H., and Knippertz, P.: Formation and Maintenance of Nocturnal Low-Level Stratus over the Southern West African Monsoon Region during AMMA 2006, *J. Atmos. Sci.*, 70, 2337–2355, 2013.

Seifert, A. and Beheng, K. D.: A two-moment cloud microphysics parameterization for mixed-phase clouds. Part 1: Model description, *Meteor. Atmos. Phys.*, 92, 45–66, 2006.

10 Seinfeld, J. H. and Pandis, S. N.: *Atmospheric Chemistry and Physics, From Air Pollution to Climate Change*, John Wiley & Sons, Inc., Hoboken, New Jersey, 2, 449–450, 2006.

Stokes, R. H. and Robinson, R. A.: Interactions in aqueous nonelectrolyte solutions. I. Solute-solvent equilibria, *J. Phys. Chem.*, 70, 2126–2130, 1966.

15 Tegen, I., Hollrig, P., Chin, M., Fung, I., Jacob, D., and J., P.: Contribution of different aerosol species to the global aerosol extinction optical thickness: Estimates from model results, *J. Geophys. Res.*, 102, 23 895–23 915, 1997.

van der Linden, R., Fink, A. H., and Redl, R.: Satellite-based climatology of low-level continental clouds in southern West Africa during the summer monsoon season, *J. Geophys. Res.*, 120, 1186–1201, 2015.

Vogel, B., Vogel, H., Bangert, M., Lundgren, K., Rinke, R., and Stanelle, T.: The comprehensive model system COSMO-ART - Radiative 20 impact of aerosol on the state of the atmosphere on the regional scale, *Atmos. Chem. Phys.*, 9, 8661–8680, 2009.

Walter, C., Freitas, S. R., Kottmeier, C., Kraut, I., Rieger, D., Vogel, H., and Vogel, B.: The importance of plume rise on the concentrations and atmospheric impacts of biomass burning aerosol, *Atmos. Chem. Phys.*, 16, 9201–9219, 2016.

Weimer, M., Schröter, J., Eckstein, J., Deetz, K., Neumaier, M., Fischbeck, G., Hu, L., Millet, D. B., Rieger, D., Vogel, H., Vogel, B., 25 Redmann, T., Kirner, O., Ruhnke, R., and Braesicke, P.: An emission module for ICON-ART 2.0: implementation and simulations of acetone, *Geosci. Model Dev.*, 10, 2471–2494, 2017.

Zieger, P., Väisänen, O., Corbin, J. C., Partridge, D. G., Bastelberger, S., Mousavi-Fard, M., Rosati, B., Gysel, M., Krieger, U. K., Leck, C., Nenes, A., Riipinen, I., Virtanen, A., and Salter, M. E.: Revising the hygroscopicity of inorganic sea salt particles, *Nature communications*, 8, 2017.

Evaluation of RH vertical profiles

30 ~~RH vertical profiles at Lamto (Ivory Coast) with respect to radiosoundings (black solid) and COSMO-ART (black dashed) on (a) 6 July 12 UTC, (b) 6 July 18 UTC, (c) 7 July 6 UTC, (d) 7 July 9 UTC, (e) 7 July 12 UTC and (f) 7 July 18 UTC. For the GRAW radiosondes an uncertainty of ± 4 are assumed (grey shading). The Lamto soundings are related to problems with reaching the 100 RH (Andreas Fink, personal communication, 2018).~~

RH vertical profiles at Abidjan (Ivory Coast) with respect to radiosoundings (black solid) and COSMO-ART (black dashed) on (a) 2 July 4 UTC, (b) 2 July 10 UTC, (c) 2 July 16 UTC, (d) 2 July 23 UTC, (e) 3 July 4 UTC and (f) 3 July 10 UTC, (g) 3 July 16 UTC and (h) 3 July 23 UTC. For the Meteomodem radiosondes an uncertainty of ± 4 are assumed (grey shading).

Same as for Figure 17 but for (a) 6 July 4 UTC, (b) 6 July 10 UTC, (c) 6 July 16 UTC, (d) 6 July 23 UTC, (e) 7 July 4 UTC, 5 (f) 7 July 10 UTC, (g) 7 July 16 UTC and (h) 7 July 23 UTC.

Hovmöller diagram of RH on 6–7 July 2016

Hovmöller diagram of the median (a) RH (%) and (b) total ALWC ($\mu\text{g m}^{-3}$) in the lowest 1500 m AGL as zonal mean over Ivory Coast (7.5°W – 3°W , 4 – 10°N) between 6 July 15 UTC and 7 July 15 UTC. The horizontal bars denote the zonal mean location of the 302 K isentrope at 250 m AGL, the horizontal solid line indicates the zonal mean coast line and the vertical dashed lines separate the three phases: *AI progression phase* (Phase 1), *Moist morning phase* (Phase 2) and *Daytime drying phase* (Phase 3). 10

Spatiotemporally-averaged profiles of aerosol mass concentration on 2–3 July 2016

Vertical profiles (m AGL) of aerosol concentrations ($\mu\text{g m}^{-3}$) for the median over Ivory Coast (7.5°W – 3°W , 4 – 10°N) with respect to the time period 2 July 15 UTC and 3 July 15 UTC. The colors refer to organics (POA+SOA; green solid line), 15 NO_3 (orange solid line), NH_4 (blue solid line), SO_4 (red solid line) and sea salt (grey solid line). Additionally, POA and SOA are shown as dashed and dotted green lines, respectively. The shadings denote minima and maxima in the diurnal cycle mean profile and the pie charts on right hand side highlight the mean contribution of the single species to the total aerosol composition at 500, 1000, 1500 and 2000 m AGL.

Aerosol dry and wet diameters on 3 July 2016, 6 UTC

20 Boxplots of dry (red) and wet (blue) aerosol diameters (μm) for (a) AIT and ACC and (b) COARSE, splitted in the three COSMO-ART sea salt modes as median in the lowest 1500 m AGL over Ivory Coast (7.5°W – 3°W , 4 – 10°N) on 3 July, 6 UTC. The whiskers span the data from the 2.5th to the 97.5th percentile (95 of the data). Data outside of this range is not shown. Note the logarithmic scale in (b).

Realization-related cloud property differences on 2–3 July 2016

25 **Hovmöller diagram of SSR, SLR and 2-m temperature differences on 6–7 July 2016**

Hovmöller diagram of SSR (W m^{-2}) for (a) *Reference*, (b) *Reference* minus *No ALWC* for ICA (c) *Reference* minus *No ALWC* for OCA as zonal mean over Ivory Coast (7.5°W – 3°W , 4 – 10°N) between 6 July 15 UTC and 7 July 15 UTC. The horizontal

bars denote the zonal mean location of the 302 K isentrope at 250 m AGL of *Reference*, the horizontal solid line the zonal mean coast line and the vertical dashed lines the three phases introduced in Figure 3. Same as for Fig. 23 but for the SLR. Positive (negative) values in (b) and (c) denote more outgoing longwave radiation in the *Reference* (*No-ALWC*) case. Same as for Fig. 23 but for 2-m temperature ($^{\circ}$ C) and 2-m temperature difference (K).

5 ALWC-radiation relationship on 6–7 July 2016

Relationship between the total column ALWC (g m^{-2}) and the radiation difference between *Reference* and *No-ALWC* (W m^{-2}) over Ivory Coast (7.5° W– 3° W, 4 – 8° N) during the time period 2 July 15 UTC to 3 July 15 UTC. The data is clustered in areas that are simultaneously cloudy (left, ICA) or cloud free (right, OCA) in both realizations. The top panels show the SSR difference (6 July 15–18 UTC and 7 July 7–15 UTC), the middle panels the SLR daytime difference (same time period as SSR) and the bottom panels the SLR nighttime difference (2 July 19 UTC to 3 July 6 UTC). The ALWC values are clustered in bins with an increment of 0.01 g m^{-2} . For every bin the spatial median of the radiation difference is calculated (blue line). The envelope, spanned by the 25th and 75th percentile of the radiation difference, is shown as blue shading. For greater ALWC values the spread significantly increases. For this area (empirically selected) the median radiation difference is shown as blue dots instead of a blue line. A linear fit is calculated for the first part of the curves (red line). The fitted equations are shown in 10 the top-left corner of the panels.

15

Table 1. List of acronyms used in this study.

Acronym	Description
ACC	Accumulation mode
ADE	Aerosol Direct Effect
AGL	Above Ground Layer
AI	Atlantic Inflow
AIE	Aerosol Indirect Effect
AIT	Aitken mode
ALWC	Aerosol Liquid Water Content
AOD	Aerosol Optical Depth
ASL	Above Sea Level
CDNC	Cloud Droplet Number Concentration
COARSE	Coarse mode
COSMO-ART	Consortium for Small-scale Modeling - Aerosol and Reactive Trace gases
DACCIWA	Dynamics-aerosol-chemistry-cloud interactions in West Africa
DWD	Deutscher Wetterdienst (German Weather Service)
ECDF	Empirical Cumulative Distribution Function
GF	Growth Factor
GRAALS	General Radiative Algorithm Adapted to Linear-type Solutions radiation scheme
HaChi	Haze in China campaign
ICA	In-Cloud Area
ICON	Icosahedral Nonhydrostatic Model
NLLS	Nocturnal Low-Level Stratus
No-ALWC	Model realization neglecting ALWC in the radiation calculation
OCA	Off-Cloud Area
PBL	Planetary Boundary Layer
POA	Primary Organic Aerosol
Reference	Reference case model realization with considering ALWC in the radiation calculation
RH	Relative Humidity
SCT	Stratus-to-cumulus transition
SLR	Surface Longwave (net) Radiation
SOA	Secondary Organic Aerosol
SSR	Surface Shortwave (net) Radiation
SST	Sea Surface Temperature
SWA	Southern West Africa
WAM	West African Monsoon

Table 2. Radiation-ALWC relationship (W g^{-1}) based on linear fits as presented in Figure 15, including the time period 2 July 15 UTC to 3 July 15 UTC. The subdomain denotes whether the captured area is simultaneously cloudy (ICA) or cloud-free (OCA) in both realizations. *Original data* denote the slopes derived from Fig. 15 whereas *bootstrapping* refers to the median slopes of the 10,000 re-samples. The confidence intervals are derived by using the Gaussian approximation and $\alpha=0.05$ and the evaluation range provides the ALWC interval, which is used for the linear fitting.

Radiation	Subdomain	Radiation-ALWC relationship (W g^{-1})		Evaluation range (g m^{-2})
		<i>Original data</i>	<i>Bootstrapping</i>	
SSR	ICA	-318	-305 ± 39	0.00–0.49
SSR	OCA	-106	-114 ± 42	0.00–0.29
Daytime SLR	ICA	-12	-12 ± 5	0.04–0.49
Daytime SLR	OCA	-13	-16 ± 9	0.00–0.39
Nighttime SLR	ICA	-7.1	-7.1 ± 1.3	0.05–0.50
Nighttime SLR	OCA	-8.3	-8.8 ± 2.0	0.00–0.49

Table 3. COSMO-ART model configuration used for this study.

Characteristics	Description
Model version	COSMO5.1-ART3.1
Time period	2–3 July 2016, 6–7 July 2016
Simulation domain	9.0° W–4.4° E, 3.0° N–10.8° N
Grid mesh size	2.5 km (0.0223°)
Vertical levels	80 up to 30 km (28 in the lowest 1.5 km ASL AGL)
Meteorological boundary and initial data	COSMO-ART (5 km grid mesh size using ICON operational forecasts from DWD)
Pollutant boundary and initial data	COSMO-ART (5 km grid mesh size using MOZART, 2017) GlobCover (2009) landuse data CCSM (2015) plant functional types
Cloud microphysics	Two-moment microphysics scheme (Seifert and Beheng, 2006)
Pollutant emissions	Mineral dust (online): Rieger et al. (2017) using HWSD (2012) Sea salt (online): Lundgren et al. (2013) DMS (online): using Lana et al. (2011) BVOCs (online): Weimer et al. (2017) Biomass burning (prescribed/online): Walter et al. (2016) using GFAS (CAMS, 2017) Anthropogenic (prescribed): EDGAR (2010) Gas flaring (prescribed): Deetz and Vogel (2017)
Aerosol dynamics	MADEsoot (Riemer et al., 2003; Vogel et al., 2009) Secondary inorganic aerosol: ISORROPIA II (Fountoukis and Nenes, 2007) Secondary organic aerosol: VBS (Athanasopoulou et al., 2013)
Chemical mechanisms	Gas phase chemistry: RADMK (Vogel et al., 2009)
ALWC	Anthropogenic aerosol: ISORROPIA II (Fountoukis and Nenes, 2007; Stokes and Robinson, 1966) Sea salt: Lundgren et al. (2013) Fresh soot: Riemer (2002)
Aerosol direct effect (ADE)	Vogel et al. (2009)
Aerosol indirect effect (AIE)	Warm phase: Bangert (2012) and Fountoukis and Nenes (2005) Cold phase: Philipp et al. (2008)

Table 4. Statistics of the cloud property differences (*Reference* minus *No-ALWC*, ICA) over Ivory Coast (7.5° W– 3° W, 4 – 10° N) with respect to the time period 2 July 15 UTC to 3 July 15 UTC, including the median difference, the 25^{th} and 75^{th} percentile of the differences and the ratio of 75^{th} percentile to the *Reference* average. The CDNC and the effective radius refer to the median in the lowest 1500 m AGL.

Measure	Median	25^{th} percentile	75^{th} percentile	75^{th} percentile / <i>Reference</i> average
Total cloud water (g m^{-2})	$-2.7 \cdot 10^{-4}$	-27.9	22.6	0.37
CDNC (cm^{-3})	$-2.9 \cdot 10^{-9}$	-59.1	54.7	0.79
Effective radius (μm)	$1.8 \cdot 10^{-4}$	-2.1	2.2	0.23

Table 5. Radiation-ALWC relationship (W g^{-1}) based on the linear fits of Figure 15 including the time period 6 July 15 UTC to 7 July 15 UTC. The subdomain denotes whether the captured area is simultaneously cloudy (ICA) or cloud-free (OCA) in both realizations. *Original data* denote the slopes derived from Fig. 15 whereas *bootstrapping* refers to the median slopes of the 10.000 re-samples. The confidence intervals are derived by using the Gaussian approximation and $\alpha=0.05$ and the evaluation range provides the ALWC interval, which is used for the linear fitting.

Radiation	Subdomain	Radiation-ALWC relationship (W g^{-1})		Evaluation range (g m^{-2})
		Original data	Bootstrapping	
SSR	ICA	-319	-350 ± 32	0.01–0.50
SSR	OCA	-320	-351 ± 35 <small>36</small>	0.01–0.30
Daytime SLR	ICA	-20	-28 ± 9	0.05–0.50
Daytime SLR	OCA	-32	-44 <small>42</small> ± 14 <small>11</small>	0.05 <small>0.00</small> –0.35
Nighttime SLR	ICA	-14	-20 ± 5	0.05–0.45
Nighttime SLR	OCA	-23	-25 ± 3 <small>2</small>	0.05 <small>0.00</small> –0.35

The research leading to these results has received funding from the European Union 7th Framework Programme (FP7/2007–2013) under Grant Agreement no. 603502 (EU project DAccIWA: Dynamics-aerosol-chemistry-cloud interactions in West Africa). Thanks to the German Weather Service (DWD) for providing access to the ICON forecast data and to the Steinbuech Centre for Computing (SCC) for providing the computational resources for the model realizations. The data analysis was done by using 5 the software R (2013).

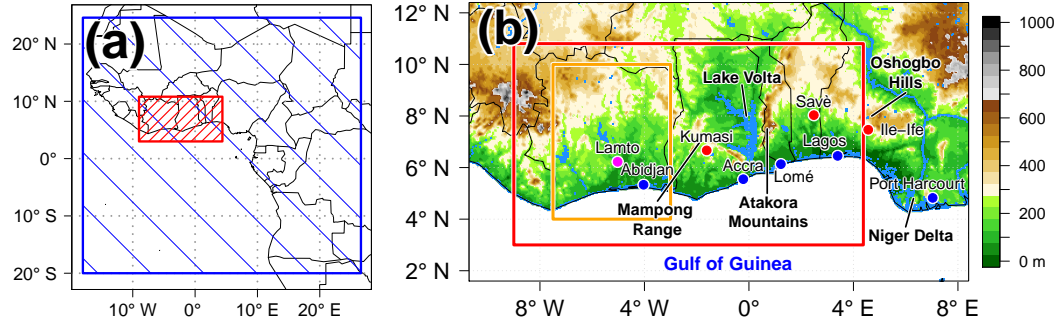


Figure 1. (a) Modeling domain SWA (red rectangle, 2.5 km grid mesh size) together with its coarse domain (blue, 5 km grid mesh size). (b) Map of the research area SWA. The color shading denotes topography (m Above Sea Level, ASL). Topographic features are named in bold. Coastal cities are shown as blue dots and the three DACCWA supersites as red dots. Lamto (magenta dot), together with Abidjan, are used for evaluations of relative humidity profiles. The modeling domain SWA is again denoted as red rectangle. The orange rectangle highlights the domain over Ivory Coast, which is used for subsequent analyses. Figure adopted from Deetz et al. (2018).

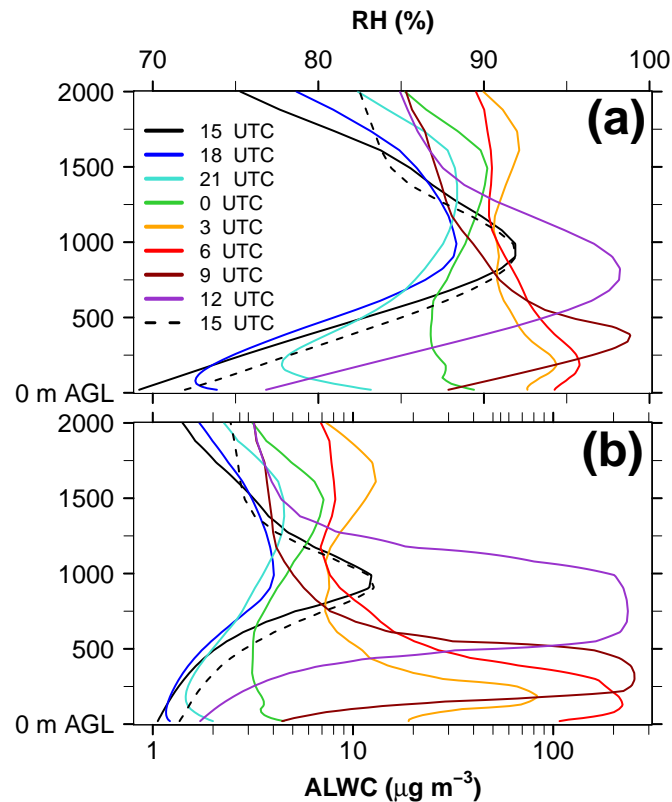


Figure 2. Vertical profiles (m AGL) of (a) RH (%) and (b) ALWC ($\mu\text{g m}^{-3}$) for the median over Ivory Coast (7.5° W – 3° W , 4 – 10° N) between 2 July 15 UTC (black solid) and 3 July 15 UTC (black dashed). Consider the logarithmic abscissa of (b).

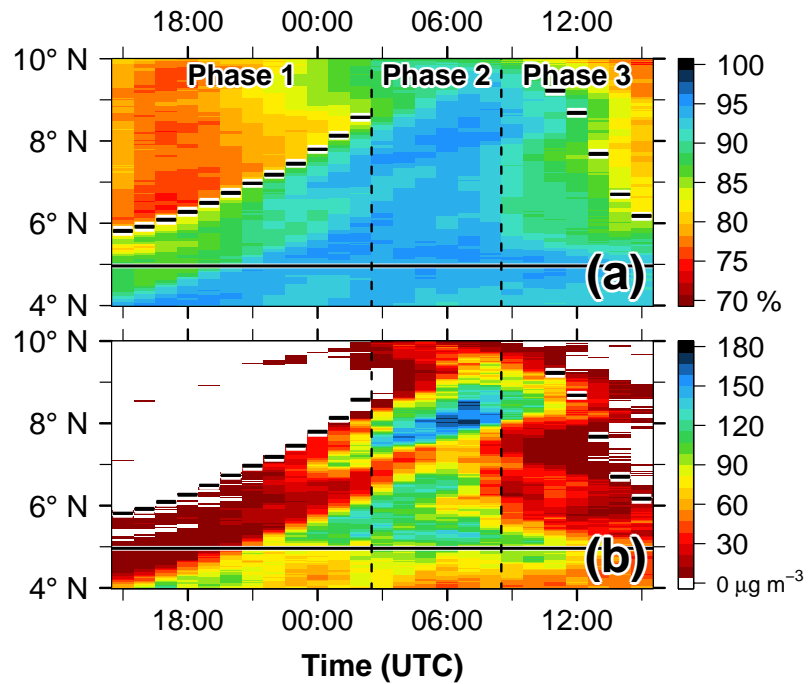


Figure 3. Hovmöller diagram of the median (a) RH (%) and (b) total ALWC ($\mu\text{g m}^{-3}$) in the lowest 1500 m AGL as zonal mean over Ivory Coast (7.5° W– 3° W, 4 – 10° N) between 2 July 15 UTC and 3 July 15 UTC. The horizontal bars denote the zonal mean location of the 302 K isentrope at 250 m AGL, the horizontal solid line the zonal mean coast line and the vertical dashed lines separate the three phases: *AI progression phase* (Phase 1), *Moist morning phase* (Phase 2) and *Daytime drying phase* (Phase 3).

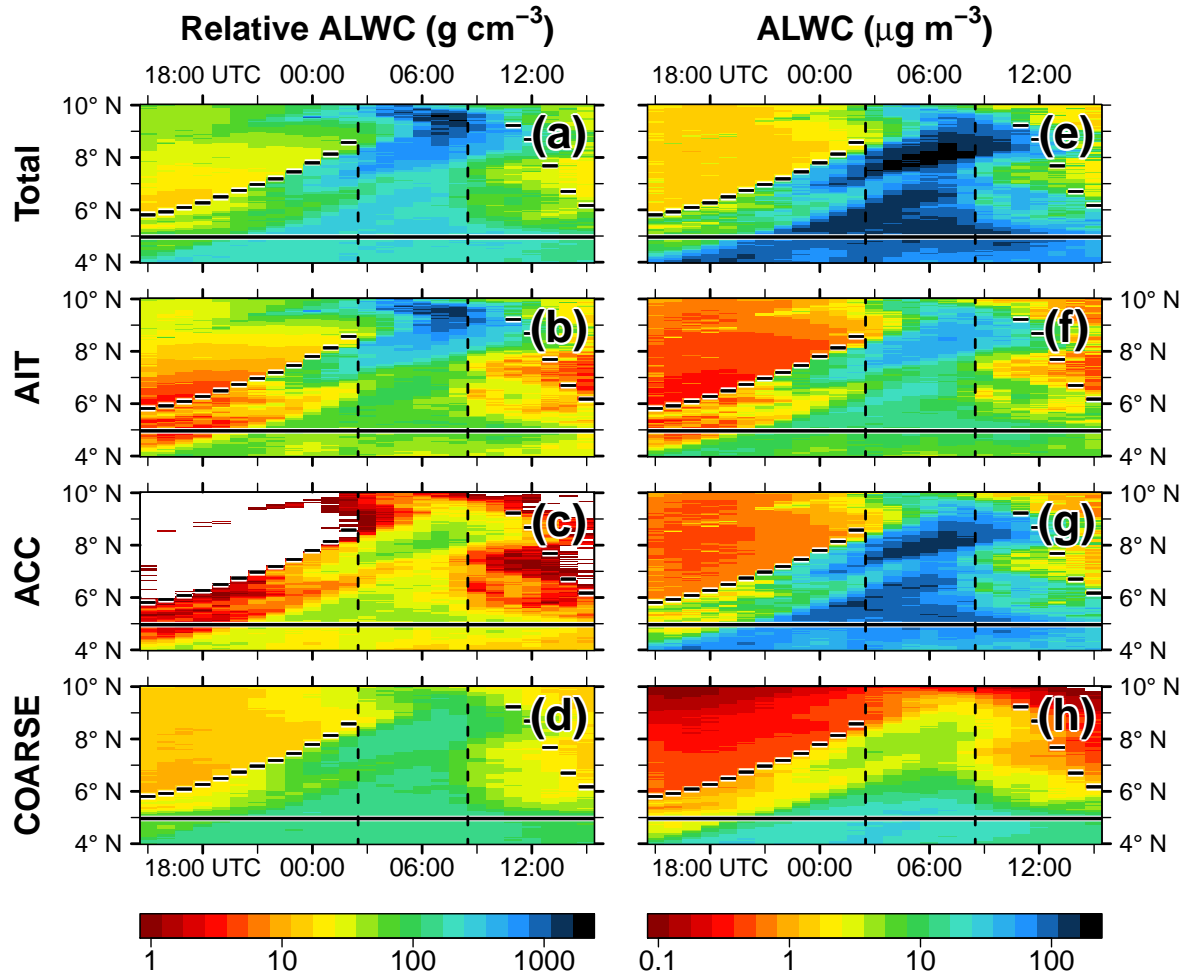


Figure 4. Same as for Fig. 3 but for (left) relative ALWC (g ALWC cm^{-3} dry aerosol) with respect to (a) total relative ALWC, (b) relative ALWC_{AIT}, (c) relative ALWC_{ACC} and (d) relative ALWC_{COARSE} and (right) absolute ALWC ($\mu\text{g ALWC m}^{-3}$ air) with respect to (e) total ALWC, (f) ALWC_{AIT}, (g) ALWC_{ACC} and (h) ALWC_{COARSE}.

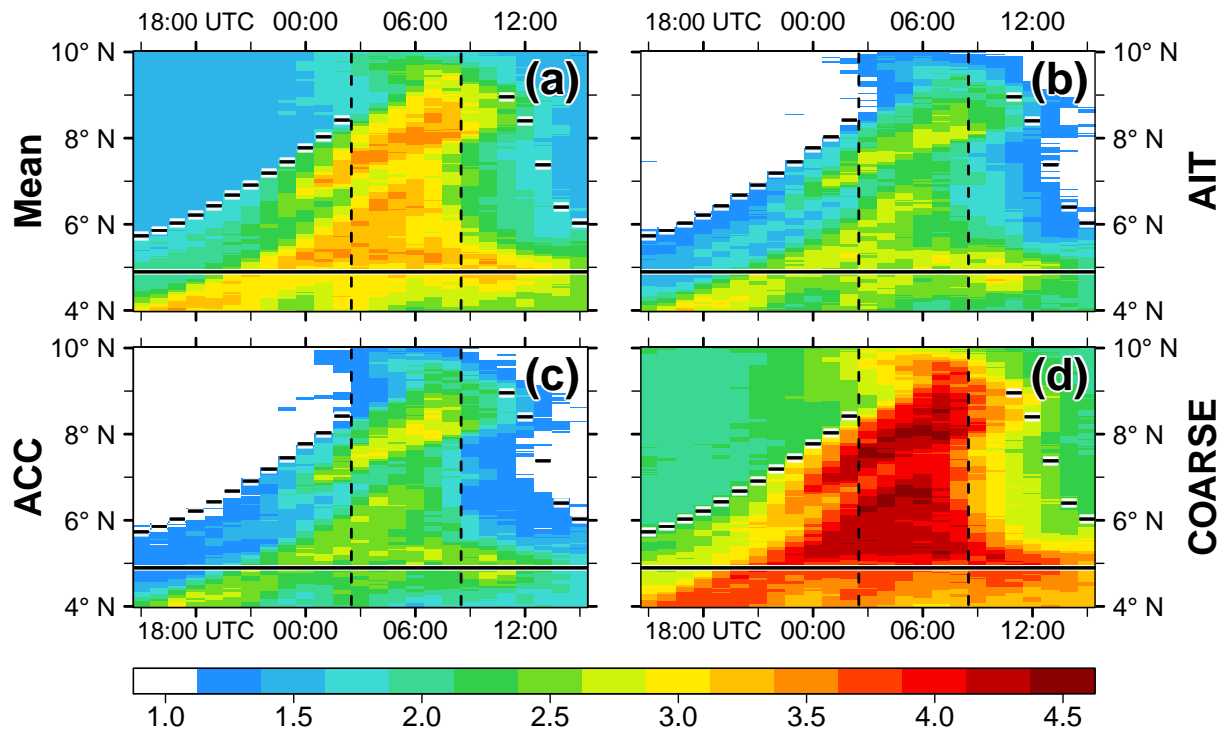


Figure 5. Same as for Fig. 3 but for the GF ($d_{p,wet} d_{p,dp}^{-1}$) with respect to (a) mean GF, (b) GF_{AIT}, (c) GF_{ACC} and (d) GF_{COARSE}.

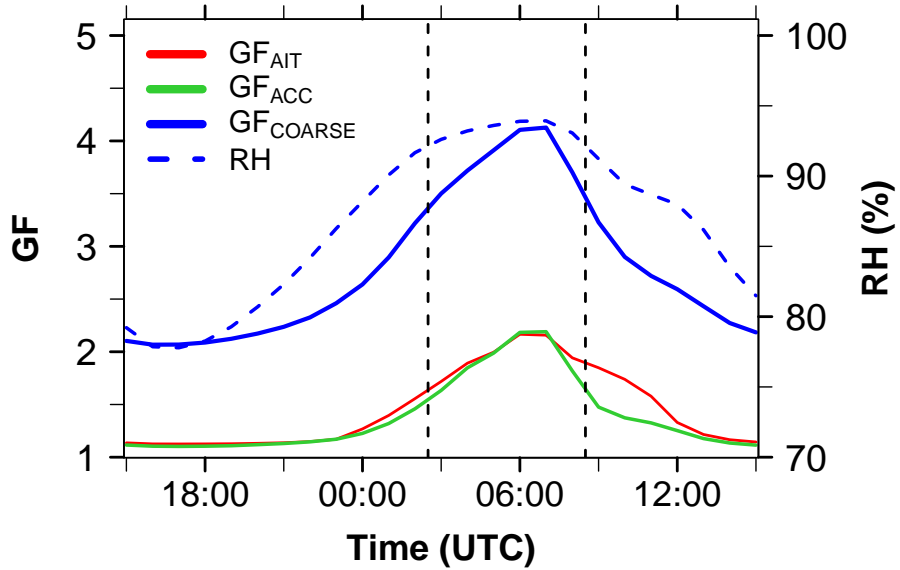


Figure 6. Diurnal cycle of the median GF (%) of GF_{AIT} (red), GF_{ACC} (green), GF_{COARSE} (blue) and RH (%) (blue dashed) in the lowest 1500 m AGL over Ivory Coast (7.5° W– 3° W, 4 – 10° N) from 2 July 15 UTC to 3 July 15 UTC. The vertical dashed lines denote the three phases introduced in Figure 3.

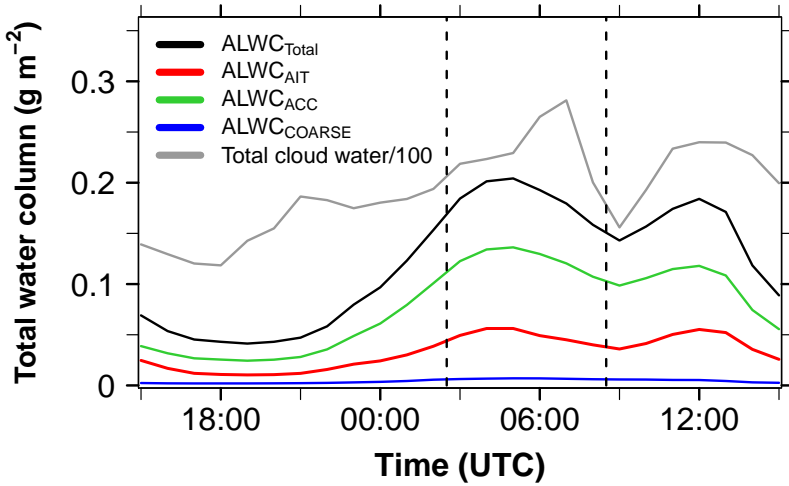


Figure 7. Diurnal cycle of total cloud water column (g m^{-2}) as median over Ivory Coast (7.5° W– 3° W, 4 – 10° N) from 2 July 15 UTC to 3 July 15 UTC with respect to $ALWC_{Total}$ (black), $ALWC_{AIT}$ (red), $ALWC_{ACC}$ (green) and $ALWC_{COARSE}$ (blue) as well as the median total cloud water (grey, divided by 100). Values below 10^{-3} g m^{-2} are not considered. The vertical dashed lines denote the three phases introduced in Figure 3.

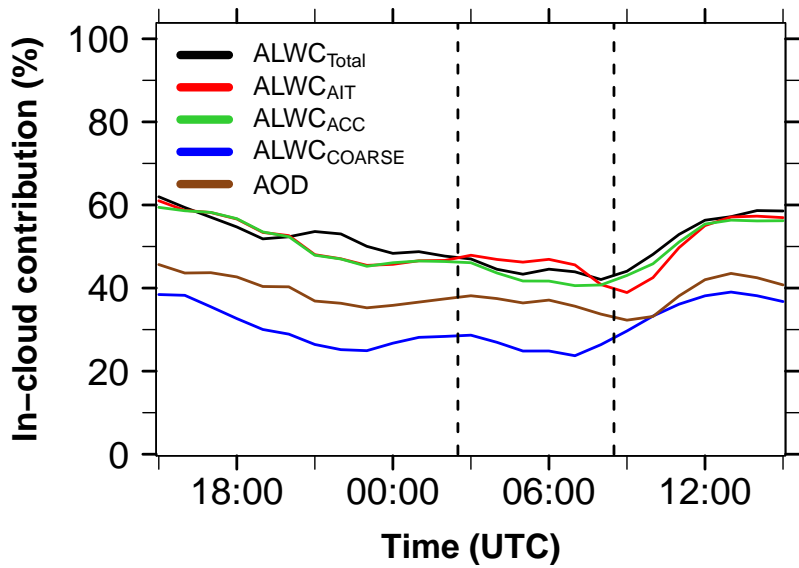


Figure 8. Diurnal cycle of the median contribution from in-cloud areas (%) with respect to $\text{ALWC}_{\text{Total}}$ (black), ALWC_{AIT} (red), ALWC_{ACC} (green), $\text{ALWC}_{\text{COARSE}}$ (blue) and the contribution of in-cloud AOD to the total AOD (brown) in the total vertical column over Ivory Coast (7.5° W– 3° W, 4 – 10° N) from 2 July 15 UTC to 3 July 15 UTC. The vertical dashed lines denote the three phases introduced in Figure 3.

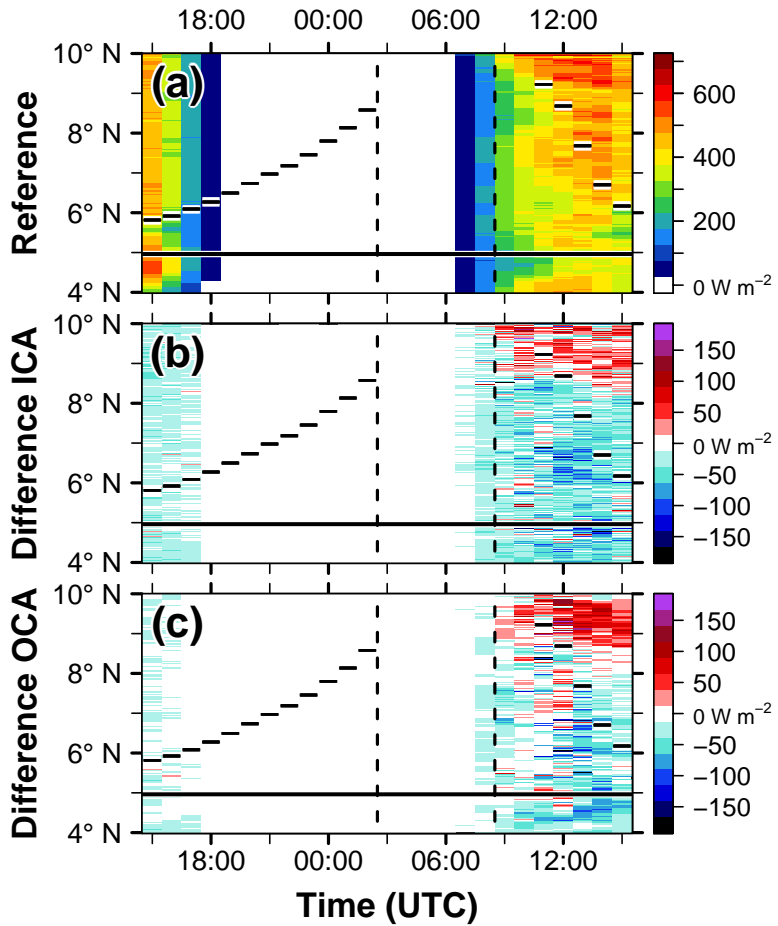


Figure 9. Hovmöller diagram of SSR (W m^{-2}) for (a) *Reference*, (b) *Reference* minus *No-ALWC* for ICA and (c) *Reference* minus *No-ALWC* for OCA as zonal mean over Ivory Coast (7.5° W– 3° W, 4 – 10° N) between 2 July 15 UTC and 3 July 15 UTC. The horizontal bars denote the zonal mean location of the 302 K isentrope at 250 m AGL of *Reference*, the horizontal solid line the zonal mean coast line and the vertical dashed lines the three phases introduced in Figure 3.

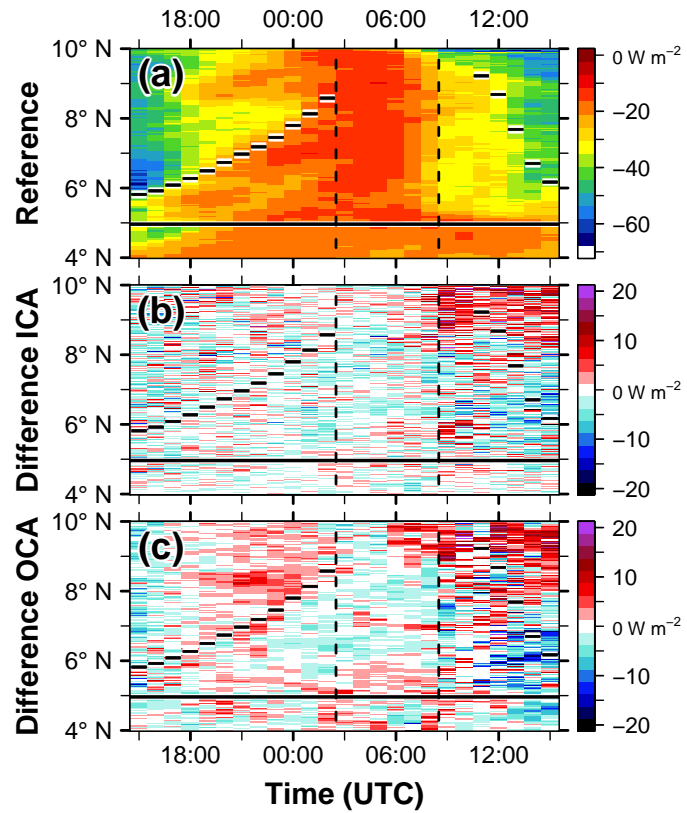


Figure 10. Same as for Fig. 9 but for SLR: (a) *Reference*, (b) *Reference* minus *No-ALWC* for ICA (c) *Reference* minus *No-ALWC* for OCA. Positive (negative) values in (b) and (c) denote more outgoing longwave radiation in *Reference* (*No-ALWC*).

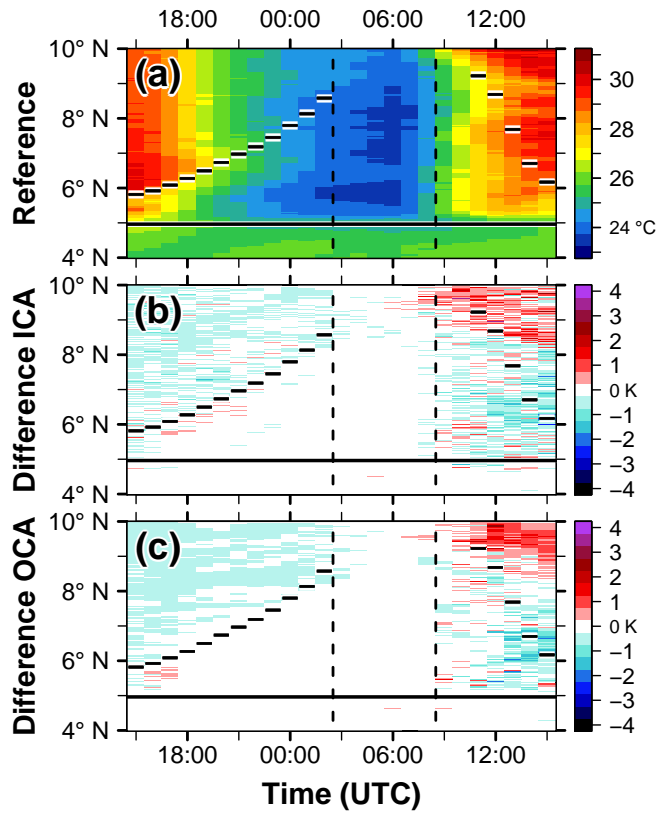


Figure 11. Same as for Fig. 9 but for 2-m temperature ($^{\circ}\text{C}$) and 2-m temperature difference (K): (a) *Reference*, (b) *Reference* minus *No-ALWC* for ICA (c) *Reference* minus *No-ALWC* for OCA.

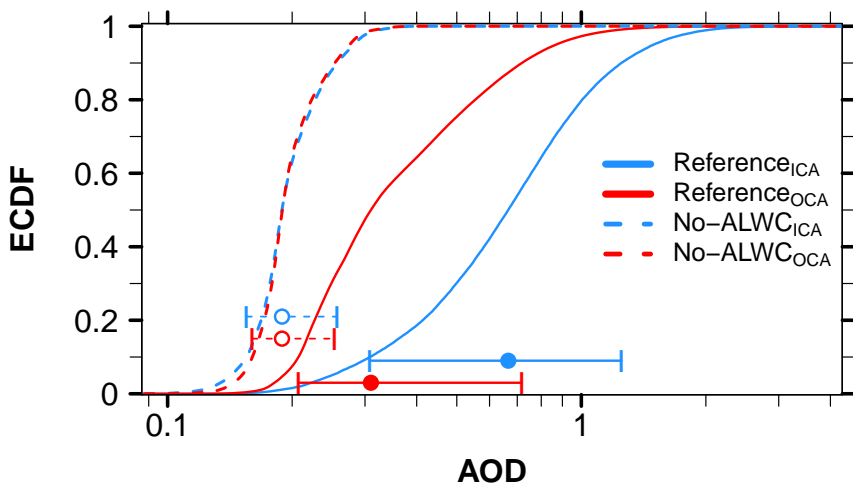


Figure 12. ECDF of the total AOD of ICA (blue) and OCA (red) for *Reference* (solid lines) and *No-ALWC* (dashed lines) over Ivory Coast (7.5° W– 3° W, 4 – 10 ° N) including the time period from 2 July 15 UTC to 3 July 15 UTC. The dots (circles) highlight the median with respect to *Reference* (*No-ALWC*) and the whisker the 10th and 90th percentiles.

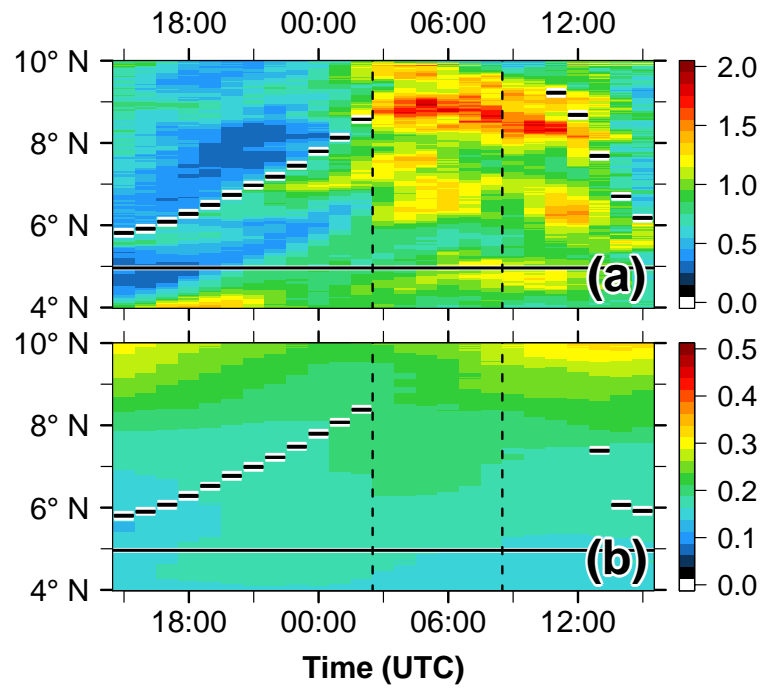


Figure 13. Hovmöller diagram of AOD for (a) *Reference* and (b) *No-ALWC* as zonal mean over Ivory Coast (7.5° W– 3° W, 4 – 10° N) between 2 July 15 UTC and 3 July 15 UTC. The horizontal bars denote the zonal mean location of the 302 K isentrope at 250 m AGL, the horizontal solid line the zonal mean coast line and the vertical dashed lines the three phases introduced in Figure 3. Note the different color scales in (a) and (b).

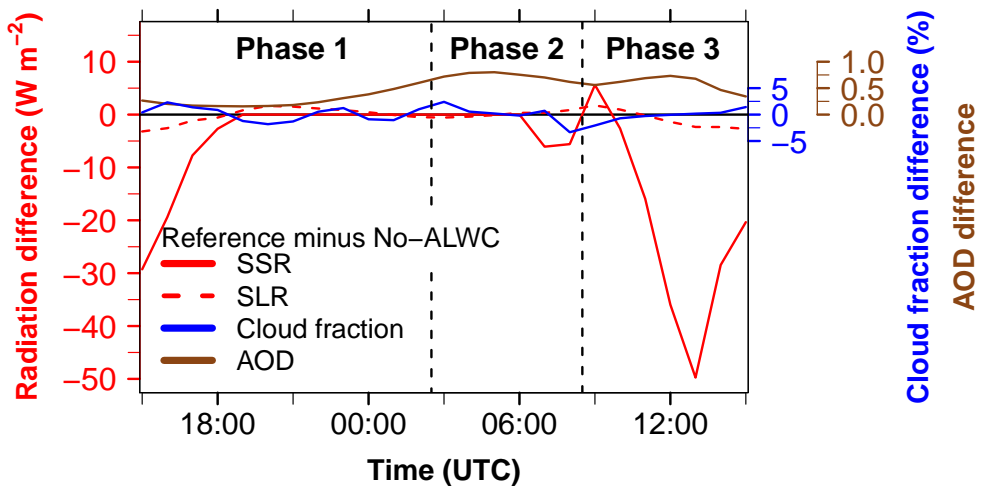


Figure 14. Diurnal cycle of the difference between *Reference* and *No-ALWC* with respect to SSR (red solid, W m^{-2}), SLR (red dashed, W m^{-2}), domain-wide cloud fraction (blue, %) and AOD (brown) as median over Ivory Coast (7.5°W – 3°W , 4 – 10°N) between 2 July 15 UTC and 3 July 15 UTC. The vertical dashed lines indicate the three phases introduced in Figure 3. Note the color coded of the different ordinates.

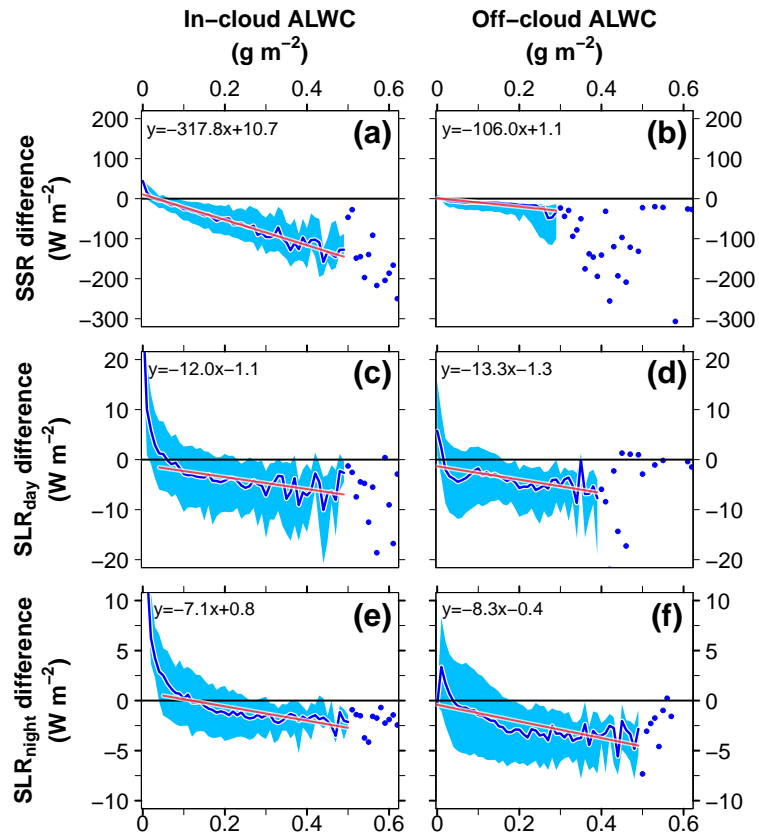


Figure 15. Relationship between the total column ALWC (g m^{-2}) and the radiation difference between *Reference* and *No-ALWC* (W m^{-2}) capturing Ivory Coast (7.5°W – 3°W , 4 – 8°N) and the time period 2 July 15 UTC to 3 July 15 UTC. The data is clustered in areas that are simultaneously cloudy (left, ICA) or cloud free (right, OCA) in both realizations. The top panels show the SSR difference (2 July 15–18 UTC and 3 July 7–15 UTC), the middle panels the SLR daytime difference (same time period as SSR) and the bottom panels the SLR nighttime difference (2 July 19 UTC to 3 July 6 UTC). The ALWC values are clustered in bins with an increment of 0.01 g m^{-2} . For every bin the spatial median of the radiation difference is calculated (blue line). The envelope, spanned by the 25th and 75th percentile of the radiation difference, is shown as blue shading. For greater ALWC values the spread significantly increases. For this area (empirically selected) the median radiation difference is shown as blue dots instead of a blue line. A linear fit is calculated for the first part of the curves (red line). The fitted equations are shown in the top-left corner of the panels.

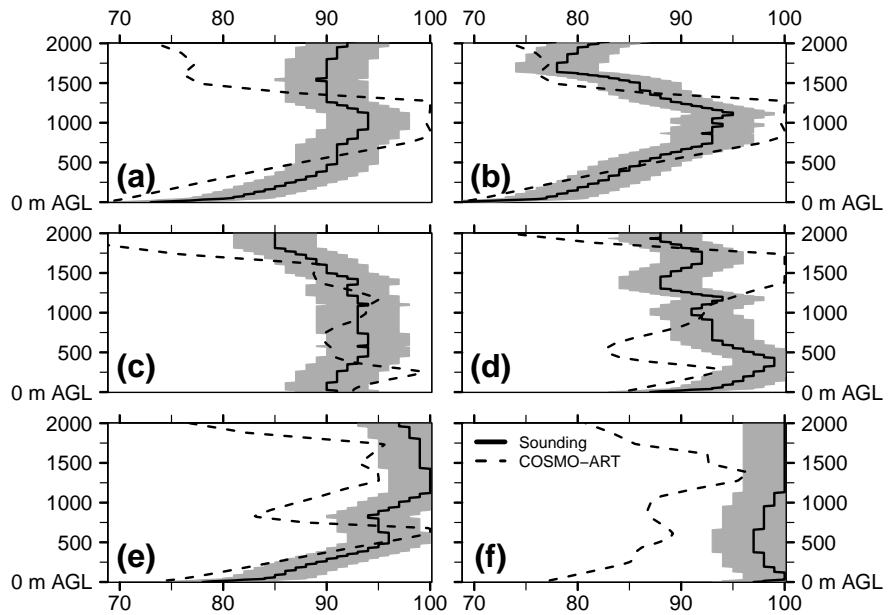


Figure 16. RH vertical profiles at Lamto (Ivory Coast) with respect to radiosoundings (black solid) and COSMO-ART (black dashed) on (a) 6 July 12 UTC, (b) 6 July 18 UTC, (c) 7 July 6 UTC, (d) 7 July 9 UTC, (e) 7 July 12 UTC and (f) 7 July 18 UTC. For the GRAW radiosondes an uncertainty of $\pm 4\%$ are assumed (grey shading). The Lamto soundings are related to problems with reaching the 100 % RH (Andreas Fink, personal communication, 2018).

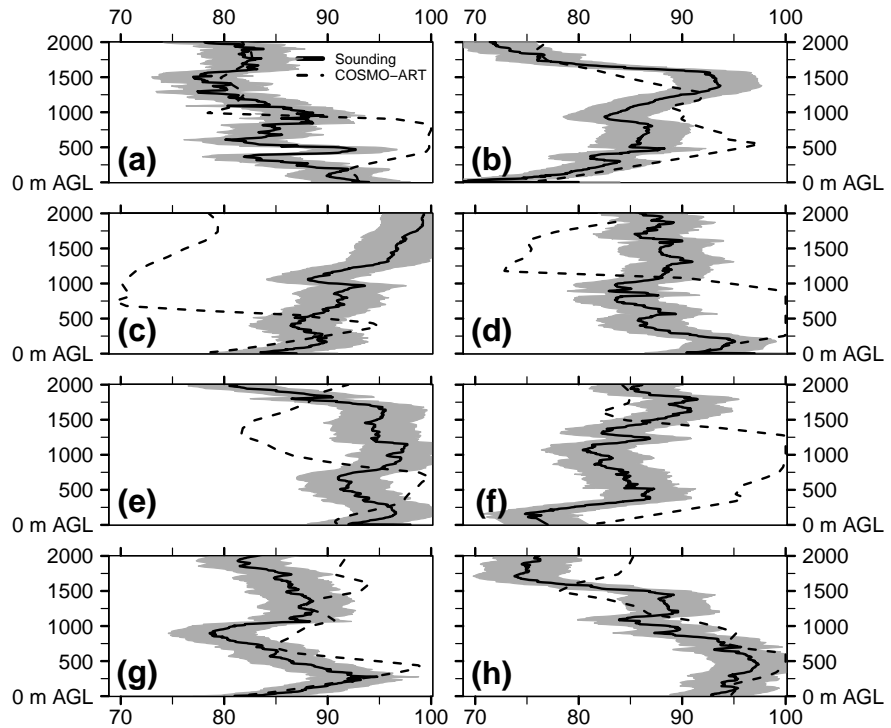


Figure 17. RH vertical profiles at Abidjan (Ivory Coast) with respect to radiosoundings (black solid) and COSMO-ART (black dashed) on (a) 2 July 4 UTC, (b) 2 July 10 UTC, (c) 2 July 16 UTC, (d) 2 July 23 UTC, (e) 3 July 4 UTC and (f) 3 July 10 UTC, (g) 3 July 16 UTC and (h) 3 July 23 UTC. For the Meteomodem radiosondes an uncertainty of $\pm 4\%$ are assumed (grey shading).

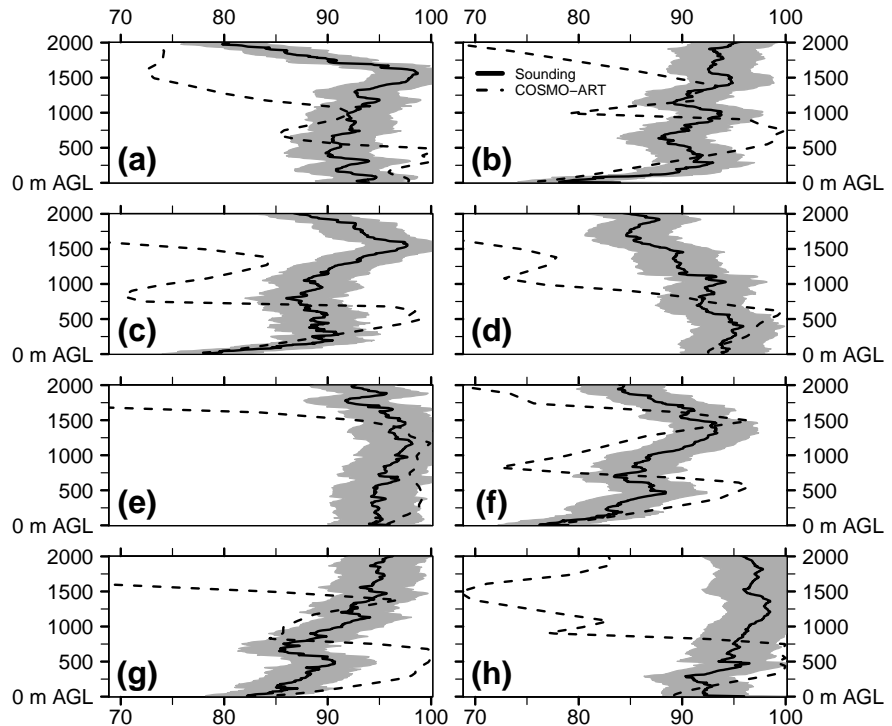


Figure 18. Same as for Figure 17 but for (a) 6 July 4 UTC, (b) 6 July 10 UTC, (c) 6 July 16 UTC, (d) 6 July 23 UTC, (e) 7 July 4 UTC, (f) 7 July 10 UTC, (g) 7 July 16 UTC and (h) 7 July 23 UTC.

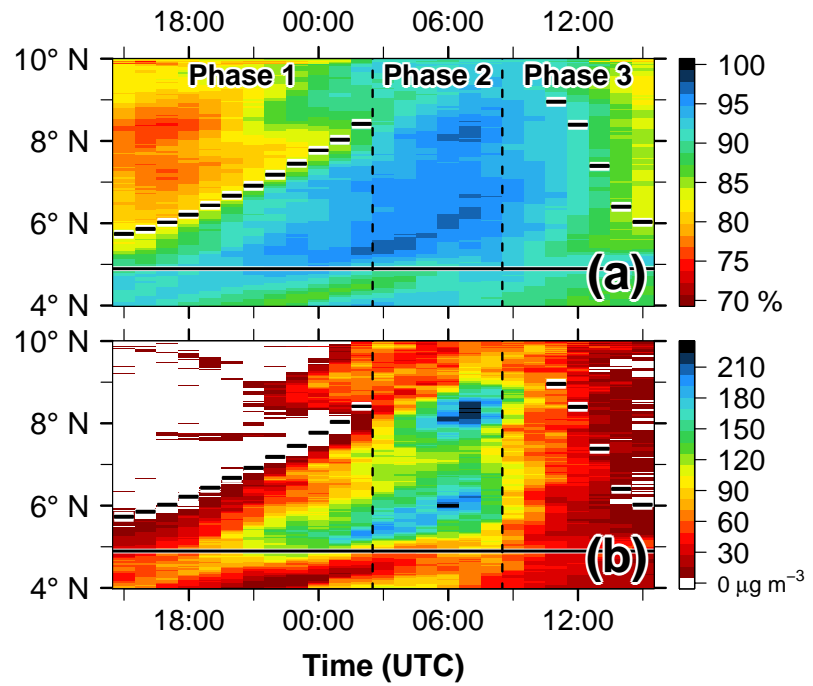


Figure 19. Hovmöller diagram of the median (a) RH (%) and (b) total ALWC ($\mu\text{g m}^{-3}$) in the lowest 1500 m AGL as zonal mean over Ivory Coast (7.5°W – 3°W , 4 – 10°N) between 6 July 15 UTC and 7 July 15 UTC. The horizontal bars denote the zonal mean location of the 302 K isentrope at 250 m AGL, the horizontal solid line indicates the zonal mean coast line and the vertical dashed lines separate the three phases: *AI progression phase* (Phase 1), *Moist morning phase* (Phase 2) and *Daytime drying phase* (Phase 3).

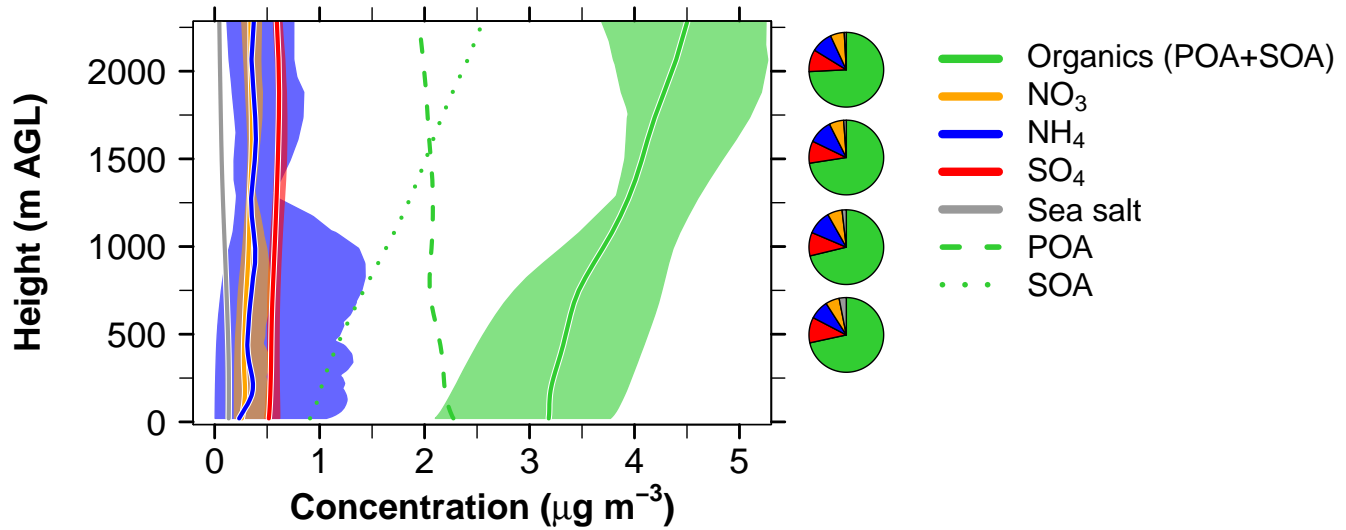


Figure 20. Vertical profiles (m AGL) of aerosol concentrations ($\mu\text{g m}^{-3}$) for the median over Ivory Coast (7.5°W – 3°W , 4 – 10°N) with respect to the time period 2 July 15 UTC and 3 July 15 UTC. The colors refer to organics (POA+SOA; green solid line), NO_3 (orange solid line), NH_4 (blue solid line), SO_4 (red solid line) and sea salt (grey solid line). Additionally, POA and SOA are shown as dashed and dotted green lines, respectively. The shadings denote minima and maxima in the diurnal cycle mean profile and the pie charts on right hand side highlight the mean contribution of the single species to the total aerosol composition at 500, 1000, 1500 and 2000 m AGL.

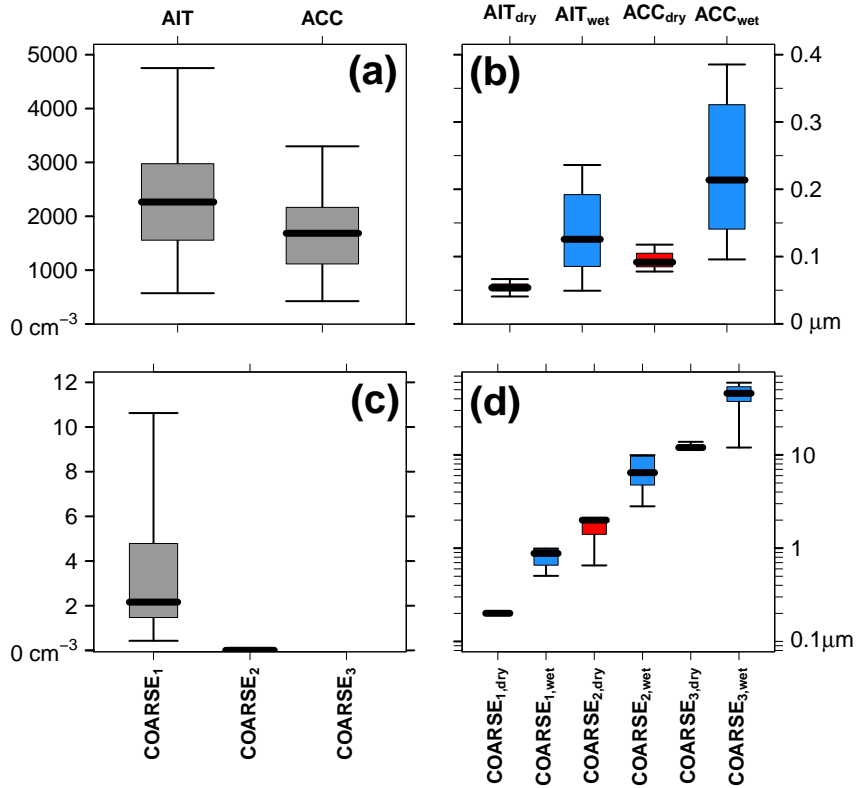


Figure 21. Boxplots of (a) aerosol number density (cm^{-3}) and (b) dry (red) and wet (blue) aerosol diameters (μm) for AIT and ACC and boxplots of (c) aerosol number density (cm^{-3}) and (d) dry (red) and wet (blue) aerosol diameters (μm) for COARSE, splitted in the three COSMO-ART sea salt modes as median in the lowest 1500 m AGL over Ivory Coast (7.5°W – 3°W , 4 – 10°N) on 3 July, 6 UTC. The whiskers span the data from the 2.5th to the 97.5th percentile (95 % of the data). Data outside of this range is not shown. Note the different unit in (c) (conversion factor is 10^6) and the logarithmic scale in (d). The absolute value of the number density of COARSE₃ is below 1.3 cm^{-3} and is therefore not shown in (c).

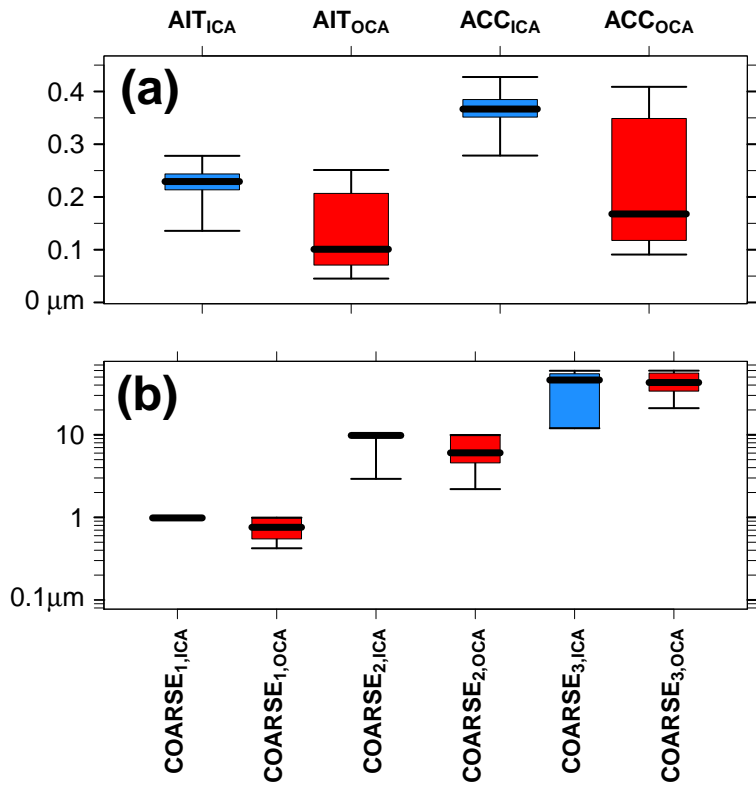


Figure 22. Boxplots of aerosol wet diameters (μm) for (a) AIT and ACC and (b) COARSE, splitted in the three COSMO-ART sea salt modes as median in the lowest 1500 m AGL over Ivory Coast (7.5° W – 3° W , 4 – 10° N) on 3 July, 6 UTC by separating in ICA (areas with non-zero cloud water, blue) and OCA (areas with zero cloud water, red). The whiskers span the data from the 2.5th to the 97.5th percentile (95 % of the data). Data outside of this range is not shown.

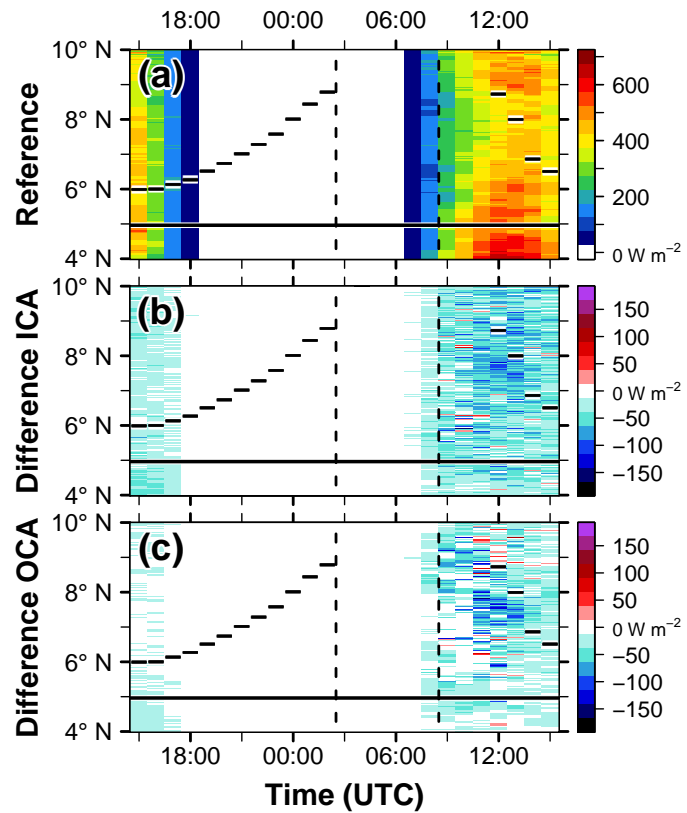


Figure 23. Hovmöller diagram of SSR (W m^{-2}) for (a) *Reference*, (b) *Reference* minus *No-ALWC* for ICA (c) *Reference* minus *No-ALWC* for OCA as zonal mean over Ivory Coast (7.5° W– 3° W, 4 – 10° N) between 6 July 15 UTC and 7 July 15 UTC. The horizontal bars denote the zonal mean location of the 302 K isentrope at 250 m AGL of *Reference*, the horizontal solid line the zonal mean coast line and the vertical dashed lines the three phases introduced in Figure 3.

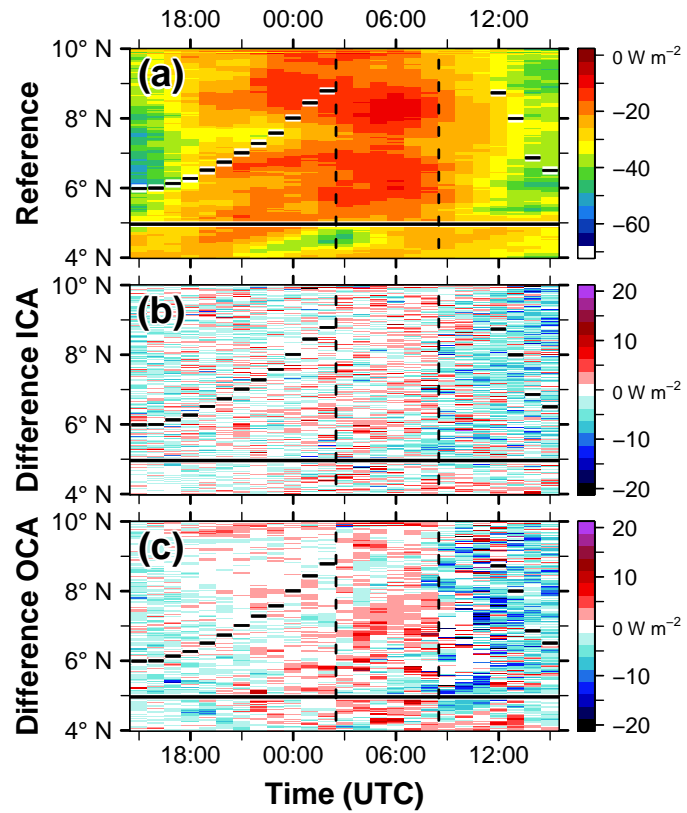


Figure 24. Same as for Fig. 23 but for the SLR. Positive (negative) values in (b) and (c) denote more outgoing longwave radiation in the Reference (No-ALWC) case.

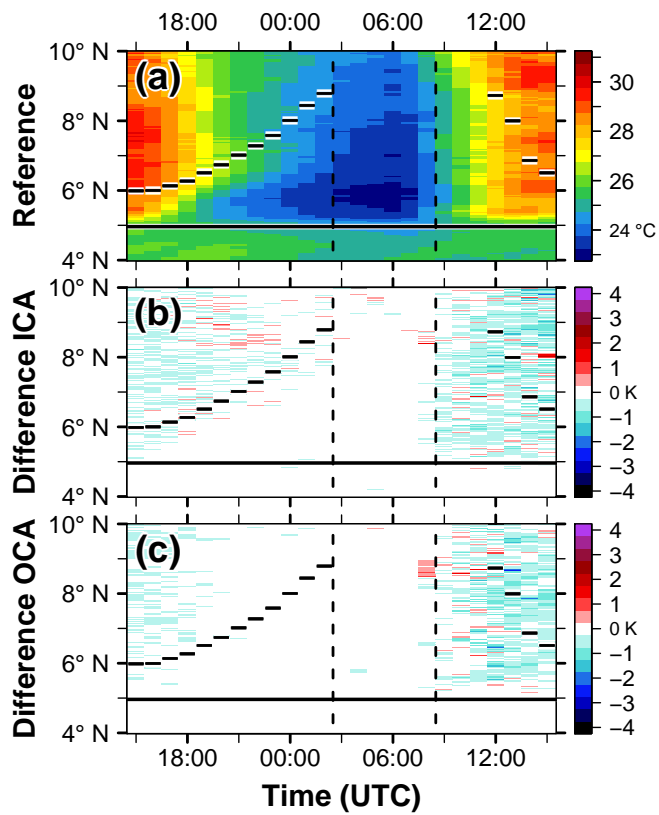


Figure 25. Same as for Fig. 23 but for 2-m temperature ($^{\circ}\text{C}$) and 2-m temperature difference (K).

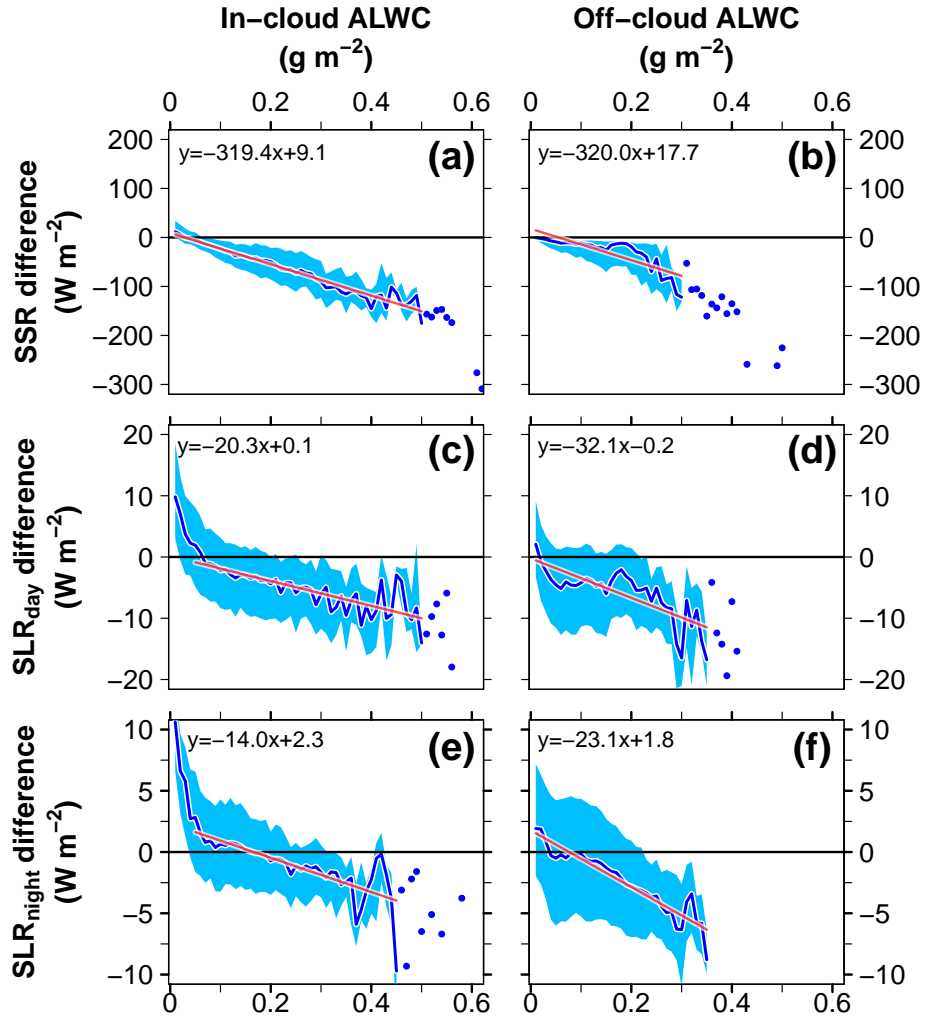


Figure 26. Relationship between the total column ALWC (g m^{-2}) and the radiation difference between *Reference* and *No-ALWC* (W m^{-2}) over Ivory Coast (7.5°W – 3°W , 4 – 8°N) during the time period 2 July 15 UTC to 3 July 15 UTC. The data is clustered in areas that are simultaneously cloudy (left, ICA) or cloud free (right, OCA) in both realizations. The top panels show the SSR difference (6 July 15–18 UTC and 7 July 7–15 UTC), the middle panels the SLR daytime difference (same time period as SSR) and the bottom panels the SLR nighttime difference (2 July 19 UTC to 3 July 6 UTC). The ALWC values are clustered in bins with an increment of 0.01 g m^{-2} . For every bin the spatial median of the radiation difference is calculated (blue line). The envelope, spanned by the 25th and 75th percentile of the radiation difference, is shown as blue shading. For greater ALWC values the spread significantly increases. For this area (empirically selected) the median radiation difference is shown as blue dots instead of a blue line. A linear fit is calculated for the first part of the curves (red line). The fitted equations are shown in the top-left corner of the panels.